On Relating Physical Damage to Mechanical Response in Advanced Ceramics

by

Brendan M. L. Koch

A thesis submitted in partial fulfillment of the requirements for the degree of

Doctor of Philosophy

Department of Mechanical Engineering
University of Alberta

Abstract

This thesis is concerned with the experimental mechanics of brittle failure in advanced ceramics. It seeks to bridge global damage accumulation to local failure phenomena. Alumina serves as the primary model material. Other advanced ceramics (silicon carbide and boron carbide) and cermets are included for the purposes of comparison against alumina. Microstructural features such as grain boundaries, grain sizes, inclusionary bodies, and internal pores and cracks are obtained for alumina and compared to mechanical responses. For all brittle materials, experiments used to probe the mechanical response and failure behaviors include quasi-static compressive testing, Kolsky pressure bar dynamic compressive testing, and impact testing. Failure behaviors are captured using ultra-high-speed imaging, which also allows for the determination of 2D strain fields via digital-image-correlation. With 2D strains, contributions derived from this research are made to better model damage evolution in all materials during loading and catastrophic failure. Damage evolution is expanded to include the changes to axial-lateral response as well as stress-strain response. Experiments demonstrate non-linear and non-monotonic changes in behavior. Further refinement of mechanical response tracking demonstrates the importance of shear modulus to compressive failure. Internal local phenomena like crack volume changes can be inferred from global phenomena, such as simultaneous changes in apparent Young's modulus and Poisson's ratio. This thesis constitutes a major contribution to the field of mechanics of brittle materials, in general, and advanced ceramics, in particular. The understanding of physical failure processes is greatly improved, along with which characteristics are of significance to dynamic fracture and failure.

Preface

Chapter 2 of this thesis, with minor modifications, has been published in *Materials Science and Engineering: A*, as **Brendan M. L. Koch**, Phillip Jannotti, Debjoy Mallick, Brian Schuster, Tomoko Sano, James D. Hogan, "Influence of microstructure on the impact failure of alumina" in Press 2020.

Chapter 3 of this thesis, with minor modifications, has been published in *Engineering Fracture Mechanics* as **Brendan M. L. Koch**, Calvin Lo, Haoyang Li, Tomoko Sano, James D. Hogan, "Two-Dimensional Dynamic Damage Accumulation in Engineered Brittle Materials" in Press 2021.

Chapter 4 of this thesis, with minor modifications, has been published in the *Journal of the European Ceramics Society* as **Brendan M. L. Koch**, Calvin Lo, Haoyang Li, Tomoko Sano, Jonathan Ligda, James D. Hogan as "Dynamic Mechanical Response of Damaged Alumina AD995" in Press 2020.

Chapter 5 of this thesis, with minor modifications, has been submitted to *Acta Materialia* as **Brendan M. L. Koch**, Calvin Lo, Jonathan Ligda, James D. Hogan as "Damage Accumulation Mechanisms During Dynamic Compressive Failure of Boron Carbide"

Acknowledgements

Chapter 2 was sponsored by the U.S. Army Research Laboratory and was accomplished under Cooperative Agreement Number W91NF-16-2-0079. The views and conclusions contained in this document are those of the authors and should not be interpreted as representing the official policies, either expressed or implied, of the Army Research Laboratory or the U.S. Government. The U.S. Government is authorized to reproduce and distribute reprints for Government purposes notwithstanding any copyright notation herein.

Chapter 3 was sponsored by the U.S. Army Research Laboratory and was accomplished under Cooperative Agreement Number W91NF-16-2-0079 and W911NF-17-2-0213. The views and conclusions contained in this document are those of the authors and should not be interpreted as representing the official policies, either expressed or implied, of the Army Research Laboratory or the U.S. Government. The U.S. Government is authorized to reproduce and distribute reprints for Government purposes notwithstanding any copyright notation herein.

Chapter 4 was sponsored by the U.S. Army Research Laboratory and was accomplished under Cooperative Agreement Number W91NF-16-2-0079 and W911NF-17-2-0213. The views and conclusions contained in this document are those of the authors and should not be interpreted as representing the official policies, either expressed or implied, of the Army Research Laboratory or the U.S. Government. The U.S. Government is authorized to reproduce and distribute reprints for Government purposes notwithstanding any copyright notation herein.

Chapter 5 was sponsored by the U.S. Army Research Laboratory and was accomplished under Cooperative Agreement Number W91NF-16-2-0079 and W911NF-17-2-0213. The views and conclusions contained in this document are those of the authors and should not be interpreted as representing the official policies, either expressed or implied, of the Army Research Laboratory or the U.S. Government. The U.S. Government is authorized to reproduce and distribute reprints for Government purposes notwithstanding any copyright notation herein.

Table of Contents

Table of Figures

Chapter 1 - Introduction

1.1. Motivation

High strain-rate loading of brittle materials is an area of significant research in mining[1], planetary science[2], and armor applications[3]. In contrast with planetary science and mining, armor research focuses on studying man-made ceramics rather than naturally occurring rocks. For armor applications, the interplay of factors such as material strength, stiffness, toughness, speed of sound, and the failure mode(s) that govern projectile defeat is particularly complex. The mechanics of brittle failure gives certain brittle materials a particular ability to resist kinetic penetrator impacts[4–11]. Rather than failing due to localized shear the way that ductile metals do[12–15], brittle ceramics fracture and fragment in a conoidal volume that better distributes the forces and impact energy. In further contrast to metals, ceramics comminute into a fine powder during impact[16,17], which can be ejected away from the projectile as an alternative to remaining in the front of the projectile. This process further dissipates energy and contributes to eroding and blunting the projectile, reducing its penetrative capacity, and potentially, leading to projectile defeat[18,19]. Ceramics also demonstrate features such as strain-rate dependent hardening up to their Hugoniot elastic limit (HEL)[20], and this means that properties such as hardness and failure strength increase in importance up to the hypervelocity impact regime[2,21,22]. The materials of highest interest for these properties are termed advanced ceramics due to the high degree of technical sophistication required to manufacture them at high purities. Examples of advanced ceramics that receive significant attention in the scientific literature and in engineering applications are alumina, boron carbide, and silicon carbide. The complex properties that make advanced ceramics attractive for use resisting ballistic impacts also make them difficult to model under dynamic conditions due to the fact that their properties change with strain-rate. This means that properties obtained using quasi-static testing are not necessarily applicable under dynamic conditions. Furthermore, the actual failure process occurs on a scale of microseconds. Under impact conditions a material retaining its resistance to deformation for a microsecond longer can be the difference between defeat of a projectile and penetration of the ceramic[23–25]. In order to improve the performance of these materials, better models that incorporate how advanced ceramics behave under dynamic conditions and how they go from intact to fragmented are required to facilitate simulation during design. In order to improve models such as the Johnson-Holmquist constitutive models[26], a better understanding of the properties of advanced ceramics and how they evolve with strain and strain-rate up to total failure is required. This thesis seeks to address this problem through the use of new experimental and analysis techniques.

Primary material properties of interest within the literature are fracture toughness, failure strength, elastic modulus, and crack speed[27–31]. Experiments from the literature also show that these properties can change with increasing strain rate. Material properties arise from a combination of the chemical constituents and multiscale structural features. For example, defects, such as secondary inclusions and pores, serve as favorable failure nucleation sites, but in quasi-static conditions may not influence properties as significantly as under dynamic conditions[32–35]. The orientation of defects also influences the failure of a ceramic, as modelled by Hu *et al.*[36] and observed experimentally by Hogan *et al.*[37]. In some cases, two materials can have similar quasi-static properties but divergent properties as strain-rate increases, such as in impact[32] or compression bar experiments[38]. A material deemed to have superior qualities under quasi-static testing may also prove inferior under dynamic conditions. An illustrative example of this phenomenon is found in the work of Arab *et al.*[33]. For their work, they were seeking to improve the fracture toughness of zirconia toughened aluminum oxide (ZTA) through the addition of strontium carbonate. Under quasi-static conditions this addition increased the fracture toughness by forming a secondary phase at the grain boundaries. This secondary phase also increased the porosity of the material. When performing dynamic compression testing via split-Hopkinson pressure bar, all of the specimens with strontium carbonate had inferior fracture toughness and failure strength to pure ZTA. The authors attributed the poor dynamic performance to the added porosity, which was what had improved quasi-static values. These tests demonstrate the complexities between material design, fabrication, microstructure, and strain-rate dependent mechanical properties. The work of Arab *et al.*[33] serves as an extreme example of a discrepancy between experimentally observed behavior and the predictions made based upon quasi-static behavior. Other discrepancies between theoretically predicted and experimental behavior of brittle materials under dynamic loading forms the core of this thesis.

Ideally, one would be able to produce a model or simulation capable of taking information from non-destructive characterization experiments and use them to predict accurately the behavior of a given ceramic. Due to the strain-rate dependencies for ceramics this is not a computationally simple process. As an example of the complexity of rate-dependencies, in the edge-on-impact (EOI) experiments of Strassburger *et al.*[39–43] to determine how damage propagates in ceramics using high-speed video, there are two general damage propagation regimes that depend upon impactor velocity. The first regime has crack speed increase with increasing impactor velocity, while the second regime features crack speed not increasing as significantly with increasing impactor velocity, with this plateauing velocity being associated with some fraction of the speed of sound within the ceramic[39]. With two different behavior domains below the HEL, and each with a different response to increasing impact energy, any model that seeks to capture this behavior will need to account for how materials respond to kinetic impacts differently depending on what strain-rate regime they are in. This serves as a single example of the difficulties in capturing strain-rate dependent behavior of a material as it transitions from quasi-static to dynamic and then to shock-discontinuity behavior.

From an initial literature review that will be further motivated by the Introduction sub-sections of the chapters throughout this thesis, a picture emerges of multiple related but distinct phenomena interacting to govern the dynamic behavior and failure of advanced ceramics. Under impact loading, the material directly in contact with the projectile is subjected to an initial compressive loading[16,37,39,44] and thus how these materials perform under easily controlled compressive loading is the foundation of predicting how it will perform under the more complex impact loading. Brittle fracture theory holds that globally compressive loading is transformed into local tension or shear loading[45–48], while constitutive models track global changes in material behavior[37,49–54] where the propagation of failure is an intrinsically local phenomenon. Recent advancements in experimental tools and techniques have allowed improvements in how we study the failure of brittle materials, providing new data on failure behaviors. This thesis explores failure phenomena with new experimental tools capable of capturing previously unobserved behavior and the implications that stem from this new data. For example, a key discussion point is the distinction between “physical damage” and “apparent mechanical damage”. Physical damage refers to the irreversible changes that occur in a sample such as crack formation and growth. Apparent mechanical damage is caused by physical damage, and it is how mechanical responses such as Young's modulus, Poisson's ratio, or shear modulus change. The ability to relate the two forms of damage is key to modelling and simulation, but the work done in this thesis shows that the relationship is more complex than previously assumed.

1.2. Objectives

The thesis objective is to develop a better understanding through experimental mechanics of how an intact advanced ceramic becomes damaged and then fails from a mechanics of materials perspective. From this understanding, the design and performance of advanced ceramics under dynamic loading can be better predicted. This is achieved by utilizing new diagnostic technologies such as ultra-high-speed cameras, digital-image-correlation, and photon-Doppler velocimetry to improve experimental data gathering methods. The data gathered in experiments contains information such as lateral strain and stress-strain from the unloading phase of failure not anticipated by prior theories on damage accumulation[26,36,55], requiring evaluation of results with more fundamental theories such as wing-crack growth[56] and developing methods of expressing the data in a manner consistent with past results. This has resulted in the expansion of damage accumulation formulations in this thesis to now include changes to the apparent Poisson's ratio and shear modulus, rather than just the Young's modulus as previously used[26,36,49,50,54,55]. The outcomes of this thesis will be important to: 1. the design of new materials that have tailored mechanical properties and microstructures to better resist dynamic failure, 2. for the development and validation of computational models describing fracture in advanced ceramics, and 3. for better understanding the overall ballistic performance and high rate response of advanced ceramics used in personal protection equipment.

Through this thesis, I have accomplished the following research goals:

- Used novel experimental diagnostics such as high-speed imaging and digital-image-correlation (DIC), high-speed strain gauges, and photon-Doppler velocimetry to determine axial and lateral strains, and global stresses during impact to determine elastic and inelastic behaviors and how they evolve with a specified input compressive stress. Particular emphasis is given to the process of bulking (also known as dilatancy), which is the process by which crack expansion increases the apparent volume of a sample[56].

- Used high-speed imaging in impact and Split-Hopkinson pressure bar experiments to observe localized crack formation and propagation towards better understanding how failure events are sequenced. There exists limited measurements of this kind, and so I have provided new insights into the speed and mechanisms for crack growth.
- Characterize the microstructures and chemistry of advanced ceramics to understand how initial chemical and physical structures influence local and global failure events. In particular, two different grades of aluminum oxide were used as model materials so that the differences in microstructure can serve as the primary difference rather than more extreme chemical differences such as between aluminum oxide and silicon carbide. Aluminum oxide is also a widely used material in military and industrial applications (e.g. abrasives, insulators, protective coatings), and thus its study has wide applicability. These characterization efforts provide insights into the important microstructural length scales and features that govern failure of these materials.
- Compare and contrast behaviors found in aluminum oxide to other advanced ceramics (e.g. silicon carbide and boron carbide), cermets, and geo materials in order to determine which newly observed failure processes are common to brittle materials and which are unique to advanced ceramics or individual ceramic types. This improves the understanding of which performance metrics are most important for resisting failure at high strain-rates, and how chemical and microstructural differences produce different outcomes. Some of these comparisons are made by additional experimental work (e.g. performing the same experiments on boron carbide), while some are made by drawing upon data available in the literature.
- Studied how observable macroscopic changes in stress-strain and axial-lateral responses of advanced ceramics imply microstructural changes during compression. In particular, changes to the apparent Poisson's ratio imply how internal microcracks can open or close, as the changes require either the loss or addition of volume that can only come from the rearrangement of crack geometries.
- Building on work done by past researchers on the failure of brittle materials [36,52,55,56], I have expanded theoretical formulations for how to describe damage in brittle materials by introducing additional terms to stress-strain response equations in order to encompass observed changes to apparent Poisson's ratio or shear modulus in

addition to Young’s modulus. This allows for the incorporation of previously unobserved behavior into theory in order to include these behaviors into future predictions. This constitutes the main fundamental contribution of my thesis, and this work is important because it provides new insights into dynamic failure of materials and renewed motivation for improving brittle failure models describing their behavior.

- Discovered there exists at least two different damage accumulation behaviors that are strain-rate dependent for brittle materials. In the lower strain-rate quasi-static regime, bulking does not contribute to failure behavior, and damage to the apparent Young’s modulus is sufficient to model the material response. As strain-rate increases, bulking becomes significant and the elastic moduli of importance are the apparent Poisson’s ratio and the shear modulus.

1.3. Thesis Structure

This thesis is structured based off of research published as journal articles and is presented in the following order:

- Chapter 1: “Introduction”. Discusses the background and motivation for studying advanced ceramics and outlines the major contributions to the field done by the thesis.
- Chapter 2: “Influence of Microstructure on the Impact Failure of Alumina”. Published in *Materials Science and Engineering A*, as **Brendan M. L. Koch**, Phillip Jannotti, Debjoy Mallick, Brian Schuster, Tomoko Sano, James David Hogan, Volume 770 (2020). A study into the chemical and microstructural features of two grades of aluminum oxide (alumina) and how these grades differ in their response to an impact loading event. Correlations between impact response events and material microstructure show the importance of low porosity and high chemical homogeneity to the ability of alumina to resist penetration by a kinetic impactor. This study demonstrated how variation in microstructure affected the ability of a ceramic to stop a ballistic impactor and also provided initial interest in how shear mechanics were significant to failure phenomena.
- Chapter 3: “Two-Dimensional Dynamic Damage Accumulation in Engineered Brittle Materials”. Published in *Engineering Fracture Mechanics* as **Brendan M. L. Koch**,

Calvin Lo, Haoyang Li, Tomoko Sano, Jonathan Ligda, James David Hogan, Volume 244 (2021). A study on two grades of alumina, a silicon carbide, and a brittle cermet material subjected to dynamic compressive loading via Kolsky bar. The incorporation of digital image correlation technology to data collection allows for the observation of dynamic two-dimensional stress-strain responses, providing experimental data for the quantification of mechanical damage caused by physical damage. This experimental technique allowed for the development of a method for analyzing two-dimensional strains. This technique demonstrated more complex mechanical behaviors and allowed for the observation of previously unseen damage accumulation mechanisms in compressive loading.

- Chapter 4: “Dynamic Mechanical Response of Damaged Alumina AD995”. Published in the *Journal of the European Ceramics Society* as **Brendan M. L. Koch**, Calvin Lo, Haoyang Li, Tomoko Sano, Jonathan Ligda, James David Hogan, Volume 41, Issue 3 (2021). This investigation concerns the study of one grade of alumina subjected to zero to eight thermal shock cycles in order to accumulate internal physical damage. With previously established damage metrics from Chapter 3, this allows for correlation between the degree of physical damage and how mechanical damage manifests in quasi-static and dynamic compressive loading. This study demonstrated that the loss of shear modulus provided a more physical description of the behavior of the materials than the previously assumed loss of Young’s modulus[26,57–59].
- Chapter 5: “Damage Accumulation Mechanisms During Dynamic Compressive Failure of Boron Carbide”. Submitted to *Acta Materialia* as **Brendan M. L. Koch**, Calvin Lo, Jonathan Ligda, James David Hogan. Working with two different grades of boron carbide compressed in a Kolsky bar at strain rates from 10^2 to 10^3 s^{-1}, this study expands on the usage of shear modulus damage as being indicative of failure. One grade undergoes a transition in damage accumulation behavior within the strain rate range tested, while the other does not. This study shows that the best description of damage accumulation in ceramics is not change to Young’s modulus, but simultaneous change to shear modulus and Poisson’s ratio.
- Chapter 6: Conclusion. A summary of the findings of the thesis and important contributions to the field of mechanics of brittle materials.

The flow of ideas motivating each chapter is as follows:

- Chapter 2 serves as the foundation for overall interest in the dynamic properties of ceramics. The microstructure characteristics of AD-85 and AD-995 are studied in detail and their responses to impact conditions are examined. Of direct relevance to armor applications, these experiments showed the importance of wave speed to the failure process of advanced ceramics. The wave speeds of materials are related to their density and elastic properties, motivating the acquisition of more information on the strain-rate dependencies of those properties in subsequent chapters.
- Chapter 3 is motivated by questions raised in Chapter 2, and by access to new equipment. Experiments continued to use AD-85 and AD-995 due to the interest generated in Chapter 2, but also included silicon carbide and a titanium-aluminum-alumina cermet. These new materials were included to serve as brittle materials with different compositions in order to better understand what properties and damage accumulation behaviors are general to brittle materials rather than specific to alumina. Two unanticipated results motivated further work throughout the rest of the thesis. The first was that the apparent mechanical properties such as Young's modulus and Poisson's ratio could change non-monotonically. An explanation for this behavior was that the microstructure was evolving in a complex manner, such as cracks being closed by compression. This possible microstructure evolution motivated the development of the experiments performed in Chapter 4. The second unexpected result was that the materials with the highest failure strength and stiffness, SiC and AD-995, did not fail as expected. These two materials could exhibit increasing Young's modulus during failure. The expected behavior of a decreasing Young's modulus and increasing Poisson's ratio was only reliably seen in the cermet. The unusual behavior of the stronger ceramics (AD-995 and SiC) motivated working with even stronger and stiffer boron carbide in Chapter 5.
- Chapter 4 sought to determine if the non-monotonic changes in mechanical responses observed in Chapter 3 were related to changes in microstructure. This was accomplished by using samples with pre-existing crack networks produced via thermal shock cycles.

The presence and extent of the crack networks were characterized by Lo *et al.*[60]. Mechanical response analysis showed that a material with physical damage could recover reduced stiffness by mechanisms such as crack closure. It was also found that Young's modulus could not just recover but increase past quasi-static value. By computing the shear modulus from observed Young's modulus and Poisson's ratio it was found that the shear modulus would consistently be less than its quasi-static value at failure. In Chapter 2, the shear wave speed was determined to be of importance to the failure processes in impact, and so Chapter 2 and Chapter 4 have links with respect to the importance of shear failure in ceramics. Shear modulus change was deemed of high importance to track in subsequent studies.

- Chapter 5 explored the mechanical responses of two grades of boron carbide across a range of strain-rates, motivated by the unexpected behavior of AD-995 and SiC in having an increasing apparent Young's modulus seen in Chapter 3. Both forms of boron carbide demonstrated increases in apparent Young's modulus during the failure process, but one grade did not exhibit this behavior consistently. The grade of interest was the stronger and stiffer of the two boron carbides, and the inconsistency in failure behavior was related to the strain-rate. At lower strain-rates, no change in Poisson's ratio was observed during failure and Young's modulus decreased along with shear modulus. At higher strain-rates, Poisson's ratio increased during failure, which explains how Young's modulus can increase even as shear modulus decreases. Prior theory commonly used in the literature had been based upon quasi-static observations where changes to Poisson's ratio were not significant. As such these observations suggest that there is a transition from quasi-static type damage accumulation to dynamic type damage accumulation. This transition appears related to the baseline properties of a material. A higher stiffness appears to correlate with a higher quasi-static to dynamic transition strain-rate. This discovery integrates prior findings in this thesis and the literature.

Chapter 2 - Influence of Microstructure on the Impact Failure of Alumina

2.1. Introduction

The study of the dynamic failure of ceramics is an area of active research, owing to the fact that ceramics have properties under high strain rate loading that make them ideal for incorporation into anti-ballistic protection systems. In addition to high hardness that can blunt and erode projectiles[5], one of the key properties of ceramics that makes them appealing is the way that they demonstrate increasing strength with increasing strain rate[8,21,52,61–64]. Various experimental studies done to determine material properties such as fracture toughness, density, elastic modulus, crack speed, also show that these properties can change with increasing strain rate[27–31]. A key question for modelers and designers are how these properties and their rate-dependencies are controlled by the microstructure of these materials. For example, defects, such as secondary inclusions and pores, serve as favorable failure nucleation sites, but in quasi-static conditions may not influence properties as strongly as under dynamic conditions. The orientation of defects also influence the failure of a ceramic, as modelled by Hu *et al.*[36] and observed experimentally by Hogan *et al.*[37] Two materials can also have the similar quasi-static properties but divergent properties as strain rate increases, such as in impact or compression bar experiments. A material deemed to have superior qualities under quasi-static testing may also prove inferior under dynamic conditions. An example of a ceramic with superior quasi-static fracture toughness but inferior dynamic fracture resistance can be found in the experiments of Arab *et al.*[33]. In their tests, the addition of strontium carbonate to zirconia toughened aluminum oxide (ZTA) increased the fracture toughness when added at an optimal quantity by forming a secondary phase at the grain boundaries, but this also increased the porosity of the material. When performing dynamic testing via Kolsky bar, all of the specimens with strontium carbonate had inferior strength to pure ZTA, with the authors attributing the poor dynamic performance to the added porosity induced. These tests demonstrate the complexities between microstructure and strain-rate dependent mechanical properties.

For armor applications, aluminum oxide (alumina) is of particular interest owing to it being both a suitably hard and lightweight ceramic, as well as being inexpensive to produce on an economical scale. The high availability of materials and equipment capable of producing alumina allows for increased capacity to experiment with additives [33,34,65–67]. The ease of production opens up new manufacturing options such as 3D printing [68–70], with the work of Jones *et al.* in examining 3D printed alumina body armor [69] being of particular interest. In their study they compared the microstructure and dynamic performance of both their 3D printed materials and a standard hot pressed alumina ceramic. In quasi-static characterization, they found that the 3D printed alumina had more variability in its density, had lower flexural strength, and higher hardness, with scanning electron microscope work showing that the 3D printed material had fewer pores, but the pores had a larger size. Further tests with armor piercing rounds examined the depth of penetration and residual mass of the penetrator for the two aluminas and found that the 3D printed alumina performed worse in these ballistic tests. The authors attributed the lower performance of the 3D printed alumina primarily to the lower flexural strength and the larger pore sizes encountered in the 3D printed material. Combined, this demonstrates some of the connections between microstructure and the ballistic performance of advanced ceramics.

In contrast with performing multiple tests on one material, one can also perform the same test on multiple materials to understand what is occurring. Differences in mechanical response correspond to differences in physical properties that arise from chemical composition or microstructural differences. An example of this and in how advancements in diagnostic techniques improve impact experiments is demonstrated by the extensive work of Elmar Strassburger in edge-on-impact (EOI) experiments. Over the past decade and a half, Strassburger *et al.*[39–43] has shed light upon how damage propagates within ceramics by using high speed cameras to observe how damage grows across the surface of opaque ceramics, as well as in the interior of transparent materials. One particularly notable result of these experiments is that the speed at which damage propagates occurs within two general regimes in impacts that generate shocks below the Hugoniot elastic limit. The first regime has crack speed increase with increasing impactor velocity, while the second regime features crack speed not increasing as significantly with increasing impactor velocity, with this plateauing velocity being associated with some fraction of the speed of sound within the ceramic[39]. Since the speed of sound directly relates to the stiffness of the material, this means that stiffer materials propagate damage more quickly. With the speeds of sound in advanced ceramics above 8 km/s and tile thicknesses typically measured in millimeters, this means that damage events take place in hundreds of nanoseconds to just a few microseconds.

Building on past works, this paper examines two grades of alumina through microstructural characterization, mechanical testing, and impact testing, using multiple data acquisition methods for all tests to increase the breadth of information gathered and the number of comparisons that can be made. In microstructural characterization activities, multiple characterization techniques give precise data on the physical dimensions and chemical composition of individual and aggregate microscale features. In mechanical characterization activities, quasi-static and Kolsky bar testing is performed to evaluate rate-dependent strength and failure behaviors. In impact testing, the high-speed acquisition of visual, X-ray, and deformation velocity data simultaneously allows for the correlation of events in one data set to events in another. From there we link together phenomena such as material failure to strains that could not be previously observed simultaneously at these speeds. The speed of data acquisition also allows for microsecond resolution of differences in behavior between a ceramic tile that defeats or is penetrated by a projectile. Finally, by combining microstructural information and impact data, an increased understanding of how the former affects the latter becomes possible.

2.2. Experimental Setup

2.2.1. Materials and Characterization

This experimental series utilized two different grades of alumina, AD-85 and AD-995, both provided by CoorsTek Engineered Ceramics, with Table 2-1 listing the relevant mechanical properties provided by the manufacturer. The numbers 85 and 995 refer to the percentage of the material that is alumina (85% and 99.5%, respectively), with the remainder being binding agents or trace impurities. For all of the qualities listed in Table 2-1, the manufacturer lists AD-995 as having higher numerical values than AD-85. The differences in properties are attributed to microstructural and chemical differences between the two materials, with other characterization performed in this study to probe these differences. The samples were machined into cuboids of dimensions of 3.5 mm X 2.7 mm X 2.5 mm for use in quasi-static and dynamic testing. These sizes were chosen to conform with prior samples, but reduced in dimensions in order to produce higher pressures with less force used, particularly in Kolsky bar experiments. In this paper, the quasi-static compressive strength and Young's modulus were independently examined using a MTS 810 materials testing machine and both grades of alumina were found to have properties in line with those described by the manufacturer.

Table 2-1 – Key properties for AD-85 and AD-995

	AD-85	AD-995
Flexural Strength (MPa)	296	375
Elastic Modulus (GPa)	221	303
Compressive Strength (MPa)	1930	2068
Hardness (Rockwell 45 N)	73	78
Fracture Toughness (MPa $m^{1/2}$)	3 - 4	4 - 5
Poisson's Ratio	0.22	0.22
Density (g/cm^3)	3.42	3.9
Calculated Transverse Wave Speed (m/s)	8,000	10,000
Calculated Shear Wave Speed (m/s)	5,100	6,200
Crack Speed (Dynamic Compression) (m/s)	1800 ± 600	2200 ± 400
Crack Speed (Impact) (m/s)	4600 ± 1800	4800 ± 1300

In addition to quasi-static testing, additional characterization was done using a Kolsky bar testing apparatus to obtain stiffness and strength values and a Shimadzu HPV-X2 ultra-high-speed (UHS) camera was coupled to the experiments to obtain crack speeds. The Kolsky bar apparatus used incident and transmitted bars 12.7 mm in diameter made of maraging steel (Service Steel America C-350) with a Young's modulus of 200 GPa, Poisson ratio of 0.29, yield strength of 2.68 GPa, and a density of 8100 kg/m^3. A projectile made from the same steel was launched using compressed gas to strike an incident bar, which then transmitted the strain pulse into a sample of alumina, with another bar receiving the remaining stress pulse from the event. A copper pulse shaper was used in these tests, as recommended in literature[61,71]. This set up allowed for strain rates of 10^2 to 10^3 s^{-1} to be produced.

Multiple techniques were used for microstructural characterization to study properties such as grain size and the chemical composition of individual grains and impurities. Initial examination of physical microstructure was done via SEM (FEI Nova NanoSEM 600). Electron backscatter diffraction (EBSD) (TEAM Pegasus Integrated EDS-EBSD) was used to determine the crystallographic orientation of the grains within the microstructure. This gave information about whether the grains had a preferred orientation or if they were randomly oriented. EBSD in conjunction with SEM also determined the size and shape distributions of the grains. Energy-dispersive X-ray spectroscopy (EDS) (TEAM Pegasus Integrated EDS-EBSD) was used to determine the elemental composition and distribution, and could focus upon individual grains or impurities to determine their individual composition, rather than the average composition of an ensemble of grains and intergranular material. Together SEM, EBSD, and EDS produced information on the sizes, shapes and compositions of individual alumina grains, as well as the presence and composition of intergranular materials such as amorphous phases or agglomerated impurities.

2.2.2. Impact Setup

Figure 2-1 shows the impact set-up with a variety of sensors trained upon a target, with a full description given previously in Jannotti *et al.*[72]. Impact experiments used spheres 6.4 mm in diameter of tungsten carbide (WC) impacting 6.4 mm thick and 38.1 mm diameter discs of alumina held within polycarbonate (PC) holders. The WC spheres were held in PC sabots and fired from a 7.62 mm smoothbore powder gun, with velocity varied based on powder load. Striking velocity was determined by light screens a fixed distance from the target and verified by a photo-Doppler velocimetry (PDV) probe just ahead of the target. A range of velocities were tested, but for this study the impact velocity of ~400 m/s is of greatest interest and shall be the focus of discussion. At 400 m/s, the projectile completely penetrates AD-85 but is defeated by AD-995, and thus attention in this paper focuses on studying this outcome. The impact velocity of 400 m/s chosen is based on EOI experiments done by Strassburger *et al.*[39] where the damage velocity in alumina were shown to be related to both the speed of sound of the materials and the velocity of the impacting projectile. For the alumina materials studied in the Strassburger work[39], the general behavior observed had an initial rise in damage propagation speeds before reaching some plateau value. For the 98% pure alumina used in that study, velocities greater than 200 m/s were beyond this transition point of 5500 m/s to 9500 m/s for the damage velocity, and so we selected 400 m/s for our impact experiments to avoid this transitional behavior at lower velocities.

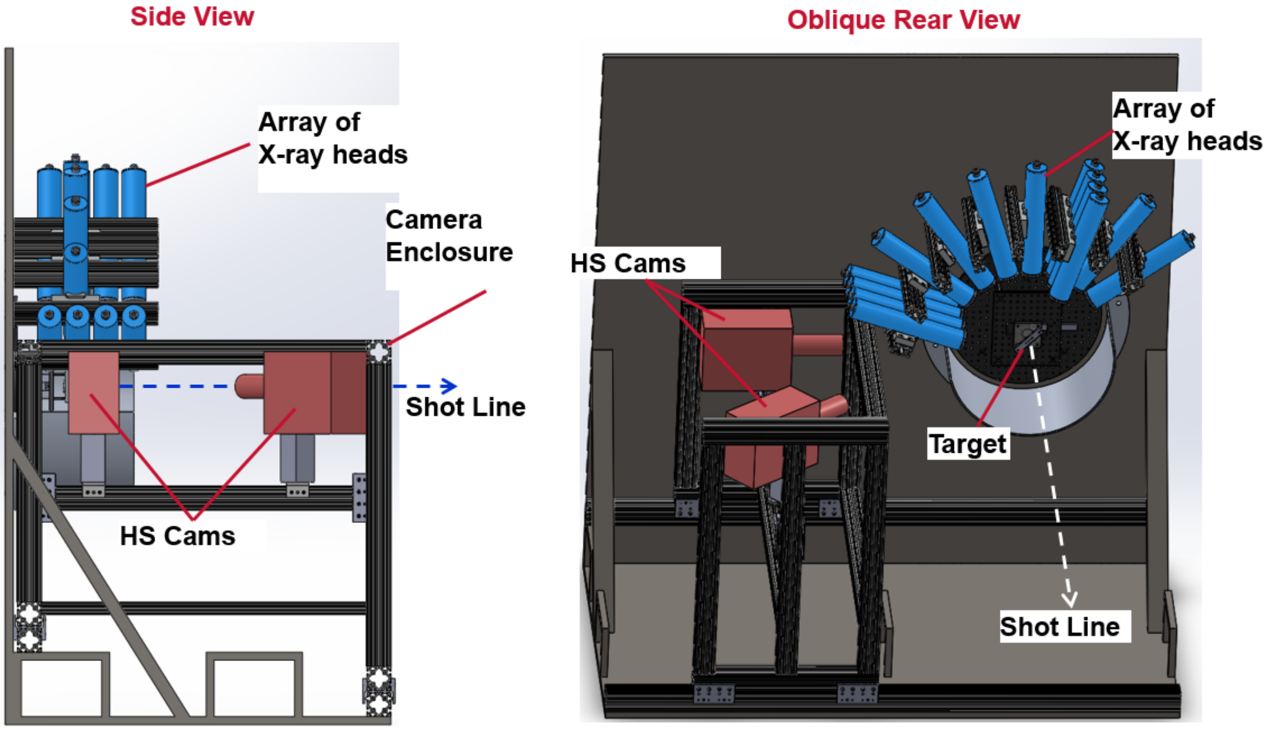

Figure 2-1 – Impact experiment set-up, showing the arrangement of high-speed cameras and X-ray heads in relation to the target and shot line. Also present are PDV laser probes trained upon the rear of the target. Description previously given in Jannotti et al.[72]

During testing, the target failure response was characterized using a range of *in situ* diagnostics, including UHS cameras sampling at 2 MHz (Shimadzu HPV-X), 8-head flash x-ray tubes (L3 Communication 150 kV tubes)[73], and back face PDV probes (AC Photonics 1CL15A070LSD01-5m). PDV is a method whereby the velocity of an object is measured by detecting the Doppler shift in frequency of a laser reflected off of the target[74] and is able to detect changes of m/s to km/s over time scales of nanoseconds to microseconds[75]. Triggering for the diagnostics was provided by a break screen adhered to the target surface that registered the impact and began the various sensors recording. This set up means that the delay between impact and the beginning of all sensors recording is on the order of 100 nanoseconds or less, much less than a single frame of UHS video at 2 MHz, so there is high confidence that events recorded synchronize up with each other.

2.3. Experimental Results

2.3.1. Microstructure Results

The microstructure analysis helps to explain the observed mechanical properties and impact behavior of both grades of alumina by showing how their composition and grain structures differ. SEM images like those shown in Figure 2-2 show the general microstructure of AD-85 and AD-995 and allows for comparison between the two. From SEM images the grain sizes were determined as 3.0 ± 0.3 µm for AD-85 and 8.0 ± 3.0 µm for AD-995. Outside of the grains, there are two other types of features seen in SEM images. The first are dark features, and the second are lighter areas that fill the irregular spaces between the grains. In AD-85, the dark features are larger than the average grain size, containing features resolvable at the magnification used, and appear separate from the grains. Comparing AD-995 and AD-85, AD-995 also has a lower presence of intergranular material, with most grains in direct contact with other grains.

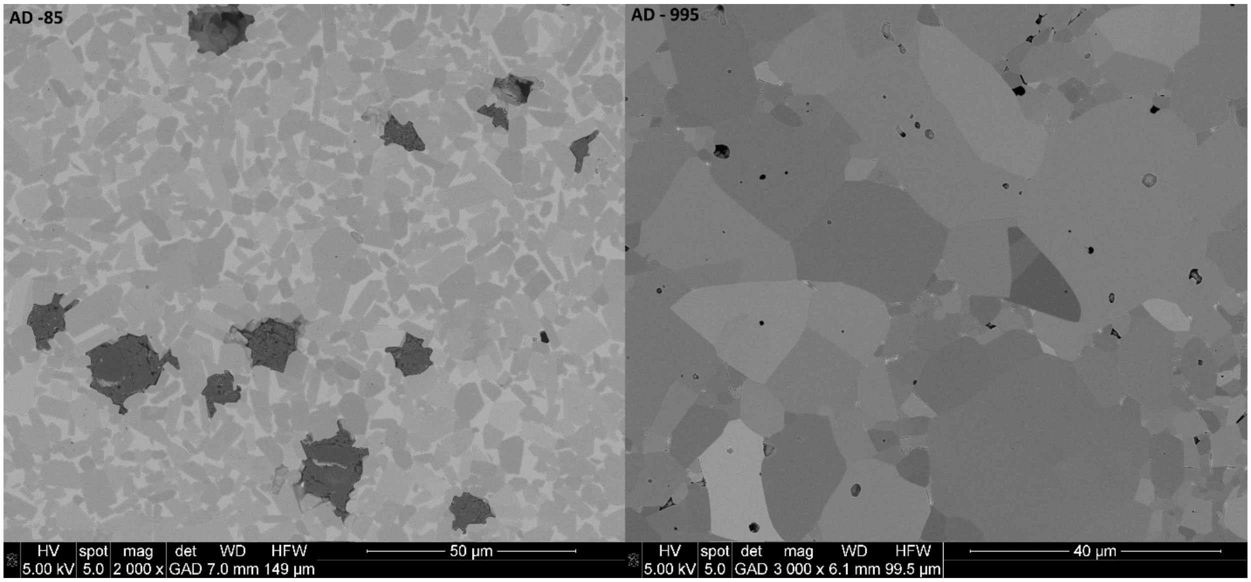

Figure 2-2 – SEM images of AD-85 (left) and AD-995 (right), showing the sizes and shapes of microstructural features in both grades of alumina. Present within AD-85 are large inclusions that appear dark under SEM, as well as lighter regions that exist between grains, confirmed with XRD to be amorphous silicate phases. These glassy phases are expected from prior work in the literature[76]. Dark spots are also present within AD-995, but are significantly smaller and appear to be contained within grains rather than between them. The average grain sizes are 3.0 ± 0.3 µm for AD-85 and 8.0 ± 3.0 µm for AD-995.

Figure 2-3 shows EDS maps of the various elements in AD-85, showing that the dark areas observed in the SEM images detected as carbon rich and have a significantly lower content of other elements present elsewhere. To further probe these dark features, SEM examination of fragments in Figure 2-4 shows that AD-85 has significant numbers of internal pores, and we believe these correspond to the dark areas seen in the SEM images of the flat surfaces. As a result of this, the carbon seen in Figure 2-3 is most likely caused by hydrocarbon compounds used in sample cleaning and preparation becoming entrapped within the deep pores instead of being removed from the surface. Next, we explore the intergranular material observed in the SEM images corresponding to areas of low to no aluminum (Figure 2-3, comparing Frame B and C), and the presence of silicon (Figure 2-3, Frame E) and calcium (Figure 2-3, Frame G). Magnesium (Figure 2-3, Frame F) appears to be primarily present as a contaminant bound within alumina grains rather than in-between grains. Prior examinations by Brandon *et al.*[76] have shown AD-85 to be composed of α-Al_2O_3 (corundum), with $MgAl_2O_4$ (magnesium spinel) and $CaO \bullet Al_2O_3 \bullet SiO_2$ (anorthite), with up to 20% of the material being a glassy phase between grains[76]. This composition corresponds to our findings in Figure 2-2 and Figure 2-3.

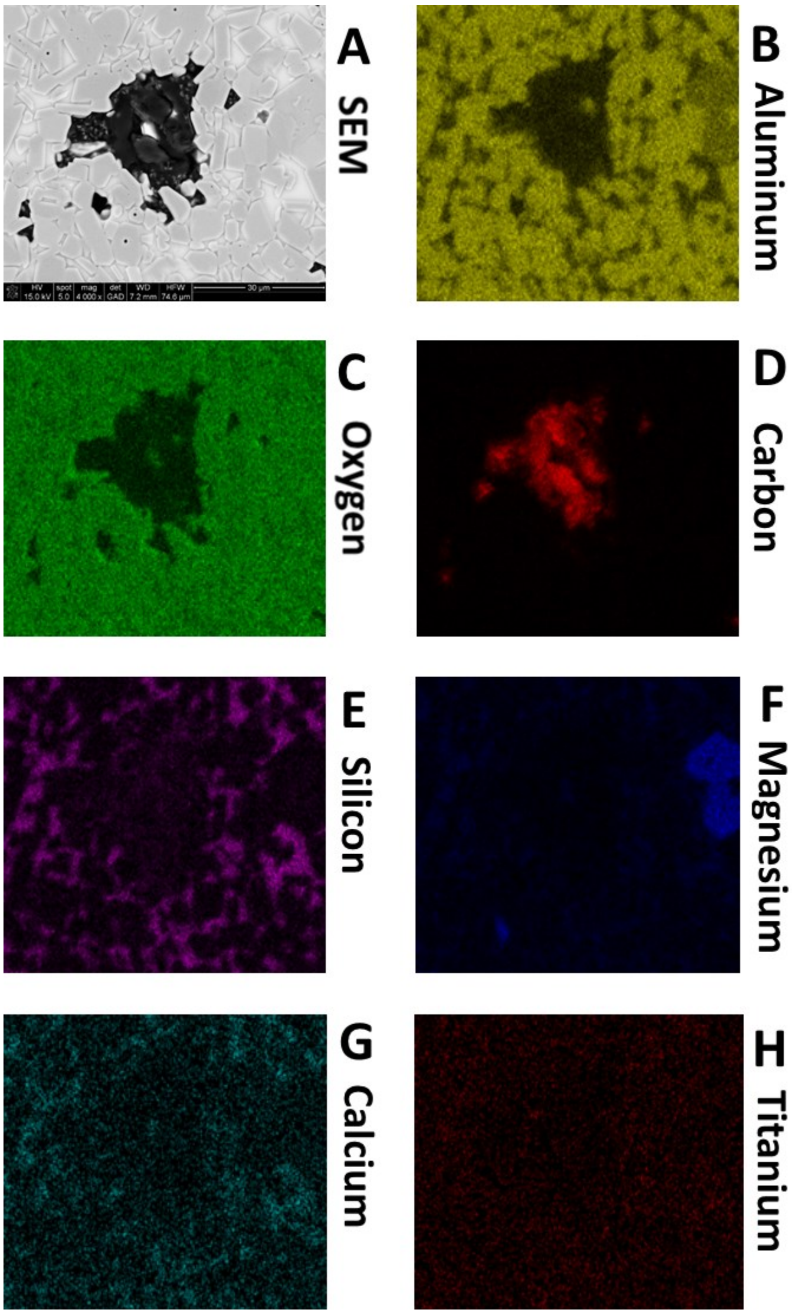

Figure 2-3 – SEM and EDS images of AD-85 showing the chemical composition of the grains, intergranular material, and impurities. Frame A: SEM image of an impurity surrounded by grains and amorphous regions. B: EDS map of the distribution of aluminum, showing that it is concentrated in the grains but not the intergranular areas. C: EDS map of the distribution of oxygen, showing that it is present everywhere except for the dark spots in the SEM image. D: EDS map of the distribution of carbon, showing its concentration in the dark areas of the SEM image. These were shown to be caused by carbon materials from prep work remaining within pores seen in Figure 2-4. E: EDS map of the distribution of silicon, showing that it is concentrated in the intergranular areas. F: EDS map of the distribution of magnesium, which is weakly scattered in the intergranular areas but also concentrated in what appeared to be a regular cluster of grains in the SEM image. G: EDS map of calcium. H: EDS map of titanium, showing that it is randomly distributed in trace amounts throughout the microstructure.

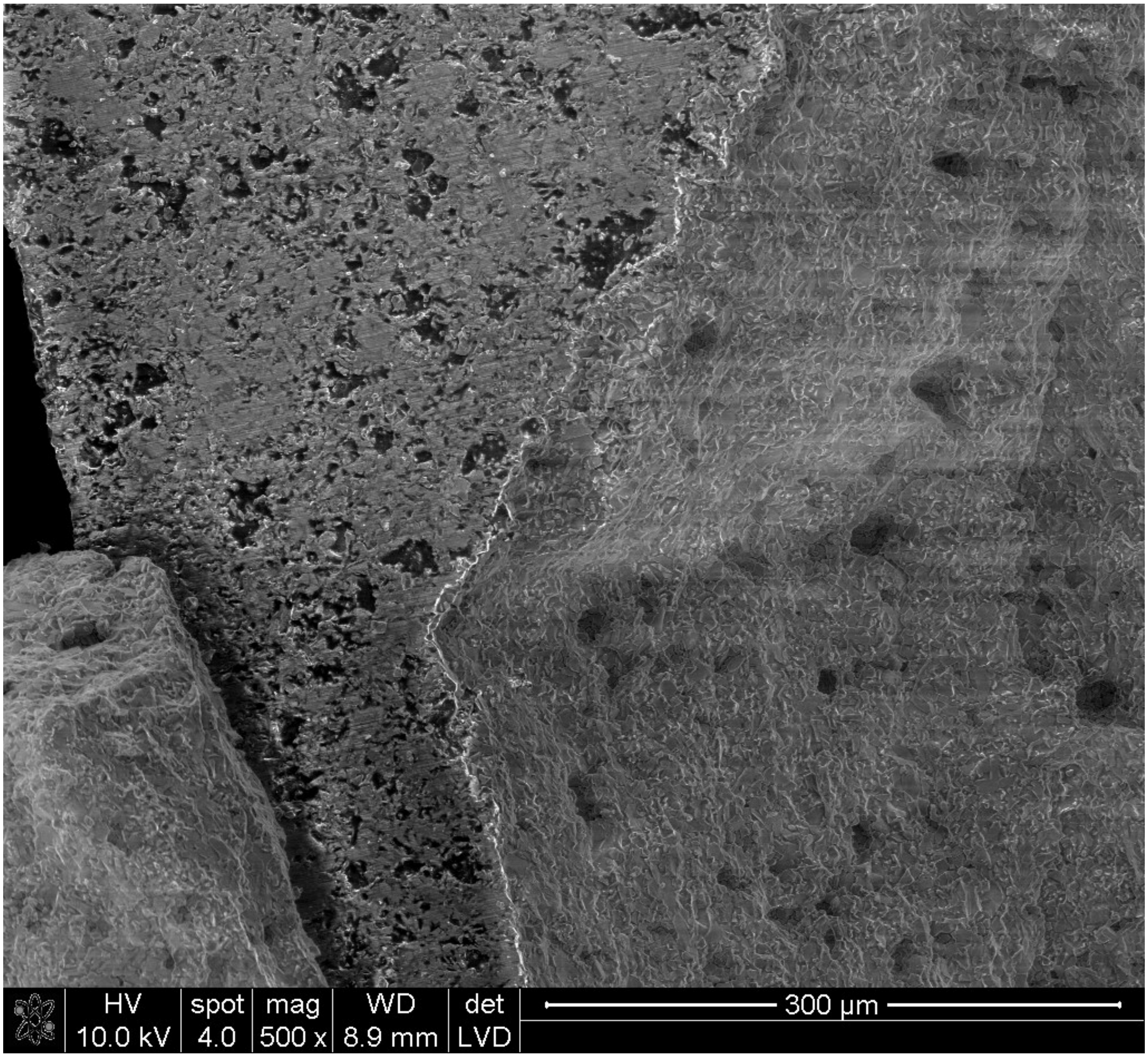

Figure 2-4 – SEM image of an AD-85 alumina fragment generated in a quasi-static crush test, showing a polished surface on the left side of the image and a fragmented surface on the right side of the image. The dark spots on both sides of the image are confirmed as pits caused by porosity.

Next, we consider the AD-995 case, where Figure 2-5 shows EDS maps for AD-995, showing almost uniform distribution of aluminum (Figure 2-5, Frame B) and oxygen (Figure 2-5, Frame C), with all other elements falling beneath the detection levels at the resolution presented. Areas where the primary elements are of lower concentration correspond to features on the SEM image such as grain boundaries and grain pullouts from polishing. Table 2-2 lists the overall elemental composition of the AD-85 and AD-995 samples as determined by EDS, both in terms of weight percentage and atomic percentage. Atomic percentage is particularly useful for comparing the ratios of aluminum to oxygen as in pure alumina there should be a 2:3 ratio between the elements, and an excess of atomic percentage of oxygen would indicate oxide contaminants, while an excess of aluminum would indicate metallic contaminants. From Table 2-2, AD-85 is primarily composed of aluminum and oxygen mixed with traces of magnesium (1.0 atomic %, 1.3 weight %), silicon (3.8 atomic %, 3.8 weight %), calcium (0.3 atomic %, 0.7 weight percentage) and a large carbon content (22.7 atomic %, 14.9 weight %). By considering individual grains, we observe oxygen content of 55.8 atomic % and aluminum 31.3 atomic %, which suggests that the 85% alumina purity given by the manufacturer is accurate. Given the EDS mapping, the metallic impurities are likely present as oxides and formed as binders between alumina grains produced by the liquid phase sintering processed used to produce the material. For AD-995, the composition appears to be almost entirely of aluminum and oxygen, as expected of aluminum oxide, with only 0.1% of atoms being silicon. This value is less than the 0.5% implied by the name AD-995, although as the silicon is present as silicon dioxide (silica), so some portion of the oxygen detected is not part of the alumina.

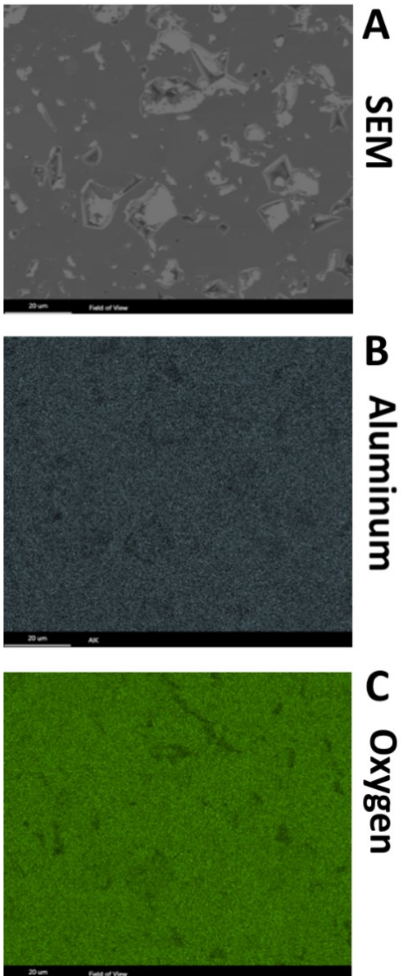

Figure 2-5 – SEM and EDS of AD-995 showing the chemical composition of the grains and intergranular material. Frame A: SEM of a polished surface of AD-995. Frame B: EDS map of the distribution of aluminum, showing that it is distributed evenly across the surface. Frame C: EDS map of the distribution of oxygen, showing that it is distributed evenly across the surface. Other elements are present in quantities too low to be detected at the relevant resolutions, confirming that the material is 99.5% alumina.

Table 2-2 – Elemental composition of AD-85 and AD-995 as determined by EDS

	AD-85	AD-995
Element	Atomic % (Weight %)	Atomic % (Weight %)
Carbon	22.8 (14.9)	0.00
Oxygen	48.4 (42.3)	59.5 (46.6)
Magnesium	1.0 (1.3)	0.00
Aluminum	25.0 (36.8)	40.3 (53.2)
Silicon	2.4 (3.8)	0.1 (0.2)
Calcium	0.3 (0.7)	0.00
Titanium	0.1 (0.3)	0.00

Figure 2-6 shows EBSD maps for AD-85 and AD-995. These images show the crystallographic orientation of the grains at the surface of the examined samples. For both grades of alumina, there appears to be no preferred orientation, and these images are also used to establish grain sizes and shapes. AD-995 has an average grain size of 8.0 ± 3.0 μm, and AD-85 has an average grain size of 3.0 ± 0.3 μm, noting that a significant amount of the AD-85 material is in the glassy binder phase. The images were chosen for clarity, with the amorphous material seen in SEM images of AD-85 not well represented in Figure 2-6.

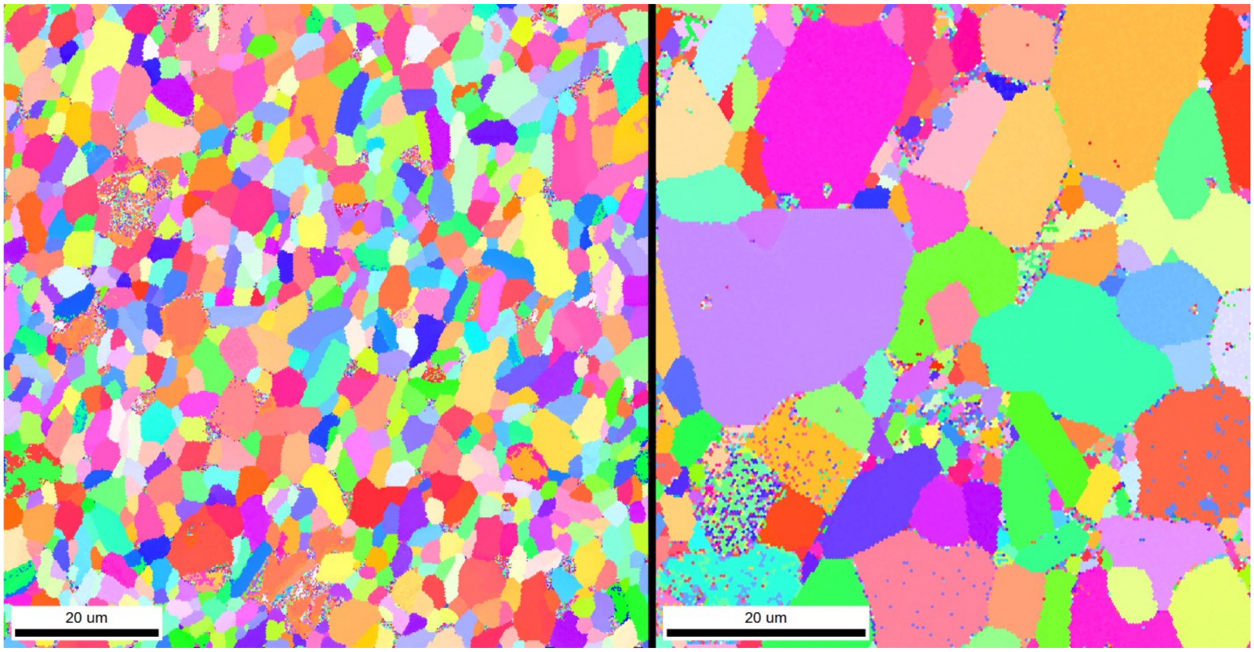

Figure 2-6 – EBSD maps for the two different types of alumina, showing the polycrystalline nature of the samples and the differences in grain size and grain size distribution between the two. A map for AD-85 is visible on the left with grain sizes of 3.0 ± 0.3 µm and a map for AD-995 on the right with grain sizes of 8.0 ± 3.0 µm.

2.3.2. Strain Rate Dependencies

Figure 2-7 shows the compressive strength of AD-85 and AD-995 as a function of strain rate. Low strain rate measurement comes from the quasi-static testing (2.0 ± 0.1 GPa for AD-85 and 2.4 ± 0.2 GPa for AD-995), while higher strain rate measurement comes from Kolsky bar testing (2.6 ± 0.3 GPa for AD-85 and 3.6 ± 0.5 GPa for AD-995). While the quasi-static testing shows strengths in agreement with those of the manufacturer, under dynamic compression experiments the strength at failure generally increases by a factor of 1.5 for both AD-85 and AD-995. The rate sensitivities (acquired 2016) are consistent with those from previous versions of alumina materials [29,31,77,78].

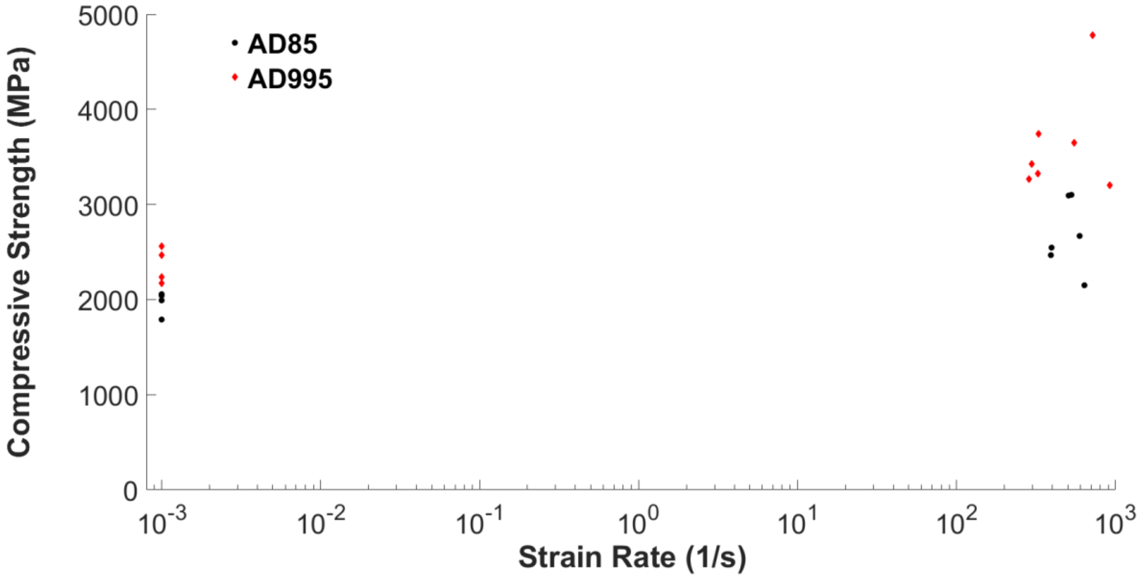

Figure 2-7 – Strength vs. strain rate plot for AD-85 and AD-995, showing the change in strength from quasi-static conditions at 10^{-3} s^{-1} strain rate to dynamic conditions between 10^2 and 10^3 s^{-1} from Kolsky bar experiments.

In addition to acquiring strength measurements, we have also visualized dynamic failure during Kolsky bar testing. Figure 2-8 shows a sequence of images of a sample of AD-85 alumina being compressed to failure, where images are selected to demonstrate: Frame A, no load; Frame B, peak stress and the beginning of cracking and chipping; Frame C, no stress and the development of long axial cracks; and Frame D, the cracks after coalescence and the material starting to pulverize. Figure 2-9 shows the same sequence of events for AD-995. The primary difference between AD-85 and AD-995 is that crack speed measurements can only be taken of the large singular cracks before crack coalescence.

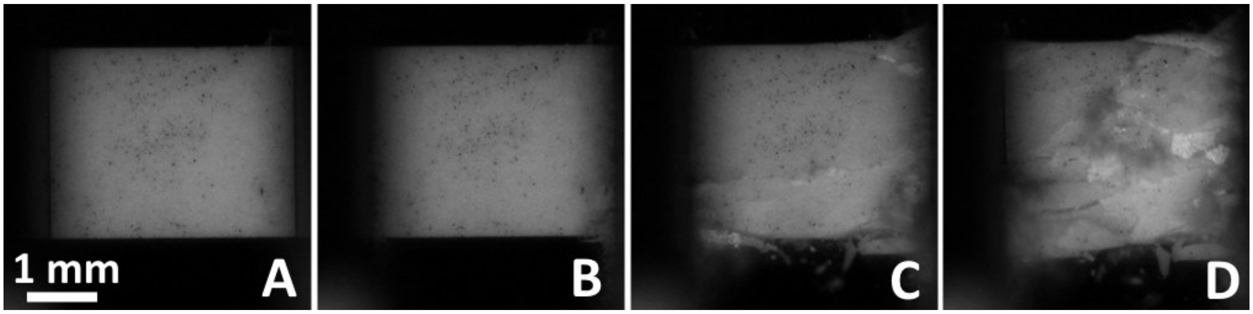

Figure 2-8 – Sequence of images from a representative sample of AD-85 compressed to failure in a Kolsky bar. Frame A shows the uncompressed, pristine sample 0 μs into the event. Frame B shows the beginning of minor cracking and chipping at one corner that occurs as peak stress is reached at 42 μs. Frame C shows a well-developed axial crack at 50 μs into the event, along with the continued cracking and chipping at the corners. At this point that sample has failed and is no longer supporting stress. Frame D shows the sample disintegrating as the cracks coalesce.

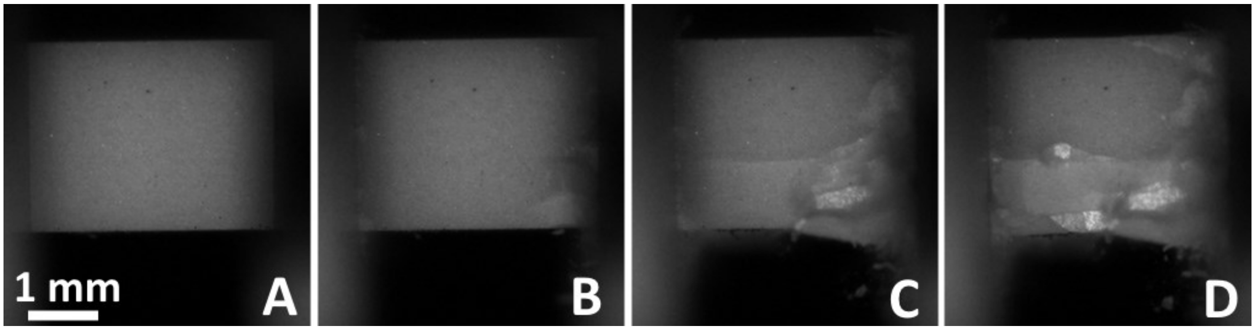

Figure 2-9 – Sequence of images from a representative sample of AD-995 compressed to failure in a Kolsky bar. Frame A shows the uncompressed, pristine sample 0 µs into the event. Frame B shows the beginning of minor cracking and chipping at one corner that occurs as peak stress is reached at 45 µs. Frame C shows a well-developed axial crack at 55 µs into the event, along with the continued cracking and chipping at the corners. At this point that sample has failed and is no longer supporting stress. Frame D shows the sample disintegrating as the cracks coalesce. The samples AD-995 go through a similar sequence of events.

When measuring crack speeds, AD-85 has a crack growth pattern that is tracked at 1800 ± 600 m/s. AD-995 in contrast shows a much greater extent of small cracks, with its large cracks often propagating across the entire face of the sample in a single frame. This places a lower bound of these sorts of cracks with a velocity of 3500 m/s, but they could conceivably be higher and it would not be measurable using the acquired framerates in these videos. It is also possible that the cracks grow in such a way that they are not visible until they are already well developed. From the available data, an estimate of 2200 ± 400 m/s is determined for the crack speeds in AD-995. These measurements highlight how the vastly different microstructures manifest in strength and crack speed measurements, and this will be important when comparing impact results.

2.3.3. Impact Results

Next, we contrast the behavior of the two materials during impact testing for a selected velocity where the AD-85 did not defeat the projectile and the AD-995 defeated the projectile. Here, only the AD-995 is shown for brevity. A sequence of high-speed video images in Figure 2-10 shows the initial progression of failure during impact testing, as captured by high-speed back face videos for AD-995. The first image is the first frame in which radial cracking becomes visible at 4.1 µs after impact. By tracing the growth of several crack tips (N=8 for both materials) frame-by-frame from the moment they are visible to when they are no longer traceable, they are found to have average radial crack speed of 4800±1300 m/s, significantly higher than the crack speeds observed in uniaxial compression in Kolsky bar testing. The second image in Figure 2-10 is at

5.1 μs after impact when the radial cracks are well developed. The final image at 7.6 μs after impact is when an inward radiating phenomenon visible as a darkening of the alumina makes contact with the radial cracks. This phenomenon is believed to be the holder delaminating from the alumina target, and any further growth of radial cracks is not observable past this point. Although not shown, at 12.1 μs the PC backing begins to radially crack, completely obscuring the activity in the alumina. A similar sequence of events occurs for AD-85, with radial crack speeds of 3800±1000 m/s, also higher than for Kolsky bar testing.

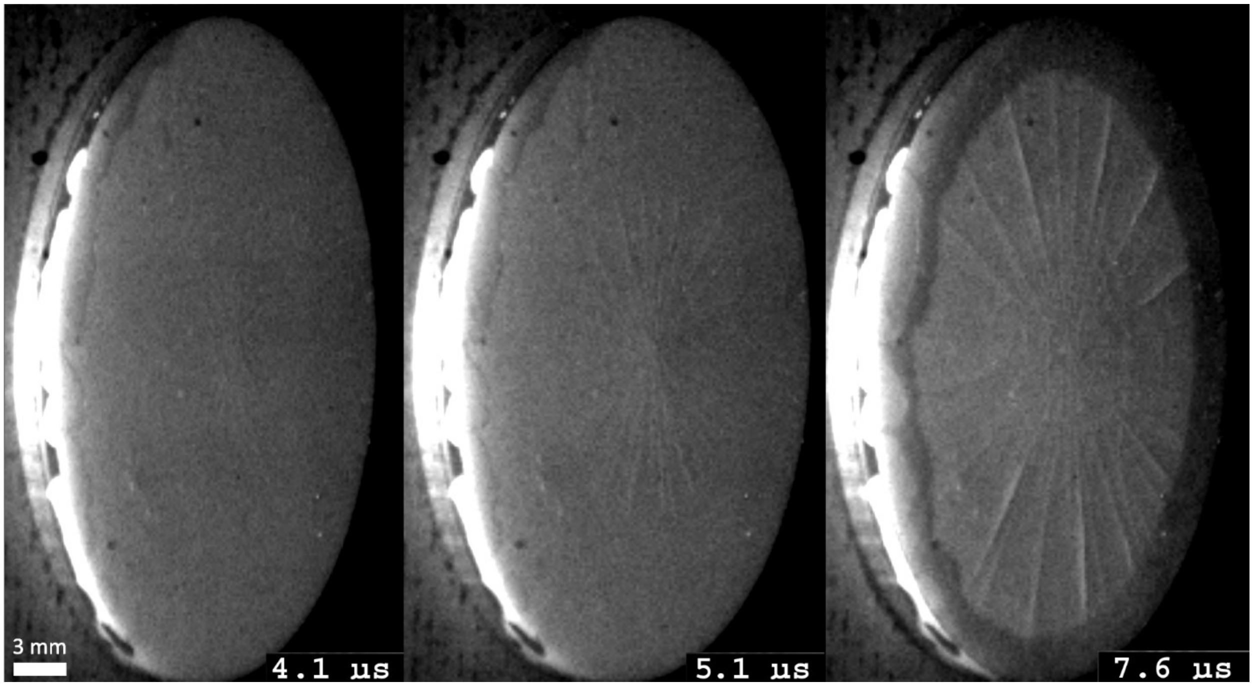

Figure 2-10 – Key frames from the AD-995 impact, showing the initial radial cracking at 4.1 μs, the radial cracks well established at at 5.1 μs, and at 7.6 μs when radial cracks have reached their maximum measurable extent and delamination has begun at the edges. Radial crack speeds are 4800±1300 m/s

Figure 2-11 shows a selection of flash X-ray images of the projectile interacting with AD-995 at the impact velocity of 400 m/s. In the first frame at 0 μs the projectile can be seen as a distinct circle. In the second frame at 5 μs the bottom has flattened out. For the third frame at 10.1 μs the flattening process has begun to affect the curvature of the back of the projectile. Finally, at 25.2 μs the projectile is almost completely flat. This sequence shows how a spherical projectile undergoing interface defeat behaves, and importantly it demonstrates that by 5 μs it has already begun to flatten. AD-995 not shown for brevity.

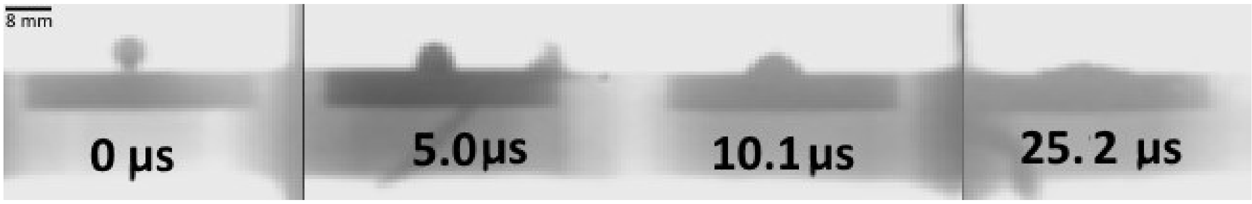

Figure 2-11 – Series of flash X-ray images showing the progression of the interaction between the projectile and target. At time 0 µs the projectile has made contact with the target and shows a circular shape, indicating that has not undergone deformation from its initial spherical shape. By 5.0 µs after impact, the projectile is already showing considerable deformation and by 25.2 µs after impact it is nearly flat, demonstrating interface defeat.

Figure 2-12 shows the PDV traces for AD-85 and AD-995, and, when linked with high-speed videos and X-ray images, gives important information on the sequence of events during impact. At a projectile velocity of 400 m/s these traces are particularly important as AD-85 is penetrated by the projectile while AD-995 defeats the projectile, so the differences between the two traces provides evidence for differences in behavior between defeating and not defeating a projectile. Between 2.5 µs and 6 µs the back face undergoes primary acceleration at an average rate of 45 $m/\mu s^2$. It reaches a peak velocity of 168 m/s at 6.0 µs. The velocity then undergoes an average deceleration of -24 $m/\mu s^2$ to 100 m/s by 10 µs, at which point interference from the holder makes further data unusable. For AD-995, the velocity trace remains close 0 m/s for 4.0 µs before it begins to accelerate at an average rate of 78 $m/\mu s^2$. A peak velocity of 133 m/s is reached at 5.8 µs. The back face velocity then decelerates at an average rate of -45 $m/\mu s^2$, reaching 20 m/s by 10 µs, at which point PC delamination begins interfering again. With all of the information available from characterization and impact experiments, it then becomes possible to begin correlating together the microstructure, strain-rate dependent compression measurements, high-speed video, flash X-ray, and PDV traces to examine the properties of a ceramic that can aid in the defeat of a projectile. This is done in the discussion.

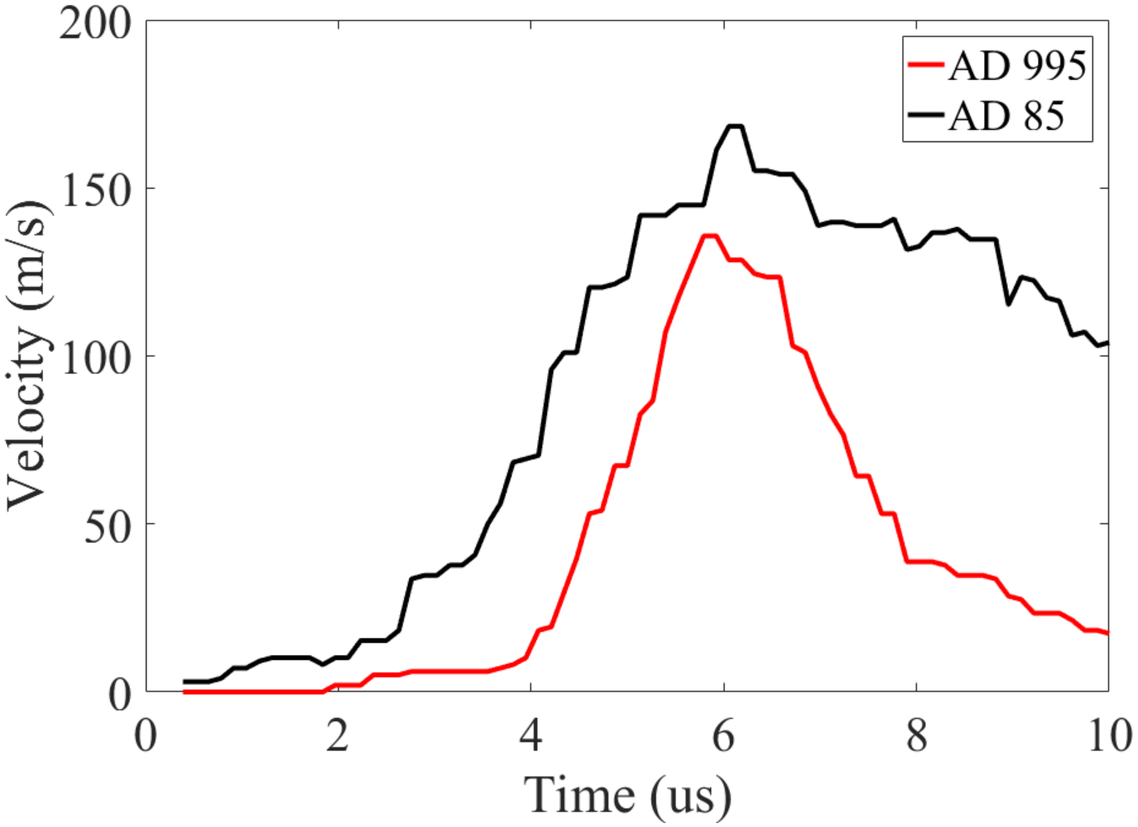

Figure 2-12 – PDV traces for AD-85 and AD-995 over the first 12 μs. Peak velocity corresponds to the time of highest stress and thus the decrease in velocity corresponds to a relaxation of stress, an indicator of material failure. For both traces the rise in velocity around 10 μs is associated with delamination of the alumina target from the PC backing and subsequent interference, and the point at which the data can no longer be considered valid.

2.4. Discussion

2.4.1. AD-85 and AD-995 Compared

We have investigated the chemical and microstructural composition of the two different grades of alumina, and observed how they behave mechanically under quasi-static, dynamic, and impact loading. We have found that AD-995 has larger grain sizes but far fewer chemical impurities and physical defects such as pores and intergranular material than AD-85 has. Mechanically this manifests as greater strength at failure, higher Young's modulus, and greater resistance to penetration by an impactor for AD-995 over AD-85. We will now explore more of the mechanisms that would produce these particular results.

We begin by looking at the differences in microstructure and how they are expected to contribute to differences in performance. For AD-85 the presence of intergranular inclusions and porosity provide crack nucleation sites, while the amorphous phase is less cohesive than alumina grains in direct boundary contact with each other. Landingham and Casey[35] determined that while smaller grain sizes in ceramics were superior for ceramics resisting penetration by high velocity projectiles, there were four other microstructural features that would negatively affect this performance. These features were: 1) porosity between ~1-5 vol%, 2) greater than 2 vol% of finely dispersed impurities, 3) small amounts of features such as larger than average grains or agglomerated impurities, and 4) greater than 10 vol% of highly elliptical grains. While having smaller grains, AD-85 has both a significant presence of finely dispersed impurities and large impurities. Together, these are believed to contribute to inferior performance.

Supporting the effects of porosity being greater than grain sizes, Longy and Cagnoux[27] also found for alumina that while grain size played a role in the strength at the Hugoniot elastic limit (HEL), porosity played a greater role in determining the HEL than grain size or chemical purity. Their flyer plate tests showed that alumina of different chemical purity had the same HEL so long as the percentage volume porosity was similar. Of particular interest was that when examining post-mortem fragments with high resolution microscopy, Longy and Cagnoux[27] observed little transgranular cracking or microplastic deformation such as twinning within the alumina, with the primary mode of cracking being intergranular and within amorphous glassy phases when present. For AD-85 with its large amounts of amorphous intergranular phases, this becomes an important mechanism in producing a less strong material with inferior ballistic performance. More recent work with alumina by Acharya *et al.*[77] showed microplastic deformations in alumina subjected to high strain rate compression, but they also found that cracks were mostly caused by intergranular cracking, glassy phase cracking, and the growth of dislocations. This lends further weight to the idea that defects such as pores and intergranular material are more important to failure than defects such as intergranular boundaries or grain size effects.

Comparing the effects of microstructure on strength and crack speed measurements shows noted differences between AD-85 and AD-995. Namely, a strength of 2.0 ± 0.1 GPa was measured for AD-85 and 2.4 ± 0.2 GPa for AD-995 at 10^{-3} s^{-1}, and 2.6 ± 0.3 GPa for AD-85 and 3.6 ± 0.5 GPa for AD-995 with strain rates between 10^{2} and 10^{3} s^{-1}. In compression Kolsky bar experiments, the crack speeds were 1800 ± 600 m/s for AD-85 and 2200 ± 400 m/s for AD-995. Under impact conditions crack speeds of 3000±1800 m/s for AD-85 and 4800±3000 m/s for AD-995 were observed. The higher average crack speed and narrower deviation is attributed to AD-995 being both a stiffer material and having a more homogenous microstructure. By having a higher stiffness than AD-85, the speed of sound within AD-995 is higher and thus the limit on crack growth is higher as the limiting factor is usually taken to be at the absolute most 50% of the Rayleigh wave speed, with 25% being more typical[79,80]. The smaller grains, more pores, more inclusionary defects, and amorphous phases providing a more varied path for cracks to grow cause the higher variability in speed for AD-85. Defects in AD-85 are larger and more varied in chemical nature than AD-995, further contributing to this greater variability in crack speed. In comparison to compression experiments, under impact loading conditions the crack speeds for AD-85 and AD-995 are much closer to each other. This is likely attributable to the fact that when impact loading, both AD-85 and AD-995 feature mostly continuous crack growth behavior and are subjected to a more complex stress state that includes significant contributions from tension and shear. The higher crack speeds under impact can be attributed to the higher input energy, as seen by Strassburger *et al.*[39] in their edge-on-impact experiments.

When comparing the PDV traces between AD-995 and AD-85, the largest point of comparison between the two is that AD-995 has a much higher acceleration and deceleration than AD-85, and reaches a lower peak velocity. Given that AD-995 defeated the projectile while AD-85 did not, this suggests that these back face velocity curves are indicative of how these behaviors occur. They also show that the most significant part of the PDV curve can occur within the first five microseconds, an important consideration for when designing materials that are more resistant to impact. It is possible that the higher stiffness of AD-995 allows it to respond more quickly to the impact event, hence its faster rise time, while the greater strength and stiffness means that the energy of impact is more effectively dissipated, hence the lower peak velocity and successful stopping of the projectile. Further testing is required to confirm this hypothesis across a range of materials and impact velocities.

2.4.2. Event Correlation in Impact

By linking video and X-ray images to the PDV traces, we attempt to correlate events seen in different sets of measurements with each other. This is done so that we can understand the sequences of events and thereby learn more about the process of dynamic failure, such as whether peak strain occurs before or after the onset of radial cracking. Analysis of the timing of events requires knowledge of the speed of sound in the material, with the two fastest being the longitudinal c_p (also called compression or primary) and transverse (also called shear or secondary) waves. The density, elastic modulus, and Poisson's ratio of the materials allows for the calculation of these speeds using Equations 2-1 and 2-2.

$$c_p = \sqrt{\frac{E(1-\nu)}{(1-\nu)(1-2\nu)}} \approx \sqrt{\frac{E}{\rho}} \text{ for } \nu > 0.3 \qquad [2\text{-}1]$$

$$c_s = \sqrt{\frac{E}{3(1+\nu)\rho}} \qquad [2\text{-}2]$$

The calculated values have been included in Table 2-1 as part of the material properties of AD-85 and AD-995. For the tungsten carbide of the projectile, wave speeds are 6200 m/s for the longitudinal wave and 4000 m/s for the transverse wave, calculated from the material's mechanical properties. Using the thickness of the target and diameter of the WC projectiles of 6.4 mm allows for the time required for the wave fronts to transition the materials to be calculated by $t = \frac{d}{c}$. This allows for correlation with events seen in the PDV traces, the high-speed photographs, and the flash X-ray images. There are several necessary assumptions for this forthcoming analysis:

- Material properties remain constant – damage does not change the elastic modulus or density. This assumption fails once the material is damaged, but for the purpose of analysis it is assumed constant before the appearance of radial cracking.
- Lengths remain constant – neither the projectile nor target deforms significantly.
- Waves that reach the surface of a material will produce a reflected and transmitted wave – the energy partition between reflection and transmission depends upon the degree of mismatch between the impedance of the materials.
- A wave that has been reflected once off an interface such as WC to air or alumina to PC retains sufficient energy to produce a significant transmitted wave into the other dense material.

- Waves retain their form after a transmission or reflection – longitudinal waves remain longitudinal, transverse waves remain transverse.

Figure 2-13 shows the relationship between the back face velocity and the communication of events through the target, with the addition of lines that mark the arrival of significant wave fronts at the back face of the target to the PDV trace for AD-85. Figure 2-14 shows the same labelling of wave front arrivals for the AD-995 trace, but based upon the higher speeds of sound in AD-995. The first two wave fronts tracked are for the longitudinal and transverse waves generated by the impact that travelled through the target. For Figure 2-13, the arrival of the impact shear wave corresponds to an initial rise in back face velocity in AD-85, but as seen in Figure 2-14 this correlation is not seen in AD-995. Reverberations within the target of longitudinal and transverse waves were also considered, but were not found relevant for AD-85 as activity begins before a full reverberation could be made. For AD-995 the longitudinal and transverse wave fronts have sufficient time to make a full round trip from the back face to the front face and back again to arrive in time for significant effects. The longitudinal and transverse wave fronts arising from within the WC projectile that reflect off the back face of the projectile and then transmit into the target are termed the 'release waves'. While these release waves are somewhat ambiguously associated with the onset of radial cracking, they do appear potentially related to the largest rise in back face velocity. Other waves such as Rayleigh surface waves were also considered, but they have a path length long enough that their arrival is too late to contribute to significant activity within either the UHS videos or the PDV traces. Wave transmission from alumina to PC likely also occurred, but the speeds of sound of PMMA are less than a quarter of that of AD-85 and less than a sixth of AD-995, so wave fronts in PC are too slow to influence the alumina over the time frame of interest of the first 6 μs.

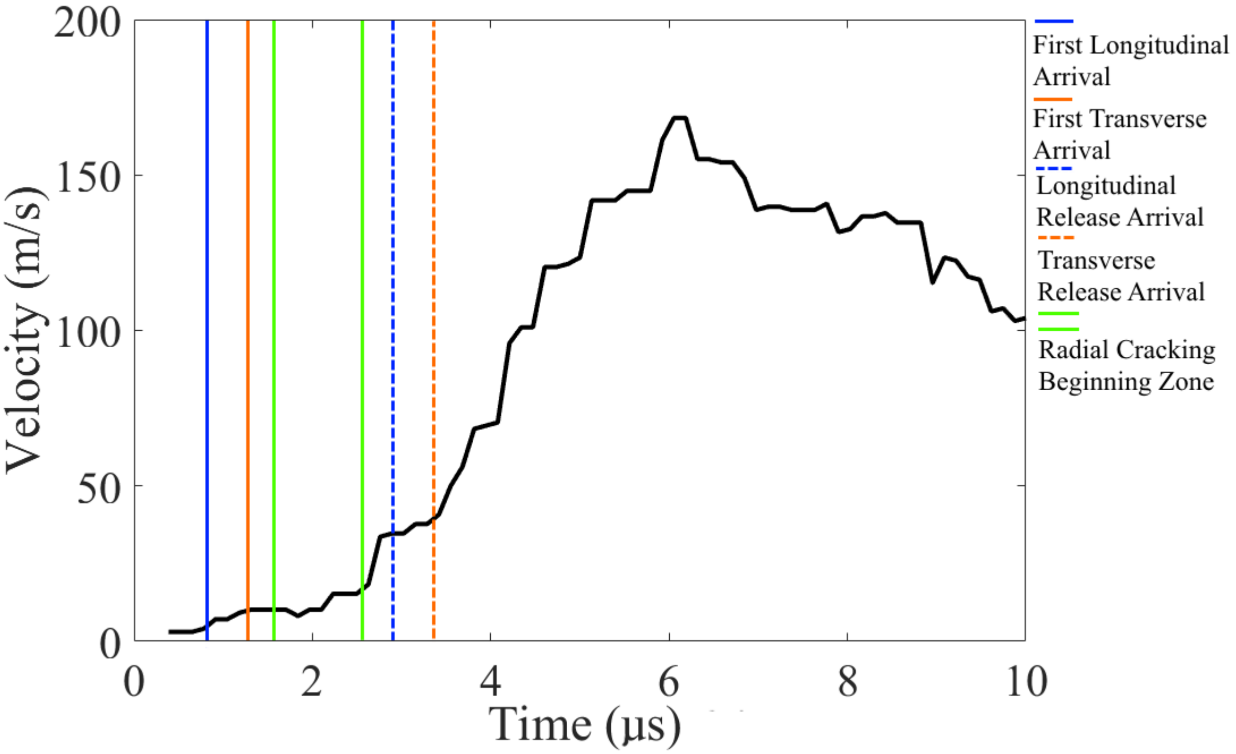

Figure 2-13 – PDV trace for AD-85 showing the arrival of the first most significant wave fronts and the period of time where radial cracking could have possibly begun. Here the first longitudinal wave appears to correlate with the first major rise in back face velocity, with the first transverse wave correlating most closely to the possible onset of radial cracking. The longitudinal and transverse release waves occur after the onset of radial cracking, but appear to potentially correspond to rises in measured velocity.

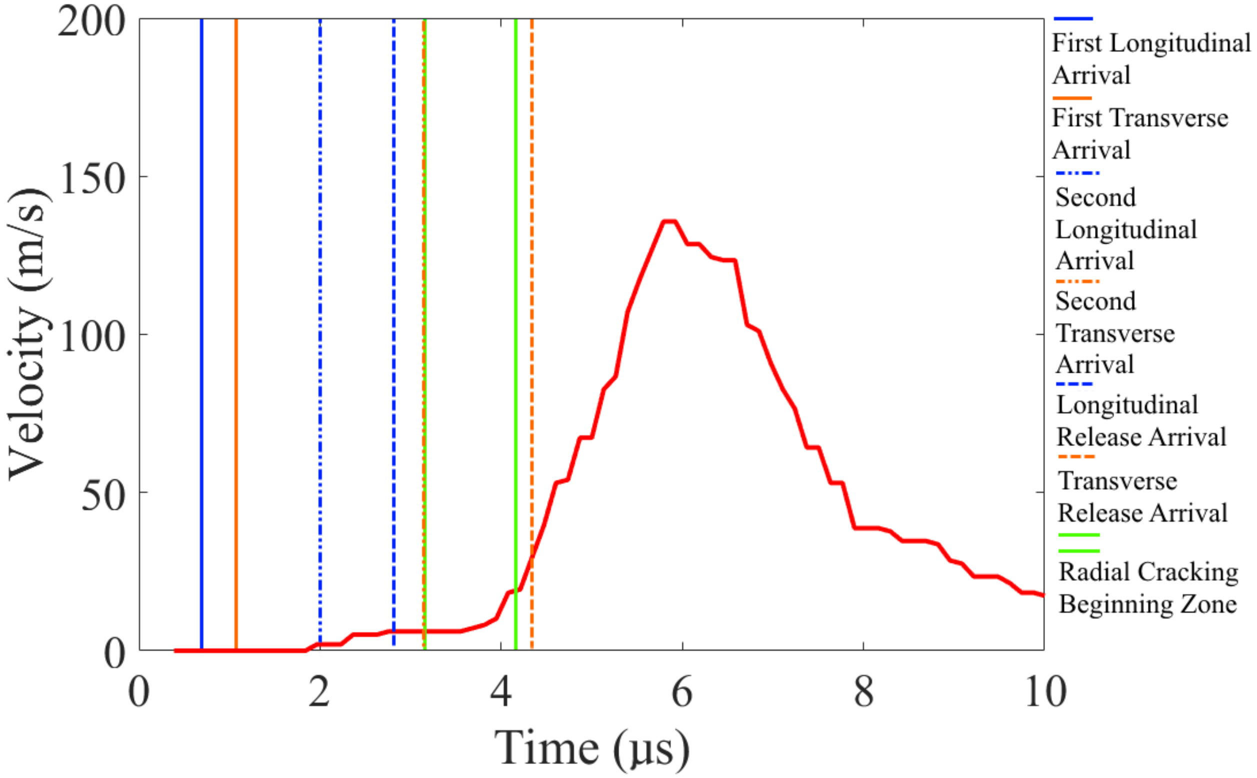

Figure 2-14 – PDV trace for AD-995 showing the arrival of the wave fronts deemed most significant and the period of time where radial cracking could have possibly begun. Here the first longitudinal and transverse waves correspond to no activity in the PDV trace, but the second longitudinal wave arrives around the first time that non-zero activity is detected, and the second transverse wave arrives at the earliest possible moment for radial cracking to begin. The longitudinal release wave front also arrives just before the earliest point of radial cracking, while the transverse release wave arrives just after cracking has definitively begun and during the rise in velocity.

For both AD-85 and AD-995 the most significant correlation is that both begin to experience their largest acceleration at approximately the same time as they begin radial cracking, and do not experience cracking from interactions with the first longitudinal wave to arrive. Given that AD-995 defeated the projectile while AD-85 was penetrated, the long delay between impact and back face activity for AD-995 suggests that AD-995 causes the WC projectile to dwell on its surface for an additional 2 µs, further highlighting the importance of a few microseconds in defeat or not defeat. Furthermore, the waves that correspond best to significant activity in the PDV traces and UHS video are shear waves, suggesting that the material may be failing in a shear mode. While for the purposes of calculation the elastic properties of the materials are kept constant since the actual changes are unknown, damage significant to cause radial cracking to become visible is likely significant enough to reduce Young's modulus and increase the apparent Poisson's ratio, both factors which decrease the shear wave velocity. Thus shear waves that are calculated to arrive slightly too soon are good candidates for being the communicator of the onset of cracking, with both AD-85 and AD-995 having these sorts of suspected wave fronts. Review of the literature lends further credence to the idea of shear waves having a greater importance for damage events.

Previously discussed in relation to microstructure studies, Acharya *et al.*[77] found that in Kolsky bar compression experiments plastic deformation mechanisms were primarily of mode II (in plane shear) and mode III (out-of-plane shear) cracking; not mode I (opening). Furthermore, Yu *et al.*[81] discuss the quantification of damage of concrete under compressive loading based upon X-ray computed tomography and found that mode II (in-plane shear) cracking better explained permanent damage than mode I cracking. These studies support the idea that compression causes damage to brittle materials more through translation to mode II and mode III shearing stress than to mode I tensile stress.

Prior work in the literature also supports the importance of shear and shear waves on the failure of ceramics in impact experiments. For example, McCauley *et al.*[82] performed experiments in transparent ceramics using the EOI technique with Strassburger and were able to visualize the expansion of stress waves within the material using both shadowgraphs and cross polarized images. In one particular experiment (McCauley *et al.* Figure 7[82] as an exemplar) when using a spherical projectile impacting a target, they imaged three distinct and well separated phenomenon: 1) a longitudinal wave front leading, 2) a shear wave front behind the longitudinal wave front, and 3) the damage front behind the shear wave front. This suggests that the shear state is more important to the accumulation of damage to a brittle material than the compressive-tensile state of the longitudinal waves. Other EOI experiments in that study that used cylindrical projectiles also demonstrated this separation of event fronts, but the distinction between event fronts was less visually clear as with spherical projectiles due to the shape of the impactor. Similar separation of longitudinal, shear, and damage fronts has been seen in the impact of basalt by Ramesh *et al.*[2], with the added information that damage begins to accumulate in brittle material in their configuration before the arrival of unloading waves from reflected surfaces. The variation in shear wave profile with projectile shape is of interest due to the findings of Wilkins [5] with ceramics and Børvik *et al.*[83] in steel, which had blunt projectiles more likely to penetrate targets at lower velocities than sharp tipped projectiles. Børvik *et al.*[83] had the additional contribution that while blunt projectiles were more likely to penetrate ceramics at lower velocities, sharp tipped projectiles retained more energy after penetration at higher velocities. This information in the literature and experiment together suggests that blunt projectiles are superior at damaging materials by the generation of shear waves. At lower speeds this means that a blunt projectile can make the minimum traversal to penetrate the target by having a path through damaged material, but at higher speeds this means that more energy is spent damaging the ceramic than damaging what is behind the ceramic [83].

The importance of shear on failure was also found by Holland *et al.*[84] and Gamble *et al.*[85]. Their work found that when designing composite ceramic and metal armor systems, moving metal from the back face of the target to the front face impaired performance, due to the metal layer failing in shear and transferring that shear into the ceramic, which is less capable of resisting shear. Related to this phenomenon is a study by Behner *et al.*[86] on the penetration of silicon carbide targets by long rod penetrators where copper discs were added in front of the targets and improved the efficiency of the ceramics at resisting penetration. Behner *et al.* suggest that the copper provides a buffer that attenuates shock, which can be brought into alignment with our findings by considering that copper is a soft metal. In comparison to the steel used in the works of Holland *et al.*[84] and Gamble *et al.*[85], copper likely slows down and reduces the magnitude of an impact but cannot couple shear waves into the ceramic as effectively. Additionally, boron carbide is known from past work in the literature to undergo amorphization when shear loaded[87–92], adding additional importance to the consideration of the shear waves in future work. With our experimental observations combined with prior insights in the literature, this suggests that for the design of multi-component armor systems, the introduction of sections of shear decoupling layers may prove an important addition to the systems.

2.4.3. Insights in Prior Ballistic Testing Work

The various interactions noted previously also help demonstrate how experimental set up can influence results in not immediately obvious ways. A literature review of the development of armor ceramics by Walley[93] discusses that the literature remains divided on determining which experiments are the most useful for studying high strain rate loading of ceramics. Early work on ceramic and ceramic-metal layered armor by Wilkins [5–7] used ballistic limit (V_{BL}, more frequently called V_{50} in modern literature), the velocity at which a given projectile penetrated the system 50% of the time, as a measure of a material's performance as armor. While this produced considerable insight into how ceramics fail, the methods involve large numbers of tests, and V_{50} is a measure of the overall system being used, not any individual components. The so-called "shatter gap" phenomenon emerges from the use of V_{50} as a measure of performance. It is possible for certain ceramics to undergo changes in behavior at higher impact velocities that can cause penetration less than 50% of the time before further rise increases in impact velocity brings the penetration probabilities above 50% again, thus creating two V_{50} values[94]. While the dynamics that cause projectile fracture at higher velocities are interesting on their own, the ability to generate two different V_{50} values demonstrates the issues with the technique. Bless *et al.*[95] proposed the use of the depth of penetration (DOP) method, whereby a ceramic sample is placed in front of a block of metal. The metal is sufficiently thick to stop completely a given projectile type, creating a baseline depth of penetration value that can then be compared to the depth the same type of projectile reaches when, for example, there is a layer of ceramic in front of the metal. The purpose of DOP experiments is to produce a measure of the ballistic efficiency that was unaffected by how the system was constructed, and thus a material property. From DOP experiments, Rozenberg and Yeshurun[96] found that ballistic efficiency increased monotonically with what they called the "normalized effective strength", which is the arithmetic average of quasi-static and dynamic strength measurements. While DOP experiments are a more efficient method of screening materials than manufacturing a number of body armor panels and shooting them, the method has the back face of the ceramic confined. With the results of our study suggesting that what is on the front face of the target, including the projectile itself, influences the failure of a ceramic, this brings new considerations to modelling and design. Rozenberg and Yeshurun[96] found that the ceramic tiles had to have a thickness of at least half of the projectile diameter to produce consistent results. In light of the impact experiments and PDV traces, this suggests that if the ceramic is too thin the event of the impact cannot be fully communicated within the projectile before the ceramic fails, revealing different failure mechanisms than typically seen under these conditions. For the purposes of modelling, the information on the sequence of events during defeat and failure can better help validate models and simulations. The experimental knowledge that key events are over within the first five microseconds can also be of great value to modelers by allowing for a narrowing of the temporal windows of simulations, saving processing time so that only the most significant events require modelling.

2.5. Concluding Remarks

This study has examined the microstructure of two grades of alumina and their behavior when subjected to impact loading. Scanning electron microscopy, electron backscatter diffraction, and energy dispersive X-ray spectroscopy were used to assess the microstructural properties, giving detailed information on grain sizes, chemical compositions of grains and defects, and defect sizes and spacing. Lower purity AD-85 alumina had smaller alumina grains than higher purity AD-995, but these grains were mixed in with amorphous silica and large pores, producing a weaker material that was less able to resist impact from a project. In Kolsky bar experiments, AD-85 showed an increase in strength in comparison to quasi-static conditions, but still demonstrated lower failure strength and stiffness than AD-995. In impact experiments, high-speed photography, flash X-ray photography, and photo-Doppler velocimetry were used to examine the behavior of alumina tiles with sub-microsecond temporal resolution. At a velocity where AD-85 was penetrated by a projectile but AD-995 defeated the projectile, the PDV traces show important differences that point towards phenomena important to the behavior of a ceramic occurring within the first five microseconds of impact. Beyond that, by tracking when wave fronts generated by the impact should arrive at the back face of the target and correlating to events seen in the PDV traces and high-speed videos, this study shows that the behavior of the projectile in generating shear influences failure events such as radial cracking. The importance of shear in materials in contact with the front of a ceramic upon the failure of the ceramic has been seen elsewhere in the literature, and with this new experimental information modelers of important periods and characteristics to consider. For the design of armor systems, these experiments show new insights into ways to maximize the efficacy of ceramics for the stopping of projectiles. This work also motivates further work exploring the PDV traces of different ceramics at different velocities to find further points of commonality between them.

Chapter 3 - Two-Dimensional Dynamic Damage Accumulation in Engineered Brittle Materials

3.1. Introduction

The defining characteristic of brittle materials is that they undergo little to no plastic deformation before failure, but instead undergo crack formation and growth. A popular method of modelling crack growth is the wing-crack model[38,46–48,56,55,97,98], which is based upon studies of crack growth in brittle transparent materials such as glass[45]. The core formulation of the wing-crack model was first posed by Nemat-Nasser, Horii, and Obata in the 1980s[46–48,56] whereby the various mechanisms of macroscopic crack growth[45,99] are combined together into a single formulation that can be iterated to produce predictions of the stress-strain behavior of brittle materials undergoing fracture[36,49,50,100]. Further expansions to this formulation have been made to introduce factors such as crack interaction[101].

The specific theory of wing-cracks begins with a crack of arbitrary orientation to the direction of loading. When a stress is applied, the crack will begin to grow along the same axis as the applied stress[45]. Initial flaws have random orientations with respect to the loading direction, but the wing-crack phenomenon causes curvilinear crack that becomes linear parallel to the direction of loading. The cracks grow parallel to the loading direction because stress concentrations will cause compressive loading to be resolved as tensile loading at the crack tip. This stress state produces a Mode I tensile opening failure that results in both the length of the wings increasing and a separation between the faces of the wings[45,47,99]. The crack can also grow by the faces of the central crack sliding apart, which results in the volume occupied by the crack increasing. From examining the mechanisms in this manner, it is seen that sliding and opening mechanisms alter the relationship between linear deformation and volume as crack opening will result in an increase in the total volume of the material.

All three of these modes are captured in the original model by Nemat-Nasser and Obata[56]. Their model assumes that the influence of the wing-cracks acts in superposition to standard linear elasticity. The formula thus produces linear elasticity in the absence of the wing-cracks with the strain vector $\boldsymbol{\epsilon}$ being the product of the compliance tensor $\boldsymbol{S}$ and the stress vector $\boldsymbol{\sigma}$. The model then assumes a distribution of N number of cracks at angle θ of initial starting length $2c$, grouped together as $f = c^2N$. Next introduced are coefficients for the slip between crack faces, b, crack face opening, d, and wing-crack length, l. For the crack extension mechanism, the individual elastic constants of Poisson's ratio ν and the shear modulus μ are required. Finally, the model accounts for the angle the crack is to the applied stress through the directional tensors $\boldsymbol{p}_0$, $\boldsymbol{p}_1$, $\boldsymbol{q}_0$, $\boldsymbol{q}_1$, $\boldsymbol{\alpha}$, and $\boldsymbol{\beta}$, which are all related to the crack-to-load angle Φ and wing-crack-to-main-crack angle θ. Figure 3-1 illustrates the geometry of these variables in order to show how their influences interact with each other and overall crack volume. All of these factors are combined in Equation (3-1) to describe a stress-strain relationship for a brittle material with wing-cracks.

$$\boldsymbol{\epsilon} = \boldsymbol{S}:\boldsymbol{\sigma} + 2fb\boldsymbol{p}_0 + 2fd\boldsymbol{p}_1 + 2bl\boldsymbol{q}_0 + fdl\boldsymbol{q}_1 + f\frac{1-\nu}{8\mu}\pi l^2[(4\boldsymbol{\sigma}:\boldsymbol{\alpha})\boldsymbol{\alpha} + (\boldsymbol{\sigma}:\boldsymbol{\beta})\boldsymbol{\beta}] \qquad (3\text{-}1)$$

This formulation is an iterative model, as strains will cause the values for b, d, and especially l to change through stress-concentrations that alter the microscopic stress experienced by the cracks. Further complexity in the model formulation is achievable via such additions as allowing the cracks to interact with each other [55] or expanding from a two-dimensional to three-dimensional formulation [36]. The overall formulation can be seen as an addition to standard elasticity, and a popular modelling method [36,52,55] is to introduce a damage term that encapsulates the additional strains as a decrease in elasticity. This method allows for physical damage caused by the formation, extension, and coalescence of cracks to be manifested as a change in mechanical response. In order to differentiate between physical cracking and the changes in elastic response the terms 'physical damage' and 'mechanical damage' will be used. A typical formulation of the mechanical damage term is $E_{eff} = (1 - D)E$ where E_{eff} is the effective Young's modulus, D is the damage to the material, and E is the undamaged Young's modulus. The bounds of D are usually given as being between 0 and 1, with 0 being the pristine state and 1 being a total loss of resistance to deformation in this formulation. Expansions upon this formulation will typically involve ideas such as the introduction of anisotropic damage [36,97] or allowing for $D = 1$ to correspond to the compressive strength of the material as a powder to allow for some residual strength of a 'completely damaged' material, such as in the work of Clayton and Tonge[51]. From this point on we shall refer to the effective Young's modulus as the 'stiffness' as the damage acts upon the entire stiffness tensor, as it is frequently used in studying anisotropic materials in literature[51], but is assumed to act most significantly upon the stress-strain response.

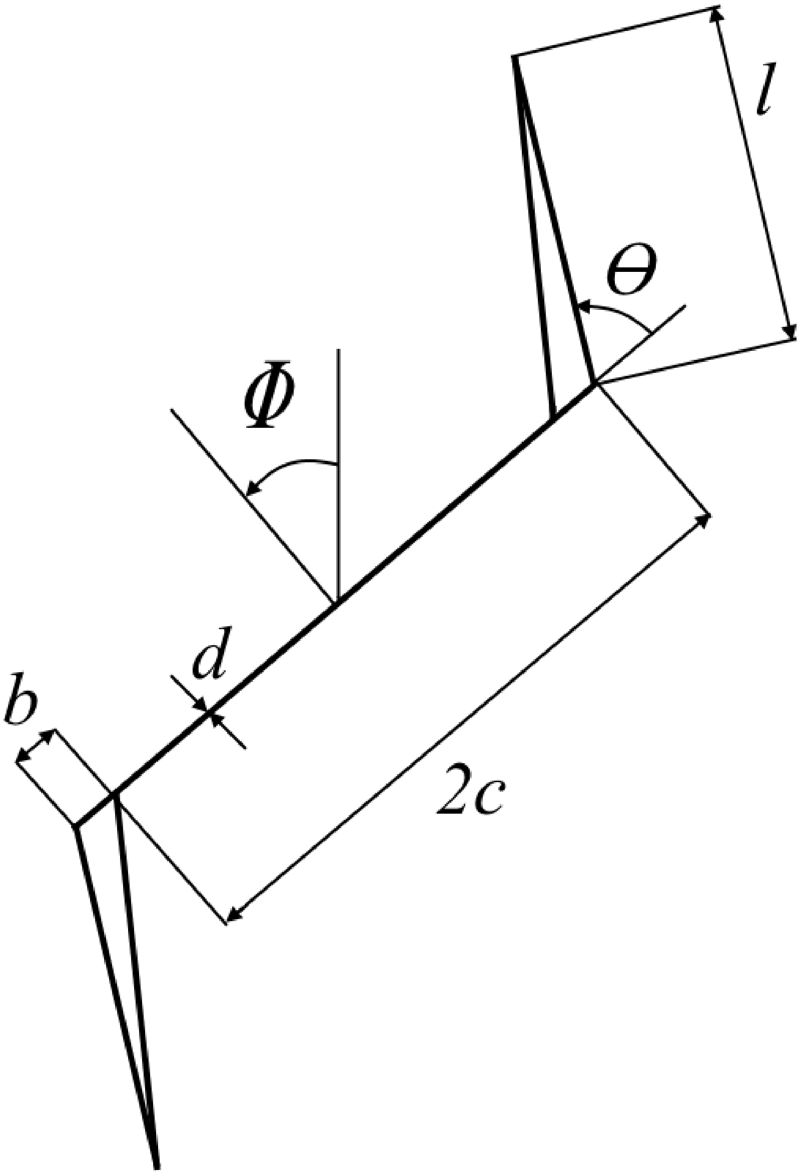

Figure 3-1 – Wing-crack showing the various dimensions such as the primary crack length (*2c*), wing-crack length (*l)*, wing-crack opening (*b*), crack face opening (*d*), angle of main crack from direction of compression (*Φ*), and angle of wing crack to main body (*Θ*).

A core question for these types of modelling methods is what appropriate values of f, b, d, l, and μ should be used to model the behavior of materials so that they are in agreement with both observed physical characteristics and mechanical response. Technologies such as X-ray computed tomography (CT) can allow for the actual microstructure of real materials to be probed[102], but the observed behavior varies from the model predictions produced when using physical microstructure properties[103]. The complexity of the idealized wing-crack model means that not all of the inelastic mechanism (sliding, crack opening, and crack elongation) will have the same contribution to the loss of elasticity, and the differences in contribution likely vary with the degree of strain[98], strain rate[38], and stress state[104]. An example of this variation is the crack sliding mechanism, which is based on the coefficient of friction of the material with itself[56]. If the microscopic coefficient is different than the macroscopic coefficient, or if at a certain strain rate the material transitioned from a static to a dynamic coefficient of friction, then this would be implicitly a variable weighting on the relative contribution of crack sliding. As a consequence it is thus sometimes necessary for modellers to select input parameters not based upon the macroscopic properties of the material but on what produces the best fit between model output and experimental results, discovering the relative weighting[56]. Being able to derive the relationship of the material properties and crack characteristics that feed into Equation (1) and other models like it from the observed physical properties of a material and the actual macroscopic behavior under a variety of loading conditions is critically important to efficient modelling and design of ceramics based systems. This paper seeks investigate what behaviors observably manifest when physical damage accumulates sufficiently to cause deviation from linear elastic behavior in advanced ceramics.

The formulation developed by Nemat-Nasser and Obata[56] shows where an experimentalist should look in order to learn more about internal crack evolution. These are the inelastic factors involving volume-changing mechanisms. In order for a crack to slip or dilate the material must occupy more volume than it did initially, requiring a change in apparent Poisson's ratio. Experiments with brittle materials such as coal[1] and concrete[102] have shown that a material can be compressed and show a decrease in Young's modulus but an increase in Poisson's ratio, which implies the formation of volume-increasing cracks. These studies did not examine advanced ceramics and involved quasi-static compression, but they provide grounding for possible mechanical manifestations of permanent fracture phenomena in brittle materials. The X-ray imaging done by Poinard *et al.*[102] is especially relevant as part of their work allows for an examination of what sorts of physical phenomena are possible in brittle materials. These effects include pore collapse and crack opening without manifesting as a decrease in apparent Young's modulus. By incorporating these effects into prior damage models [49,51,105] the net effect of multiple mechanisms with complex interactions can be better understood. This understanding can then be applied to more complex stress-states such as ballistic impacts where two-dimensional compression and shear are involved[106]. The process of better understanding the complexities discussed above begins by performing simple uniaxial experiments that produce stress, axial strain, and lateral strain data. These three factors allow for stiffness and Poisson's ratio to be tracked with strain and time, allowing for the development of a framework that can incorporate damage to both stiffness and Poisson's ratio. This work is thus motivated by having access to experimental data that has been previously unavailable that shows a greater degree of complexity for brittle material failure than previously expected in modelling[36,49,52,55,105]. This new experimental data prompts the establishment of a methodology for capturing these new details. Using the experimental set up detailed in Lo *et al.*[60] and Li *et al.*[107], new data on stress and two-dimensional strain is generated for a variety of engineered brittle materials and is then put into the context of prior theory. Unexpected and even counter-intuitive behavior is observed, indicating a need for a model of damage that incorporates changes in apparent Young's modulus and Poisson's ratio. This model thus offers explanation of experiments, new insight into the fracture and failure behavior of engineered brittle materials, and theoretical motivation for future experiments that would not have been previously considered.

3.2. Experiments & Results

3.2.1. Experimental Set Up

Compression testing is used to probe material behaviors in this study. To perform compression tests, the samples were machined into cuboids of dimensions of 3.5 mm x 2.7 mm x 2.5 mm for use in quasi-static and dynamic testing. These sizes were chosen to conform with prior samples[108], but reduced in dimensions in order to produce higher pressures with less force used, particularly in Kolsky bar experiments. Cuboidal specimens are commonly used in the testing of advanced ceramics due to ease of machining and polishing, and for the purposes of this study provide flat surfaces that can be used for measuring both axial and lateral strains using Digital Image Correlation (DIC). Both axial and lateral strains are important in this study as the evolution of Poisson's ratio (the ratio of lateral and axial strains) during loading and failure is of primary interest for exploring damage accumulation to elastic properties. Because 2D-DIC is not applicable to capturing out of plane strains, curved specimens would not produce viable lateral strain measurements. In these studies, the quasi-static compressive strength and Young's modulus were independently examined using an MTS 810 materials testing machine that compressed samples to failure. The servo-hydraulic controls allowed for precise measurement of forces, and DIC was used to determine axial and lateral strains. The DIC setup is discussed in a subsequent paragraph. Promon U750 cameras recording at 100 Hz were used to capture the entirety of a 30 to 50-second-long quasi-static experiment. While the framerate was sufficient to capture stiffness and Poisson's ratio information, 100 Hz is insufficient to capture the behavior of samples during actual failure (i.e., post-peak stress), as the events occur too quickly. Triggering a higher speed camera that is capable of operating at half a million frames per second or higher in the quasi-static experiments based on failure events requires additional equipment not available at the time of publication. Thus quasi-static testing was only used to confirm the validity of a combined strain gauge and DIC approach, and to confirm that the elastic constants were as described by the manufacturer, when available. The experiments of primary interest in this work come from the Kolsky bar experiments where post-peak behaviors are captured using an ultra-high-speed camera.

The materials that were used were two grades of alumina, AD85 and AD995 from CoorsTek, Inc., silicon carbide (SiC) from Milburn Mountain Defence (Quesnel, British Columbia, Canada), and TitanMade® cermet from Lumiant Corporation. AD85 is 85% purity alumina and AD995 is 99.5% purity alumina, with further details on their characteristics in Koch *et al.* [109]. TitanMade® is a brittle cermet with a metal matrix of (γ-α_2)-two-phase titanium-aluminide and 70% nano-grained aluminum oxide ceramic phase, characterized by Li *et al.* [110] and modelled by Amiran *et al.*[111]. AD85 and AD995 have publicly available elastic properties from the manufacturer[112], while the cermet's mechanical properties were determined by Li *et al.*[110]. Quasi-static testing of the silicon carbide demonstrated elastic properties to be within the ranges found in the literature[113]. This information can be found in Table 3-1 alongside experimentally determined quasi-static and dynamic values. The alumina and silicon carbide were selected as representative advanced ceramics used in armor systems and industrial applications, while the cermet was selected for being a brittle material with a different overall microstructure that would allow for the possibility of different failure modes to be defined, especially with the new damage model explored in this paper. The microstructure of the alumina was studied by Koch *et al.*[109], the microstructure and mechanical properties of the cermet was studied by Li *et al.*[110] and

Amiran *et al.*[111], and the microstructure of the silicon carbide was not disclosed by Milburn Mountain Defense. Where those prior papers sought to understand the influence of microstructure on the behavior of these materials, this paper seeks to combine ultra-high-speed photography, digital image correlation, and high-speed strain measurements to produce high strain-rate two-dimensional stress-strain relationships never before seen in advanced ceramics.

Table 3-1 – Elastic properties of materials tested with quasi-static (QS) and dynamic stress conditions. Note that TitanMade cermet has continual damage accumulation and thus its listed stiffness and Poisson's ratio are the most stable values at the start of a test. Listed properties are provided where available from the manufacturer or literature. Where properties are unknown or exist in a range, a * is used to indicate as such.

Material	Listed Strength (GPa)	Listed E (GPa)	Listed ν	QS Peak Stress (GPa)	QS E (GPa)	QS ν	Dynamic Peak Stress (GPa)	Dynamic E (GPa)	Dynamic ν
AD-85[112]	1.93	221	0.22	2.2±0.2	220±20	0.22±0.03	3.1±0.2	250±30	0.23±0.02
AD-995[112]	2.60	370	0.22	2.4±0.2	370±30	0.22±0.01	3.5±0.7	410±30	0.29±0.08
Silicon carbide[113]	3.0-4.0*	370-410*	0.15-0.22*	3.3±0.1	360±50	0.18±0.01	4.9±0.5	440±50	0.17±0.04
TitanMade® [110]	*	280	*	2.78±0.06	270±30	0.23±0.01	3.1±0.3	260±10	0.29±0.06

Dynamic testing was done using a custom-built Kolsky bar testing apparatus coupled to an ultra-high-speed Shimadzu HPV-X2 camera capable of capturing at ten million frames per second and 400 x 250 pixel resolution. For the experiments performed here, a framerate of 500 kHz was used at full resolution and the camera system was coupled with a K2 Infinity Lens to fill the sample in the 4 mm x 6.4 mm field of view of the camera. The field of view offered by these optics and the resolution of the HPV-X2 at 500 kHz currently represent the edge of technological limits and the state of the art for brittle material fracture studies. The Kolsky bar apparatus used incident and transmitted bars that were 12.7 mm in diameter and made of maraging steel (Service Steel America C-350) with a Young's modulus of 200 GPa, Poisson ratio of 0.29, yield strength of 2.68 GPa, and a density of 8100 kg/m^3. The incident bar was 101.6 cm in length, while the transmitted bar was 91.44 cm in length. A projectile made from maraging steel was launched using compressed gas to strike an incident bar, which then transmitted the strain pulse into a ceramic sample, with another bar receiving the remaining stress pulse from the event. The steel bars were protected from damage by the harder ceramic samples via 5 mm thick and 7.938 mm diameter tungsten carbide platens jacketed in 12.7 mm outer diameter titanium rings. These dimensions and materials are similar to those used with other advanced ceramic Kolsky bars, as detailed by Swab and Quinn[114]. The platen-sample interfaces were lubricated with high pressure grease in order to reduce the transmission of lateral or shear strains from the bars into the samples and to ensure that the input pulse was as uniaxial as possible, as is considered good practice in the literature[115,116]. A near-triangular pulse is considered ideal[61,71], and this shape was achieved by using a 3.175 mm diameter and 1 mm thick tin pulse shaper, with a final strain rate on the order of 10^1 to 10^2 s^{-1} occurring over a period of 200 μs. These pulse durations are much longer than typically used in the literature of 50 to 100 μs rise times[61,71], but have allowed us to achieve good stress equilibrium[117] and measurements for the purpose of our current study. Strain was measured by six strain gauges arranged in three pairs, with two pairs on the incident bar, and one pair on the transmitted bar. Each pair had an additional two gauges not connected to the bars but connected together to form a full wheatstone bridge, with each bridge connected to its own Vishay 2310b amplifier, which sent their signals to an HBM Gen3i high speed portable data acquisition system. The strain gauges were Micro-Measurements CEA-06-250UN-350 350 ohm resistance gauges secured in place via cyanoacrylate adhesive. These gauges are examined for accuracy and precision before testing, and replaced and recalibrated by an expert technician as needed. Tests were only considered successful when strain responses and camera images confirmed that samples failed in loading on the first loading pulse through the material. This setup has been used previously in Koch *et al.* [109] and Lo *et al.* [60] and was used in a round robin test of Kolsky bars coordinated by Swab and Quinn[114], where the setup is comparable to other labs and produced the same results as leading government and academic laboratories. At the time of publication, this system can be considered state of the art and reliable for dynamic brittle material testing.

Digital image correlation techniques were applied to ultra-high-speed camera images captured in order to obtain lateral and axial strain measurements of the samples. DIC is a computer vision method used to track changes in the position of speckle patterns on the surface of an object in order to compute deformation fields, and has been well established in the study of many different materials[118–122]. Due to the high speed of image capture and low exposure times, a high gloss metallic paint for the speckles and high intensity LED ring light (REL Inc.) were required in this study to produce sufficient contrast in the images. Due to the small size of the samples in our study, special measures were required to produce a speckle pattern that would work correctly. In this study, an airbrush with a 0.15 mm nozzle was used and this produced speckles between 5-10 pixels, which corresponds to speckle areas of approximately 1300 to 2600 μm^2. A representative test sample with applied speckle patterns seen in Figure 3-2, demonstrating good imaging at 200 ns exposure times. DIC analysis was done using the commercial VIC-2D (v6 2018) software from Correlated Solutions (Irmo, South Carolina, USA), with the regions of interest discretized into 27 by 27 pixel subsets with a virtual strain gauge set with a filter size of 15 and a step size of 7 pixels. The zone of interest used for DIC was typically the entire sample excluding edges, but comparison with various subset zones has shown that the strain values are convergent [60], indicating uniform deformation in the sample. A sample image showing a typical zone of interest and comparing the response of sub-sections can be seen in Figure 3-3 as part of a larger discussion on equilibrium behavior in the tests. Figure 3-3 shows a stress-time plot taken from the strain gauges and multiple strain-time plots taken from DIC. Each strain-time plot corresponds to a different subsection area-of-interest, with the Average Strain line corresponding to the strain of the entire area-of-interest. The image of the ceramic seen on the right-hand side of Figure 3-3 shows the spatial distribution of these subsections. The subsections shown in Figure 3-3 are not computational elements of the overall area-of-interest, but represent independent DIC processing. This is done in order to check strain equilibrium across the entire surface by looking for local variation. In Figure 3-3 the individual strain curves for each subsection overlap each other and the Average Strain line up to failure, which demonstrates that the entire sample is in equilibrium up to failure. The stress and strain curves following each other up to peak stress shows that the behavior of the material is linear elastic up to failure, as expected of a brittle material. The correlation shape function is internal to the software, based on derivatives of displacements, with the correlation criterion used being ZNSSD. Images were pre-filtered using the VIC-2D default smoothing of a low-pass filter to remove background noise. Subset weighting was done via a 90% center-weighted Gaussian filter with a window size of 15 data points. No additional post-processing smoothing was performed. Correlation analysis was carried out using the zero-normalized sum of squared differences correlation criterion and the optimized 8-tap interpolation scheme. Confidence intervals for correlations were consistently within the range of 10^{-3} to 10^{-4} pixels. Measurement uncertainty from measurement equipment is taken to be no greater than a conservatively large 5% in total, with the largest possible source of uncertainty being the initial size of the samples in the visual field, taken as being 0.1 mm out of the 2.7 mm side length of the 2.7 mm by 3.5 mm face used for measurement, which amounts to

>4% uncertainty. An elastic test using no sample between the bars showed that the magnitude and transient response of the strains recorded from DIC and the strains recorded from the strain gauges were in reasonable agreement with each other, and mismatch would not contribute to uncertainty. Strains were computed from the displacement fields using the engineering strain tensor. The computed strain histories were matched to the stress histories produced by strain gauges on the Kolsky bar to determine stress-strain curves for each of the experiments, as is commonly done in Kolsky bar experiments in the literature[117]. This produces stress-strain plots that do not need to assume material properties. By not assuming material properties, stress-strain and lateral-axial responses are allowed to vary as functions of time. Furthermore, because DIC allows for the tracking of strains, the Kolsky bar can be used solely for tracking stress, with only the transmitted strains and the elastic response of the steel being required, with no need to use wave equations. DIC has been used previously in Kolsky experiments by the authors [110], with the full validity of the process being explored in greater detail by Lo *et al.*[60] in terms of near-constant strain rate and good stress equilibrium. This was assessed by observing uniform strain accumulation across the sample and near-synchronization of the strain-time and stress-time curves. This can be seen in Figure 3-3, which shows an example of the same analysis as done by Lo *et al.*[60] but using data from this work. In Figure 3-3 the strain vs. time profiles generated from DIC analysis for sample SiC-1 using different areas of interest are plotted together to show that the averaged strain across the sample face is not strongly affected by local variation. The stress vs. time is also plotted alongside the strains to show that the material response is in equilibrium up until failure (i.e., stress-time and strain-time curves track each other). The stress-time response is taken from the transmitted side of the Kolsky bar and shows a smooth stress-rate up to failure. With the stress-time and strain-time curves in agreement with each other before linear elastic behavior is lost, the strain-rate is taken from the slope of the DIC average strain curve before deviation from linear.

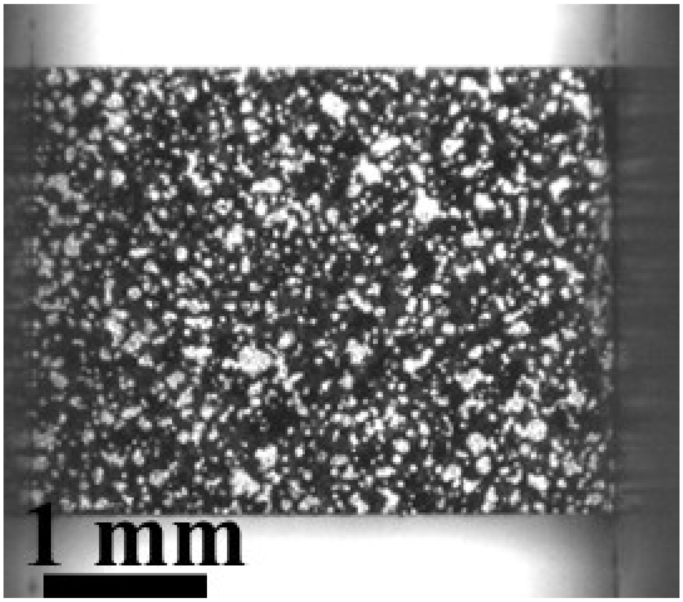

Figure 3-2 – A 3.5 mm x 2.7 mm x 2.5 mm sample of AD85 alumina with speckle pattern applied for DIC purposes. The micron-sized speckles are produced using an airbrush with a 0.15 mm nozzle, which gives a randomized pattern with sufficient resolution to work with DIC. This sample is loaded between the incident and transmission bars of a Kolsky bar apparatus, with compressive loading delivered horizontally along the long axis of the specimen.

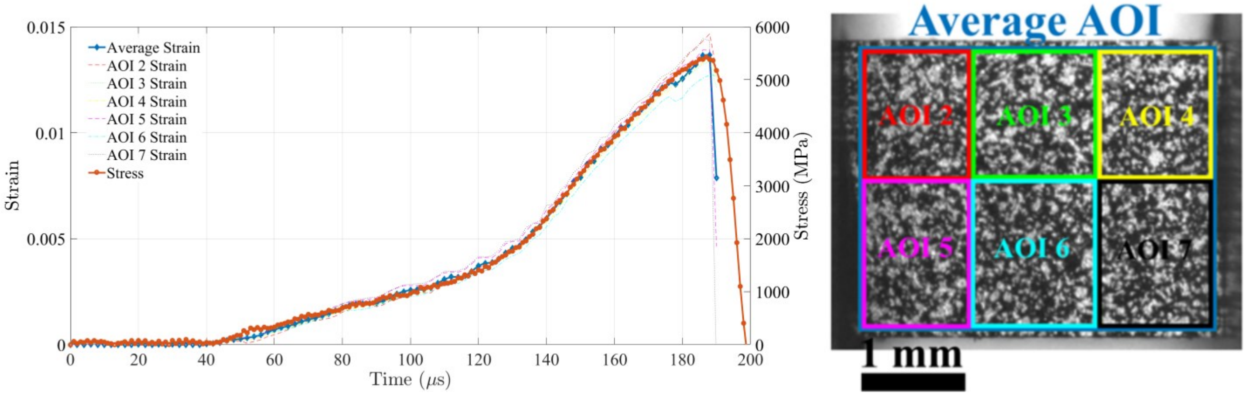

Figure 3-3 – Plot of strain versus time and stress versus time taken from the total area of interest for the SiC-1 sample, with the subsection areas of interest illustrated on the right. The global strain as determined by DIC is thus shown to match up with the localized strains. The stress as determined from the transmitted Kolsky bar measurements is also shown to follow the DIC strains, showing how the two measurement methods are in accordance with each other. The stress curve also represents an input load up to the point of failure, showing a constant stress-rate, and thus up to failure a constant strain-rate.

3.3. Experimental Results

A summary of the linear elastic properties measured in the quasi-static and dynamic tests for the materials studied in this paper is found in Table 3-1, and will be discussed throughout the following paragraphs. These values incorporate data from multiple quasi-static and dynamic tests, with stiffness and Poisson's ratio values taken from linear sections of stress-strain relationships and lateral vs. axial strain relationships, respectively. Peak strength was taken as the highest stress reached, and strain at failure was when peak stress was reached by the sample. The materials exhibited a 40±10% increase in failure strength under dynamic conditions in comparison to quasi-static conditions, which is in line with the expectations of past literature for these strain rates[52,123]. Stiffness and Poisson's ratio showed less sensitivity to strain rate than failure strength, with the quasi-static and dynamic values being statistically equal. In comparison to historical results, the elastic properties found here for alumina are in agreement in terms of Young's modulus, Poisson's ratio, and failure strength in dynamic compression[124–126].

For the Kolsky bar tests, three stress-strain results for all four materials can be seen in Figure 3-4. To filter out noise, a Savitsky-Golay filter of order 3 over across a frame length of 15 points has been applied to the data presented in Figure 3-4, and later in Figure 3-5 for the lateral vs. axial data. This filtering smooths out the curves of fluctuations while retaining actual changes in the stress-strain and lateral vs. axial behaviors. The tests presented within this paper are considered representative of general behaviors for each material, but multiple tests were performed on each material even when only one is shown for clarity in later figures. Additional data on other tests performed have been included in the Appendix Section. From Figure 3-4, it can be seen that the advanced ceramics exhibit linear behavior up to some failure point, when they begin to unload abruptly. For AD85-1, the failure behavior shows an initial rise in stress while strain begins to decrease, before the stress begins to decrease as well. AD995-1 has a brief transition zone before it begins to unload along a similar path it took while loading. SiC-1 shows a decrease in strain but near constant stress after failure. This behavior is indicative of the DIC strain measurements and the strain gauge measurements becoming asynchronous with each other as the surface begins to fail while the load applied to the entire cross-section of the system that is recorded by the strain gauges remains near constant. While these results are unlikely to be physical, they are the best data available and are useful for understanding failure mechanisms such as whether the surface of a sample fails before the interior. The general responses for all tests rather than these specific tests can be found in Table 3-1. While the samples fail before they return to zero stress, if projected to zero stress, the change in apparent stiffness means that only AD995-1 would return to zero strain at zero applied stress, and this behavior is not seen in other AD995 samples. In contrast to the advanced ceramics, the cermets have a stress-strain curve that increases linearly up to the yield point of 3100±300 MPa at 0.90±0.02% strain, where the curve reaches a peak. After undergoing stress relaxation, the material then begins to strain harden. Sample TitanMade-1 does not reach a second local maximum, while other samples will reach a second peak at 2800±500 MPa at 1.7±0.2% strain[107]. After this point the material continues to decrease in stress as strain increases, up until ultimate failure at 2.6±0.3% strain. This hardening-softening behavior is discussed in more detail in the paper by Li *et al*[110], and is related to the metal matrix phase undergoing alternating thermal softening and strain hardening.

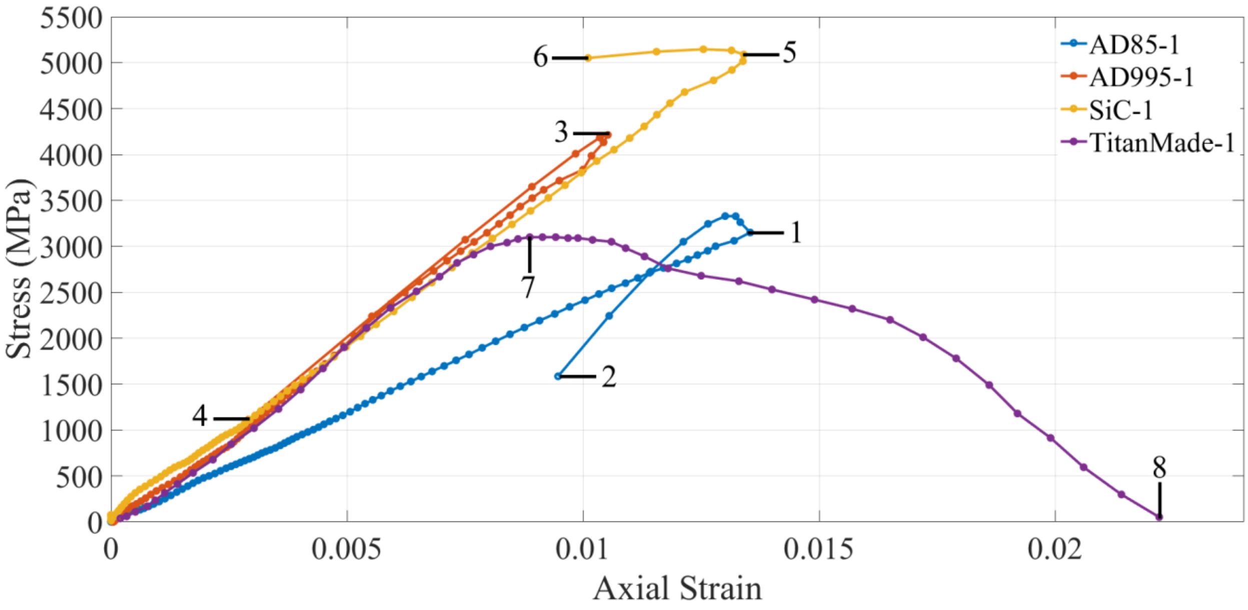

Figure 3-4 – Stress-strain curves for advanced ceramics AD85, AD995, and SiC, and TitanMade® cermet under dynamic loading, obtained from combined strain gauge measurements and high-speed DIC. Key points are (1) AD85-1 maximum strain, (2) AD85-1 failure, (3) AD995-1 maximum stress and strain, (4) AD995-1 failure (the curve goes back to the left from 3), (5) SiC-1 maximum strain, (6) SiC-1 failure, (7) TM-1 maximum stress, and (8) TM-1 failure. The advanced ceramics show linear loading up to maximum stress followed by a decrease in stress and strain before failure. By contrast, the cermet samples show an initial linear loading followed by softening and long increases in strain without significant increases in stress before stress begins to drop as strain continues to rise.

Next, Figure 3-5 explores the axial and lateral strains relationships taken from DIC measurements for each material. These measurements allow us to assess the Poisson's ratio and internal crack evolution. For the advanced ceramics, their axial versus lateral behavior is mostly linear up until reaching a softening-hardening-phase, wherein the lateral strain increases faster than the prior linear slope and then decreases to where it would have been had it followed the original linear slope. Following this point the ceramics reach their maximum strain point, after which there is a rapid increase in lateral strain and a simultaneous decrease in axial strain. The rapid increase is likely caused by internal cracks expanding laterally during failure. On average, the Poisson's ratio over this linear regime is 0.23±0.02 for AD85, 0.29±0.08 for AD995, 0.17±0.04 for SiC, and 0.39±0.05 for the cermet. These averages and standard deviations are taken across *all* experiments that were performed. Once the materials transition from linear to non-linear behavior, the average values are 0.26±0.13 for AD85, 0.22±0.16 for AD995, and 0.20±0.30 for SiC. Further discussion of these values and their meaning will come in the discussion of damage evaluation in the Discussion section. In contrast, the cermets have a near-quadratic lateral vs. axial strain curve, starting with an apparent Poisson's range ratio of 0.26±0.12 and ending with a range of 0.48±0.11.

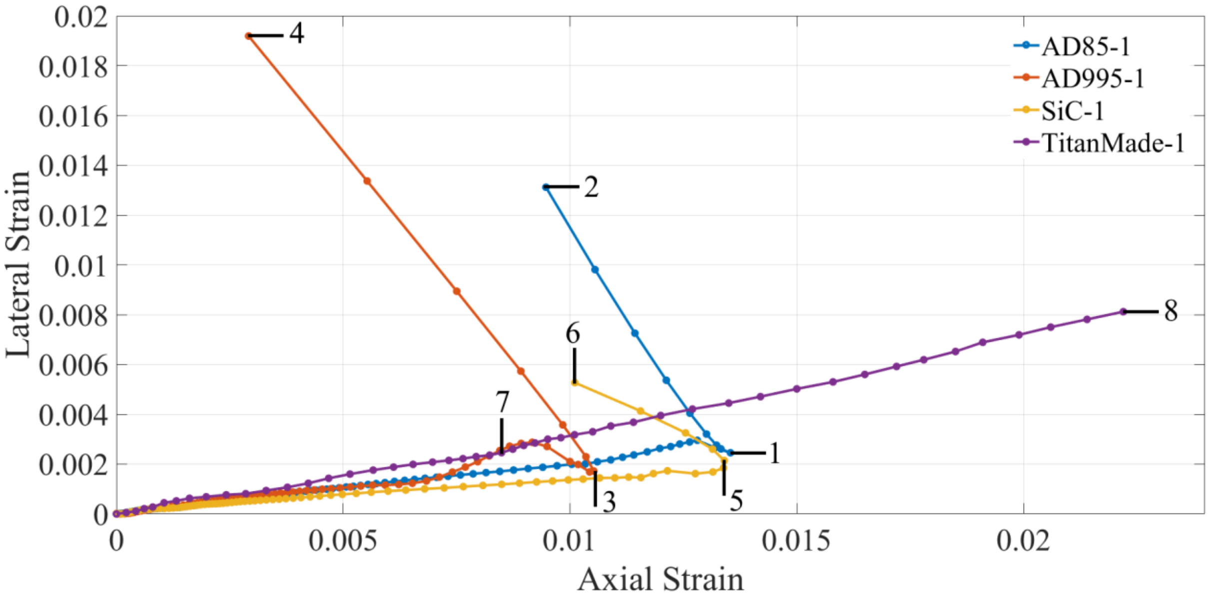

Figure 3-5 – Lateral vs. axial strain curves for AD85, AD995, SiC, and TitanMade® cermet under dynamic loading, obtained from high-speed DIC. Key points are (1)AD85-1 maximum strain, (2) AD85-1 failure, (3) AD995-1 maximum stress and strain, (4) AD995-1 failure, (5) SiC-1 maximum strain, (6) SiC-1 failure, (7) TM-1 maximum stress, and (8) TM-1 failure. The advanced ceramics demonstrate complex load paths with changes in the ratio of lateral to axial strain before reaching unloading, at which point axial strain decreases while lateral strain sharply increases. In contrast the cermet samples show a continual increase of lateral strain with axial strain.

3.4. Formulation

3.4.1. Theoretical Foundation

In this section we present a method to extend prior damage models [55,100] to include changes to the apparent Poisson's ratio in order to analyze the experimental data from this current study. While these models can include anisotropy and off-axial behavior in simulation[55], it is not possible to determine experimentally if a change in axial-lateral response comes from a change in lateral elasticity or from a change in Poisson's ratio. In order to include damage to Poisson's ratio, in this section we present a formulation that starts with an assumption of isotropic, linear elasticity. This assumption is chosen because brittle materials behave linearly elastically up until failure[127], and that damage begins to accumulate once a certain strain threshold is reached[51,62,123]. By adding in damage functions in linear superposition with the elasticity equations, the degree of strain required for damage to begin accumulating can be determined from when the materials begin to significantly deviate from linear elastic behavior. By adding damage functions to the linear elastic equations it is possible to ensure effects from crack growth and reorientation are being accounted for.

Modelling begins with the two-dimensional compliance tensor with stiffness damage term seen in Equation (3-2). The compliance tensor is used for similarity with Nemat-Nasser and Horii[56] and for simplifying a later argument. The damage term, *D*, affects the apparent Young's modulus such that no damage (D=0) results in no change to the compliance of the material, while total damage (D=1) results in the material having no resistance to deformation.

$$\begin{Bmatrix} \varepsilon_{11} \\ \varepsilon_{22} \\ 2\varepsilon_{12} \end{Bmatrix} = \frac{1}{E(1-D)} \begin{bmatrix} 1 & -\nu & 0 \\ -\nu & 1 & 0 \\ 0 & 0 & 2+2\nu \end{bmatrix} \begin{bmatrix} \sigma_{11} \\ \sigma_{22} \\ \sigma_{12} \end{bmatrix} \tag{3-2}$$

We then introduce a new damage term that acts upon the Poisson's ratio of the material, while retaining the factor that acts upon the Young's modulus. The factor that acts upon the Young's modulus is renamed to D_E, and the factor that acts upon the Poisson's ratio is named as D_ν. This process results in Equation (3-3).

$$\begin{Bmatrix} \varepsilon_{11} \\ \varepsilon_{22} \\ 2\varepsilon_{12} \end{Bmatrix} = \frac{1}{E(1-D_E)} \begin{bmatrix} 1 & -\nu(1+D_\nu) & 0 \\ -\nu(1+D_\nu) & 1 & 0 \\ 0 & 0 & 2+2\nu(1+D_\nu) \end{bmatrix} \begin{bmatrix} \sigma_{11} \\ \sigma_{22} \\ \sigma_{12} \end{bmatrix} \tag{3-3}$$

Initial validation experiments require a simpler set of variables to explore, but anisotropy can be introduced by giving different D_E and D_ν values for different dimensional axes, or an entire damage tensor that modifies all elastic constants. The equations are further simplified by removing shear. For uniaxial loading, each strain component becomes Equations (3-4) and (3-5):

$$\varepsilon_{11} = \frac{\sigma_{11}}{E(1-D_E)} \tag{3-4}$$

$$\varepsilon_{22} = \frac{-\sigma_{11}\nu(1+D_\nu)}{E(1-D_E)} \tag{3-5}$$

Rearranging Equations (3-4) and (3-5) to express both a linear and non-linear contribution produces Equations (3-6) and (3-7).

$$\varepsilon_{11} = \frac{\sigma_{11}}{E} + \frac{\sigma_{11}D_E}{E(1-D_E)} \tag{3-6}$$

$$\varepsilon_{22} = \frac{-\nu\sigma_{11}}{E} - \frac{\nu(D_E+D_\nu)\sigma_{11}}{E(1-D_E)} \tag{3-7}$$

Comparing these equations with Equation (3-1), Equations (3-6) and (3-7) will only account for strains generated when stress is present, where the microcrack formulation of Nemat-Nasser and Obata[56] in Equation (3-1) allowed for strains generated by crack sliding and opening be present even when $\sigma = 0$. Experimentally, these would appear as residual strains present after a material has been loaded sufficiently to cause damage and then unloaded, a phenomenon seen previously in experiments on concrete[102]. Such damage is not expected in pristine advanced ceramics, but severely cracked but not yet fragmented material such as in a ballistic impact[4,106] leads to such a damage value being necessary to keep track of when studying non-pristine samples. These damage values, since they are not related to the presence of stress, are dependent upon the strain history of a sample. Continuing the assumption of isotropy, D_ε, a damage term that represents residual strain can be added into Equations (3-6) and (3-7) to arrive at the following:

$$\varepsilon_{11} = \frac{\sigma_{11}}{E} + \frac{\sigma_{11}D_E}{E(1-D_E)} + D_\varepsilon \tag{3-8}$$

$$\varepsilon_{22} = \frac{-\nu\sigma_{11}}{E} - \frac{\nu(D_E+D_\nu)\sigma_{11}}{E(1-D_E)} - \nu(1+D_\nu)D_\varepsilon \tag{3-9}$$

From prior literature on concrete[102] subjected to load-unload experiments, D_ε is likely a function of the maximum strain experienced by a material. In the load-unload experiments on concrete, the unload path would show a higher stiffness than when it had been loaded enough to cause damage. When reloaded, the new load path would then follow the unload path until it reached the prior stress-strain condition, at which point the stiffness would drop again, as if the sample had never been unloaded. In experimental results in the literature, this behavior did break down as higher maximum strains were reached[102], suggesting that damage to elastic properties consists of both permanent and strain-dependent elements.

The possibility of damage consisting of both permanent and strain-dependent components allows for the possibility that D_E and D_ν can have negative values. For brittle materials, an increase in stiffness is not expected, but since materials such as metals and plastics can undergo strengthening mechanisms when strained, then it is not impossible to consider the possibility of a negative D_E value, which is an increase in stiffness. For D_ν, a negative value would correspond to a decrease in Poisson's ratio, which corresponds to a decrease in volume conservation. Under a compressive load, this would be associated with a loss of volume, which would mean that cracks would be closing rather than opening. For D_E in ceramics, the most likely cause of a negative value would be crack closure producing an apparent increase in stiffness over initial values as void spaces are pressed into each other. For pristine samples this is not likely a significant concern, but for damaged material this remains a distinct possibility.

The combination of D_E and D_ν values thus provides insight into how internal cracks evolve during loading. How elastic constants are changing informs how crack surfaces are moving and thus demonstrates the relationship between physical damage and mechanical damage. In order to keep nomenclature ordered, this paper will break from prior convention and allow D_E to have any value rather than varying from 0 to 1. This requires changing the sign conventions. Under this convention, $D_E = -1$ is the same as $D = 1$, and $D_E < -1$ corresponds to a negative stiffness. A negative stiffness is not considered a physical result and does not appear in experiment. The adoption of this nomenclature modifies Equations (3-8) and (3-9) as follows.

$$\varepsilon_{11} = \frac{\sigma_{11}}{E} + \frac{\sigma_{11} D_E}{E(1+D_E)} + D_3 \tag{3-10}$$

$$\varepsilon_{22} = \frac{-\nu\sigma_{11}}{E} - \frac{\upsilon(D_E - D_\nu)\sigma_{11}}{E(1+D_E)} - \nu(1 + D_\nu)D_\varepsilon \tag{3-11}$$

These conventions allow for experimental results that include apparent changes to Poisson's ratio to be analyzed in the same way as changes in apparent stiffness could be analyzed as damage[36,55,100]. These conventions also allow for the apparent stiffness to increase, which had previously not been considered possible. This apparent rise in stiffness in response to physical damage can be explained through D_E and D_ν varying simultaneously. This leads to insights on the microstructure evolution that can produce these counter-intuitive macroscopic observations.

3.5. Damage Evaluation

Experimental damage values for D_E and D_ν are presented in Figure 3-6 and Figure 3-7, respectively. These values are obtained by taking the definitions of damage seen in Equations (3-12) and (3-13):

$$D_E = \frac{E_{app}}{E_0} - 1 \tag{3-12}$$

$$D_\nu = \frac{\nu_{app}}{\nu_0} - 1 \tag{3-13}$$

where E_0 and ν_0 are the pristine Young's modulus and Poisson's ratio from Table 3-1, respectively, and E_{app} and ν_{app} are the apparent Young's modulus and Poisson's ratio, respectively. The apparent elastic properties are approximated as using Equations (3-14) and (3-15):

$$E_{app} = \frac{\sigma_{inst}}{\varepsilon_{1_{inst}}} \tag{3-14}$$

$$\nu_{app} = \frac{\varepsilon_{2_{inst}}}{\varepsilon_{1_{inst}}} \tag{3-15}$$

where σ_{inst} is the instantaneous stress, $\varepsilon_{1_{inst}}$ is the instantaneous axial strain, and $\varepsilon_{2_{inst}}$ is the instantaneous lateral strain. "Instantaneous" here refers to each individual data point seen in Figure 3-4 and Figure 3-5, and each individual data point has its own stiffness calculated at each moment as a secant line drawn from the origin. Because the data has already gone through a filter, no further averaging or filtering is needed with this method, although due to the earliest points of the curve being from before the sample is in stress equilibrium, the first few points are excluded as being non-physically high or low (negative stiffness, stiffness more than double a pristine value). The pristine values E_0 and ν_0 are the quasi-static values. While ideally the starting strain is when D_E and D_ε are both zero, if one of these values remains in a non-pristine state then a starting point is decided from when the other value is at or near 0. This is seen in Figure 3-6 with AD995-1 and TM-1 samples, which exhibit an initially low stiffness in the beginning. An example of how D_E and D_ν evolve simultaneously with axial strain starting with both values at 0 is seen in Figure 3-8, which shows both D_E and D_ν versus axial strain for a representative sample of AD85 alumina, and also includes frames from the ultra-high-speed camera. Each material went through this analysis, with Figure 3-6 and Figure 3-7 showing a representative case from each material for their D_E and D_ν evolution with axial strain, respectively. In the test shown in Figure 3-8, an initial stiffness of 240 GPa was found for AD85-1, within the uncertainty of the quasi-static value of 220±20 GPa, while the Poisson's ratio begins at the value of 0.22, the same as the quasi-static value of 0.22±0.03. The stiffness remains at $|D_E|$ <0.05 of the pristine value up to 1.3% strain, indicating little D_E damage accumulation occurs until just before failure, and D_E only increases beyond a magnitude of $|D_E|$ <0.05 once the axial strain begins to decrease during unloading. In contrast, D_ν damage for AD85-1 shows a consistent decrease to a value of D_ν = -0.12 before beginning to rise at 1.1% strain, seen in Figure 3-8-Image 1. This also serves as an example of the sample showing no signs of surface damage, while at the same time D_ν decreases towards a local minimum of -0.20. Figure 3-8-Image 2 shows the first image where evidence of cracking becomes evident, with these cracks occurring at the corners of the samples where stress concentration would be the highest. Ideally, the samples would be dumbbell shaped to reduce stress concentration factors[115], but for our purposes the flat faces are required for DIC and for other experiments involving the tracking of crack speeds at the surface[109], and the trade-off was considered acceptable. Figure 3-8-Image 3 shows more extensive surface damage accumulating at the corners of the specimen and is at the maximum strain of 1.4% strain before beginning to decrease, where D_E is only at -0.03 and D_ν reaches its lowest point of -0.18. Finally, in Figure 3-8-Image 4, the surface damage is beginning to intrude into the DIC area of interest, and no further data is collected past this point as image correlation is lost and strains cannot be determined once cracks are present within the area of interest. The loss in correlation can also be seen in Figure 3-3, where the strain curves from DIC end approximately 10 μs before the stress curve taken from the Kolksy bar. Damage values are only calculated when both strain and stress values are available, and thus Figure 3-8-Image 4 represents the last possible measurement of the material behavior considered. At the end point, D_E= -0.49, the lowest point on the curve, while D_ν has a value of 5.3, which is not likely a value relating to an actual Poisson's ratio, but instead represents long axial cracks opening and physically separating the test specimen. As a final observation, if the material has incurred a permanent deformation then strain will not return to zero at zero stress, and thus the unloading slope would necessarily have a different stiffness than the loading slope. The inclusion of D_ε into the formulation is intended to deal with this issue, although under dynamic loading conditions it is currently not practical to determine how these values evolve because the materials fragment during failure and, thus, permanent deformation cannot be examined quantitatively at this time.

The plots of D_E versus axial strain for exemplar experiments of each of the materials that are studied is shown in Figure 3-6. The same materials for D_ν versus axial strain are shown in Figure 3-7. The advanced ceramics all exhibit catastrophic failure after maximum strain, and D_E and D_ν damage values for the advanced ceramics do not go below -0.3 before maximum strain, with all the materials remaining within ±0.05 of their pristine stiffness value for the majority of their strains. The exception among the advanced ceramics to this is AD995-1, which shows the property of an initial low value of D_E = -0.11 before increasing to its pristine value and then remaining around zero damage for the rest of the experiment, including during unloading. The cermet also shows this initial increase in stiffness before reaching its pristine value and then continuously loses stiffness as strain increases.

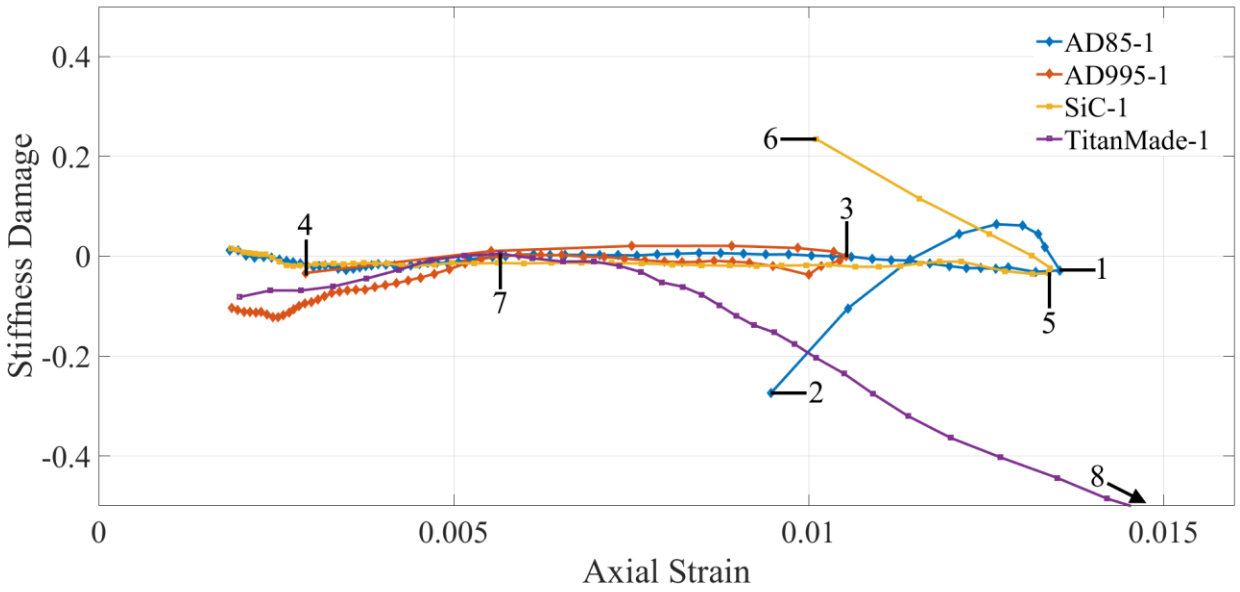

Figure 3-6 – $\boldsymbol{D_E}$ versus axial strain curves for AD85-1, AD995-1, SiC-1, and TM-1 cermet under dynamic loading. Due to noise early in the experiment, points below 0.001 strain are removed. Key points are (1) AD85-1 maximum strain, (2) AD85-1 failure, (3) AD995-1 maximum stress and strain, (4) AD995-1 failure, (5) SiC-1 maximum strain, (6) SiC-1 failure, (7) TM-1 maximum stress, and (8) TM-1 failure. As TM-1 has a $\boldsymbol{D_E}$ of -0.99 at failure, it has been excluded in order to better show the features of the adanced ceramics. The advanced ceramics have minimal stiffness evolution before catastrophic failure as axial strain decreases. While AD85-1 and AD995-1 demonstrate a loss of stiffness at the end of the test, SiC-1 demonstrates an increase in strength. In contrast the cermet shows an extended loss of stiffness through the entire loading process and continually increases in strain. Additionally, both AD995-1 and the cermet experience an initial period of stiffness gain before reaching their pristine value and then decreasing in stiffness once again.

Contrasting the D_E damage in Figure 3-6 with the D_ν damage in Figure 3-7, the advanced ceramics show a general decrease in Poisson's ratio, while the cermet shows a near linear increase. The major complexity is that the advanced ceramics show a large increase in D_ν after they reach their maximum axial strain points and then begin to unload. AD995 has the most complex D_ν curve, with an initial linear decrease from D_ν=0 at the start to a value of -0.21 at 0.65% strain, which is also the point at which cracking appears on the surface of the sample in the high-speed camera images. D_ν then increases to a local maximum of 0.32 at 0.89% strain before decreasing to a minimum value of -0.33 at 1.04% strain. As a fortunate visual guide in Figure 3-7, the minimum of the AD995-1 D_ν curve intersects with a section of the SiC curve before and after this rise and fall behavior in D_ν. This rise and fall behavior in D_ν is seen in all of the advanced ceramic samples presented, with AD995-1 showing the most pronounced version of a softening-hardening-phase and SiC-1 barely having any of this phase. Both AD85-1 and AD995-1 have their hills return to where they would have been had they followed their linear D_ν vs. strain trend and then reach maximum strain and begin to fail. SiC-1 has a small gap between its softening-hardening phase and maximum strain. From Figure 3-7, the key takeaway is that the stronger materials of AD995-1 and SiC demonstrate large decreases in Poisson's ratio, while the weaker materials of AD85-1 and the cermet demonstrate D_ν damage that is close to zero or increases. In terms of actual rather than normalized values of Poisson's ratio, the strongest and stiffest materials show the lowest Poisson's ratio (AD995-1 and SiC-1 both $\nu<0.2$ for the majority of their axial strain curves), while the weaker materials have the highest Poisson's ratio (AD85-1 and TM-1 both $\nu>0.22$ for the majority of the axial strain curves). With this considered, the final key observation is that all the materials fail with a positive D_ν value. This indicates an increase in Poisson's ratio, and thus an increase in the internal volume compared to the pristine state. This likely indicates that cracks are all expanding laterally and increasing the volume of the material. This observation is also seen in the high-speed-camera images such as those shown in Figure 3-8-Images 3 and 4, as the samples all disintegrate laterally outward. While not surprising, it is believed that this is the first time in the literature that such behavior has been quantified. The softening-hardening-phase seen in the D_ν vs. strain behavior of the advanced ceramics may be related to the opening of an initial population of cracks that then collapse again, with maximum strain being reached shortly after these cracks close.

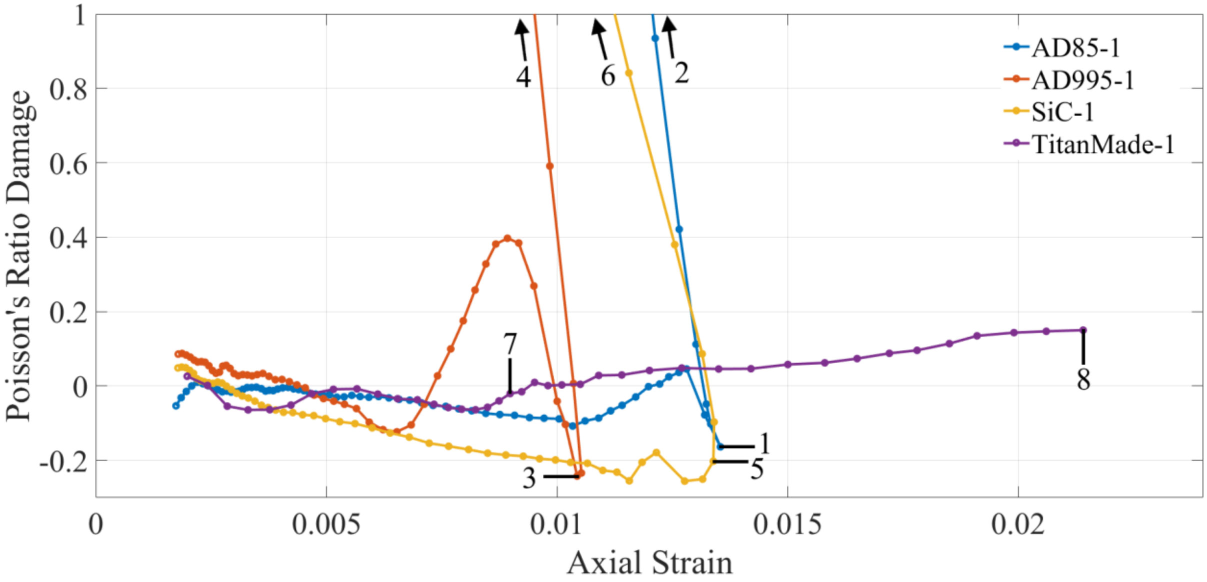

Figure 3-7 – $\boldsymbol{D_{\nu}}$ versus strain for AD85-1, AD995-1, SiC-1, and TM-1 cermet under dynamic loading. Due to noise early in the experiment, points below 0.001 strain are removed. Key points are (1) AD85-1 maximum strain, (2) AD85-1 failure, (3) AD995-1 maximum stress and strain, (4) AD995-1 failure, (5) SiC-1 maximum strain, (6) SiC-1 failure, (7) TM-1 maximum stress, and (8) TM-1 failure. The advanced ceramics demonstrate a decrease in Poisson's ratio through the loading process, before demonstrating a sharp rise as axial strain decreases. The advanced ceramics also show a rise and sharp decline in $\boldsymbol{D_{\nu}}$ just before the unloading segment, with the phenomenon being the most pronounced in AD995-1 and least pronounced in SiC-1. The cermet on the other hand shows a near continuous increase in $\boldsymbol{D_{\nu}}$. All these brittle materials demonstrate a positive final Poisson's ratio damage at failure. Comparing with Figure 3-4 and Figure 3-6 AD995-1 and SiC-1 show the largest decrease in Poisson's ratio before failure while having the highest stiffness and failure strength of the materials studied, suggesting that a negative $\boldsymbol{D_{\nu}}$ is significant in the strength of brittle materials.

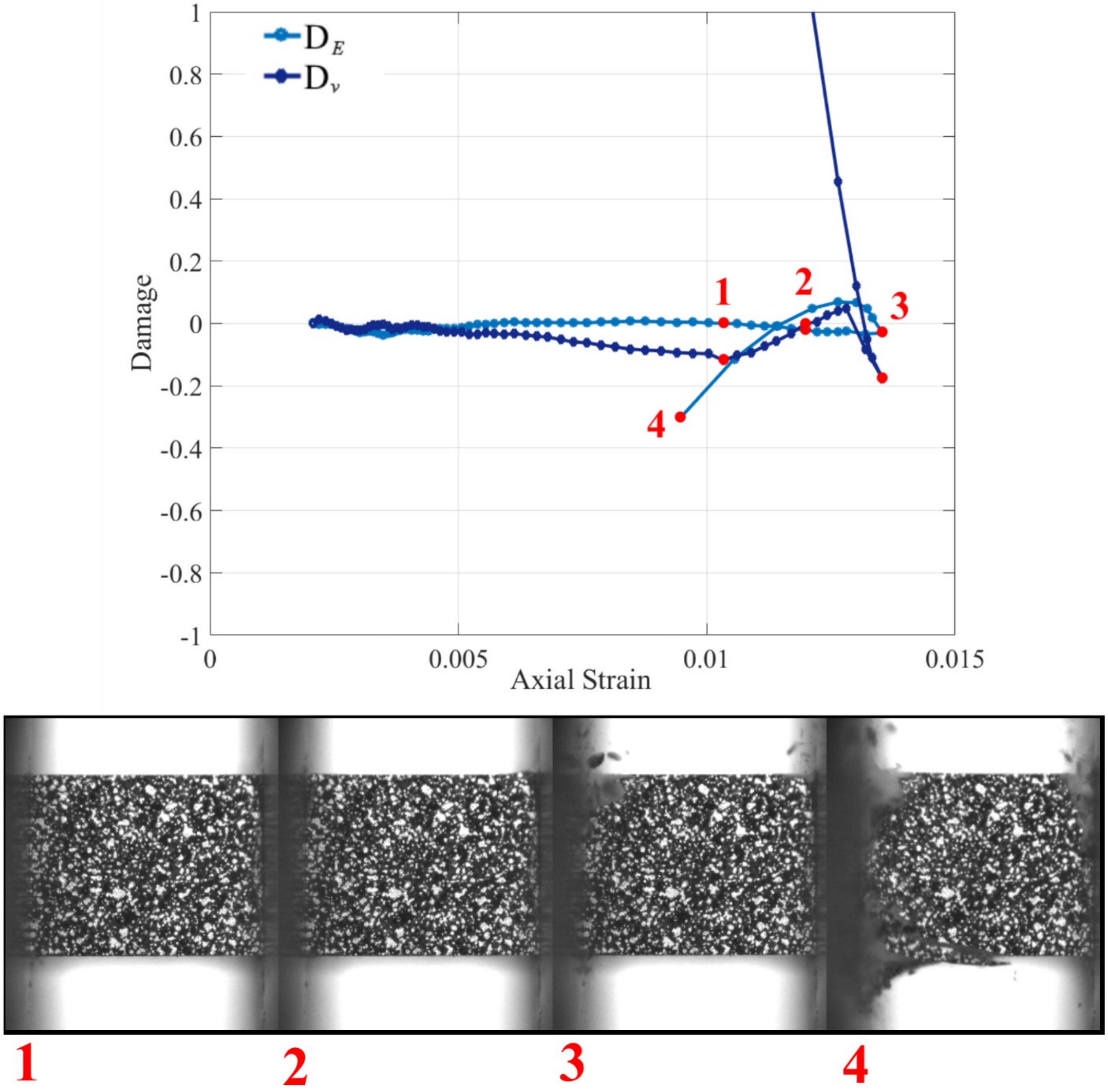

Figure 3-8– $\boldsymbol{D_E}$ and $\boldsymbol{D_\nu}$ damage curves for AD85-1 alumina and the images associated with various points on the plots. Image 1 shows the sample before damage has become visible on the surface, and is also a local minimum for $\boldsymbol{D_\nu}$. Image 2 is when the first cracks appear at the upper corners of the sample, indicated by arrows. Image 3 is the absolute minimum for $\boldsymbol{D_E}$ and $\boldsymbol{D_\nu}$. Image 3 is when the material is at maximum strain of 1.35% and $\boldsymbol{D_\nu}$ is at its lowest. Image 4 shows the last frame where coherent data is obtained from the DIC measurements; beyond this point surface cracking moves into the area-of-interest and halts measurement.

3.6. Discussion

3.6.1. Observation Discussions

From comparing Figure 3-6 and Figure 3-7 with Figure 3-4 and Table 3-1, the primary takeaway is that the accumulation of negative D_E damage before failure is not necessarily indicative of a weaker material. The TitanMade® cermet shows an initial low D_E that increases up to $D_E = 0$, before showing continual negative D_E accumulation to failure. The cermet also has the highest ultimate yield strain of the materials studied. In contrast, a negative and decreasing D_ν value and a low Poisson's ratio are associated with the stronger and stiffer materials, while a positive D_ν is associated with fragmentation and failure of all the studied materials. Taken together, this suggests that positive D_ν accumulation is a stronger indicator of failure than negative D_E. This has implications in micro-mechanical modelling of these materials[111], which is discussed later. Following this possibility, it is notable that for the AD995 sample shown in Figure 3-7, which while stiffer and stronger than AD85, has the lowest failure strain of the materials studied and demonstrates a rise and then fall pattern for D_ν. Positive D_ν values indicate internal volume increase, which as a macroscopic observation implies microscopic crack sliding and crack growth. As these phenomena are associated with increased strains for a given stress as in Equation (3-1), this is a sensible physical observation.

One way of examining the implied physical behavior of these material systems is to plot D_E and D_ν against each other in order to visualize how the two damage variables are related. The representative materials are plotted in this way in Figure 3-9, with D_E on the x-axis and D_ν on the y-axis. Segmenting this graph into the standard Cartesian quadrants produces the following implications of combined behavior:

- **Quadrant I** - D_E and D_ν positive: cracks are opened and stiffness increased. This is likely a non-physical combination that occurs when the measured stress experienced by the entire body and the strains measured at the surface by DIC are not in agreement. Outside of noise factors, the most likely reason for a material to be in this quadrant is that it is explosively fragmenting, with the interior still maintaining stress while the exterior is expanding outward, producing an apparent decreasing axial strain in DIC. While this shows the limitations of the DIC method when measuring catastrophic brittle failure, the results do provide qualitative insight into material failure processes, as it suggests that the material fails at the surface before it fails in the interior. Behavior in this quadrant comes from the damage values obtained being a global value, while the failure process is a local phenomenon. As a simple short-hand, we refer to this type of behavior as the ‘fly-apart mode’.

- **Quadrant II** - D_E negative and D_ν positive: cracks are opened and stiffness decreased. This is the expected change in properties in brittle materials from microcrack dilatancy theory[56], and will be called the ‘void growth mode’.
- **Quadrant III** - D_E and D_ν both negative: cracks are closed and stiffness decreased, suggesting that a material has been compacted into itself. This is most likely to occur early in a test as initial porosity is crushed out and crack faces mostly perpendicular to the loading direction are forced into contact with each other. This will be called the ‘crush-out mode’.
- **Quadrant IV** - D_E positive and D_ν negative: cracks are closed and stiffness increased, suggesting that porosity that had previously decreased apparent stiffness has been crushed out. This mode is most dependent upon what values are chosen as being the pristine value. This is an issue for any material that exhibits strain-rate dependency for E_0, since if one assumes that the quasi-static values are the pristine stiffness, and dynamic loading is capable of causing an increase in stiffness, then this mode is possible. Conversely, if one assumes that quasi-static loading produces a lower stiffness and that dynamic loading produces the “true” value, then this mode is non-physical because the highest observed value of D_E should be 0. Because of the assumed dependence upon cracks to be closed to achieve this state, this shall be called the ‘closed-crack mode’.

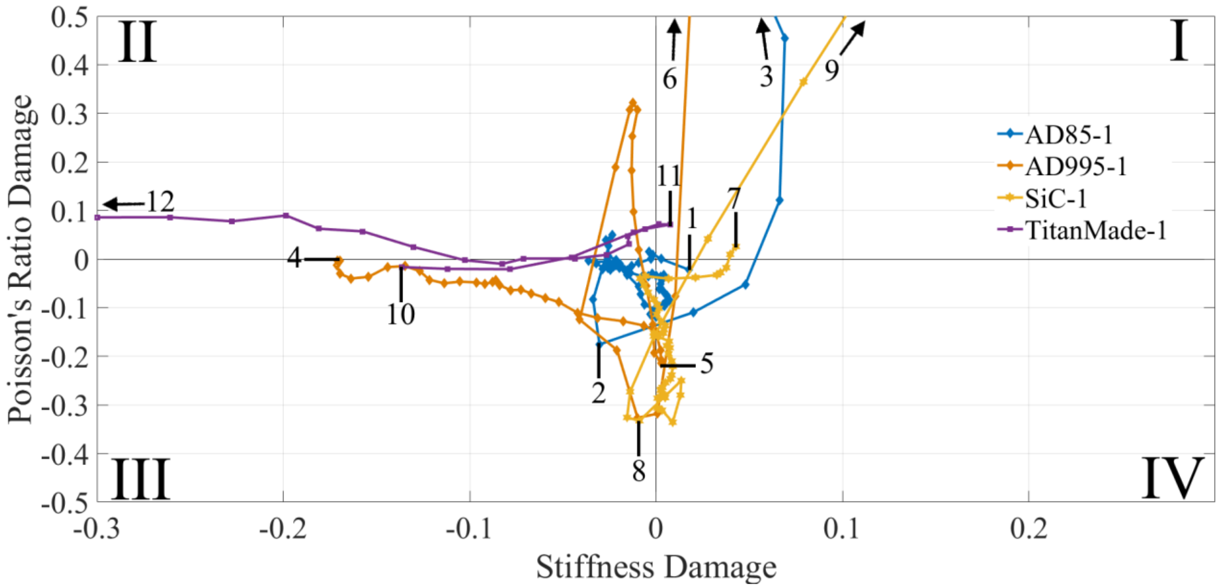

Figure 3-9 – $\boldsymbol{D_E}$ versus $\boldsymbol{D_\nu}$ for AD85-1, AD995-1, SiC-1, and TM-1 cermet under dynamic loading. Key points are (1) AD85-1 start point, (2) AD85-1 maximum strain, (3) AD85-1 failure, (4) AD995-1 start point, (5) AD995-1 maximum stress and strain, (6) AD995-1 failure, (7) SiC-1 start point, (8) SiC maximum strain, (9) SiC-1 failure, (10) TM-1 start point, (11) TM-1 maximum stress, and (12) TM-1 failure. The cermet demonstrates a similar load and unload path before it diverges, and begins to lose all stiffness while $\boldsymbol{D_\nu}$ continues to increase. The advanced ceramics demonstrate a much more complex relationship between $\boldsymbol{D_E}$ and $\boldsymbol{D_\nu}$. The Roman numerals indicate the different Cartesian coordinates corresponding to fly-apart (I), void-growth (II), crush-out (III), and crack-closed (IV).

Further distinction can be made for the direction of the damage path. The path leading away from the origin (0,0) is indicative of the material accumulating damage, while a path moving towards the origin is indicative that the material is recovering material properties from being damaged. Distance from the origin can also be used to better qualify whether a material is intact, damaged, or disintegrating, which can be seen in Figure 3-10. Figure 3-10 shows the D_ν vs. D_E curve for the same AD85 test as seen in Figure 3-8, but adds in boxes to denote probable damage space boundaries of intact-to-damaged and damaged-to-fragment transitions. These boxes are based on averaged maximum and minimum values of D_E and D_ν before surface cracking appears (such as in Figure 3-8, Image 2) for the 'intact' values, and then after surface cracking but before failure for the 'damaged' values. Each material was examined independently in this manner, so the boxes in Figure 3-10 are based upon all AD85 tests. While primarily a qualitative method of behavior visualization rather than a quantitative descriptor of what D_E and D_ν values definitively mark the behavioral boundaries, Figure 3-10 shows a number of key points that make understanding Figure 3-9 easier. First, the 'intact' box is roughly symmetric and centered on the origin, with a small bias towards being in Quadrants II and III, suggesting that the variations from pristine are likely a combination of measurement noise and the material being able to tolerate negative damage values better than positive damage values. In comparison, the damaged region is strongly asymmetric and not centered on the origin, showing that there is a preference for the curves being in Quadrant II when damaged, the void growth quadrant where volume is increased and stiffness decreased. Secondly, the intact boundary is within 10% of the origin in all directions, and contains 70% of all of the points on the curve. From Paliwal and Ramesh[55], the expectation is that the damage is continuously increasing throughout the test, with their equivalent of D_E falling beneath -0.05 at 87% of maximum strain, and max stress being reached at 94% of maximum strain. The results in this paper show that if the onset of failure is signified by damage accumulation greater than 5% variation from pristine values, then failure occurs at a lower strain than expected[55] if tracking failure by the evolution of D_ν. However, if taking failure as being related to maximum stress as with Paliwal and Ramesh[55], then the material is able to accumulate a greater than 5% increase in D_E, which is not predicted[55]. If taking only negative D_E values as indicative of failure, then the observed values are again greater than those predicted by Paliwal and Ramesh[55], with Figure 3-8 having a minimum D_E of -0.48 in comparison to a predicted value of -0.2. The third major point to observe is that while the intact section has the points tightly clustered, the points beyond that line are more widely spaced from each other, indicating that the material was changing its stress-strain behavior much more quickly than when it was behaving in a linear elastic manner.

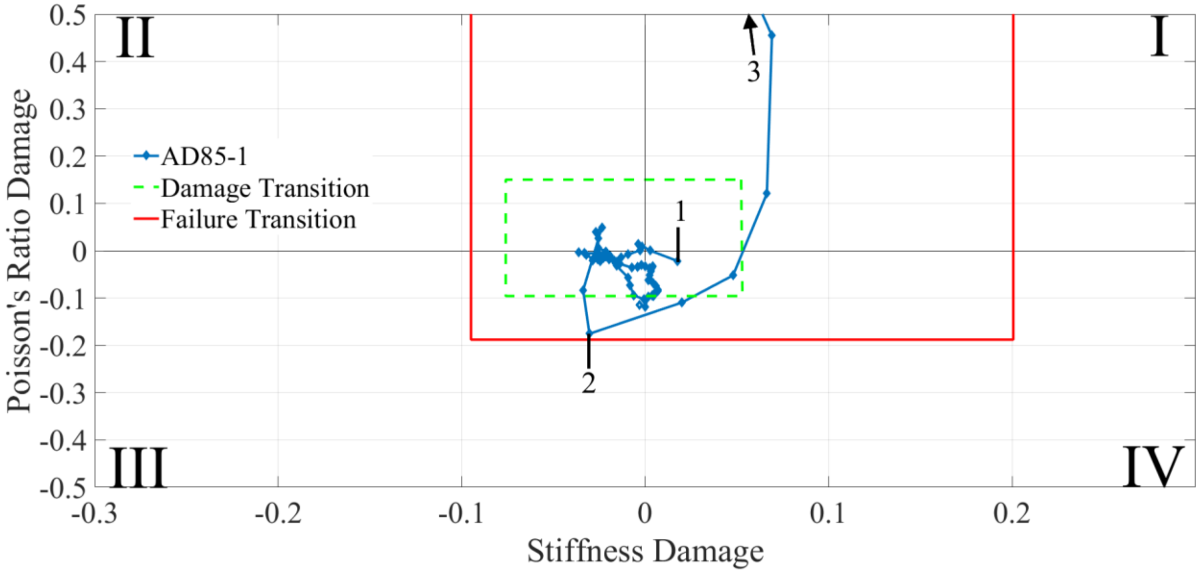

Figure 3-10 – D_E versus D_ν for the same AD85-1 sample shown in Figure 3-8, with boundaries drawn based on the maximum values of transitionary behavior for AD85-1 across multiple tests. Key points are (1)AD85-1 start point, (2)AD85-1 maximum strain, and (3)AD85-1 failure. The intact to damaged bound is based off the values for D_E and D_ν where surface cracks begin to appear on the surface, while the damaged to failure bounds are based on the values for when the sample disintegrates. For the majority of a test the sample remains within the intact bounded region, with only a few points in the damaged region. While the material ends its curve within the damaged boundary, for all the tests the curves move outside the damaged to failure boundary at some point.

Returning to Figure 3-9, each material has its own distinctive pattern in the damage space. AD85 exhibits a sort of quasi-spiral around the origin, indicative of D_E and D_ν changing simultaneously with each other. By contrast, the points for AD995 form a pair of lines, one in Quadrant II where the stiffness of the material increases to its pristine state while D_ν increases, while the second line is vertical around the y-axis, showing that for AD995 all damage accumulates in the Poisson's ratio rather than the stiffness. SiC shows almost all of its initial damage in D_ν before it fails, and both D_E and D_ν increase simultaneously, sending the curve into Quadrant I. Finally, the cermet has D_E and D_ν changing simultaneously with each other along a primarily linear slope in Quadrant II, showing that it has a void growth behavior consistent with expected brittle materials continuously accumulating damage to both stiffness and Poisson's ratio[56]. The cermet has a similar initial behavior to AD995 with a lower stiffness that increases to its pristine value while its Poisson's ratio changes, but as the material fails, it moves back along the same D_ν vs D_E path as it took initially. The cermet then begins progressing along a new slope in which D_E decreases as D_ν increases. Combined with the behavior of AD995, this suggest that there may be 'intact' and 'damaged' curves in the damage space that the materials are constrained to move along while being strained. Given the materials show evidence of moving backwards along their damage space curves before changing their behavior from ‘intact’ to ‘damaged’, this further raises the possibility that the material behaviors have to move to intersection points of these curves in order to transition between them. Further experimentation will be required to map out these potential curves, including the effects of strain rate on their shape, but this analysis points towards how cracks physically open and shut when under load, and the internal complexities of relieving stresses. These experiments would involve a combination of simple repetition to define regions of interest, loading samples without causing failure in order to observe how intact specimens unload, and inducing damage before testing in order to examine what the effects of cracks have on this behavior. Figure 3-10 is currently an initial guiding method for how to consider the D_E and D_ν curves, and further analysis for the other materials will be held off until new data is obtained to better refine the numbers used and the shape of the intact and damaged areas.

3.6.2. Implications

Beyond the discussion of the data, implications of this research for the broader field of brittle materials research are now discussed. First, the data shows that damage accumulates in both the apparent stiffness and the apparent Poisson’s ratio. Second, damage accumulation occurs more strongly in the Poisson’s ratio than in stiffness for the advanced ceramics and cermet studied here. Third, the apparent values of both stiffness and Poisson’s ratio are capable of increasing as well as decreasing. Fourth, the combination of changes in macroscopic elastic properties can imply microscopic behaviors such as crack closure in addition to the already predicted and modelled crack opening[26]. All of these observations together show that damage accumulation in brittle materials can be non-linear, non-monotonic, and can accumulate in more than one direction even when loaded uniaxially. These results are of major importance for modellers, as it demonstrates new possible behaviors that are allowable in brittle materials and may have been dismissed as non-physical in the past.

Next, a comparison is made with other models that feature damage accumulation such as Johnson-Holmquist[26], Ravichandran and Subhash[128], Paliwal and Ramesh[55,62,129], and Tonge [49–51,100]. As a first comparison, note that residual stiffnesses are trivially captured by our formulation. For a completely damaged material ($D = 1$) where the pulverized state has 10%

of the stiffness of the intact material, the residual stiffness can be represented using a stiffness damage of D_E = -0.9. Thus, the system is overall compatible with these modelling approaches and one only needs to ensure that the proper conventions are being used in each case. The advantage that our framework has is that the addition of D_ν introduces an additional degree of freedom to track damage accumulation, which is particularly important for determining the failure path that a material takes as it is damaged, an important question in brittle material mechanics[130]. If physical damage in brittle material is irreversible, it can now be concluded that the manifestation of that damage in the apparent mechanical properties includes Poisson's ratio as well as Young's modulus. A material may be continuously accumulating damage but show no changes in stiffness until encountering catastrophic failure, such as the case of SiC-1 as seen in Figure 3-6 and Figure 3-7, where D_E remains almost 0 for the entirely of the test before suffering catastrophic failure, while D_ν shows a continual decrease. Additionally, since D_E can have both positive and negative values and is able to increase and decrease, this means that brittle materials can manifest increased stiffness if the damage accumulates within the Poisson's ratio instead, a situation not yet considered in the literature[51,55,105]. This is particularly important for materials that experience crack closure type behavior as it changes how modellers can conceive of material behavior. As an example, Ravichandran and Subhash[128] in their model reasonably exclude cracks less than a critical sliding angle as they are assumed to simply shut and not contribute to damage accumulation. Our experimental evidence now suggests that this is not the case, and that cracks perpendicular to the loading direction can contribute to the behavior of the material. While our data only shows that this is relevant at this point, research into mode-II shear by Rao *et al.*[131] and mixed mode failure by Ruiz *et al.*[132] helps guide our consideration of what would be physically happening by discussing how shear manifests in three-dimensional cracks under compression. Initial microcracks can be conceptually modelled as infinitesimally thin, but all real cracks are three-dimensional objects, and the act of pushing a void closed produces shear strains at the tips. Shear has been speculated to play a significant role in our previous work on crack propagation mechanics and crack speeds in AD85 and AD995 alumina[109], and prior work on boron carbide has also shown shear to be a significant contributor to amorphization and failure[91]. Thus while crack closure can lead to an apparent increase in stiffness with strain, it could also contribute to early failure, with porosity being a known cause of failure strength reduction for ceramics [33]. The macroscopic observations thus lead to new insights into microscopic mechanisms, which provides important new data for validating and constructing models and simulations[26,49,55,128].

For simulation in particular, the appearance of ‘fly-apart mode’ type failures, as seen with SiC-1 in Figure 3-9, has implications for developing boundary conditions used in simulation. The sample losing surface cohesion faster than the stress decreases implies that the material is fragmenting from the outside towards the inside while still sustaining some load even as it disintegrates. Simulations will typically work with representative unit cells in repeating patterns and then impose boundary conditions at the end of the samples to represent free or confined surfaces[111]. Being able to provide the physically observed behavior at the boundary will provide fresh information for simulation as to appropriate boundary conditions.

As a final implication that ties into the importance of boundary conditions to simulation, the way D_v evolves produces important insight for modellers. In the models of brittle fracture for ceramics[51,55,130], one of the core parameters is that invariably increasing confining pressure increases the failure strength[51,55,130]. The data in Table 3-1, Figure 3-4, and Figure 3-7 shows that a low Poisson’s ratio is associated with improved resistance to deformation. AD85 has the lowest stiffness and peak stress, and has the lowest D_v change before failure. AD995 and the cermet have the highest dynamic Poisson’s ratio, and while they have higher stiffness and yield strength, they also have lower yield strain. Of the two, AD995 shows a decreasing Poisson’s ratio and the cermet has an increasing Poisson’s ratio, and AD995 has a higher stiffness. Of all four materials, silicon carbide has the highest stiffness, lowest Poisson’s ratio, and exhibits a negative and decreasing D_v before failure. As Poisson’s ratio is a measure of lateral expansion in response to an axial strain, this immediately suggests that lateral confinement strengthening and low Poisson’s ratio being associated with stronger materials are related. From our perspective, a confining pressure is the same as an imposed maximum Poisson’s ratio, while from a pressure sensitive model perspective, a low Poisson’s ratio can be conceptualized as the material itself providing confining pressure by having a higher resistance to lateral deformation. The way that the materials all ultimately fail with a positive D_v value implies that at failure this ‘self-pressure’ fails and void growth can proceed uninhibited. An external confining pressure would thus add to this mechanism and increase the load a sample could bear before failure, which is exactly what is seen in the literature[36,63,92,133–135].

While confining pressure is already known to change how cracks grow and interact, our experiments in uniaxial stress showing behavior consistent with an applied external confining pressure is a new piece of confirming information for the importance of confinement to the failure mechanics of brittle materials[92,128,135], and should lead to new insights as further ways to study damage accumulation are explored.

3.7. Conclusion

This work has tracked stress, axial strain, and lateral strain independently through a combination of Digital Image Correlation, Ultra High Speed Photography, and traditional dynamic strain gauge measurements. Data was collected from two grades of alumina, silicon carbide, and a brittle cermet that were tested in a Kolsky bar. Prior models of damage were modified to track changes in apparent Poisson's ratio along with apparent stiffness. Further modification was made based on experimental evidence and past literature to allow for the possibility of 'positive' damage. This was done in order to have a method to track global changes to elastic properties in a way that would allow for microscopic behaviors such as crack growth, closure, and reorientation to be inferred. The observations showed that stiffness could increase from an initial value, and that damage accumulates more strongly in the Poisson's ratio than the stiffness for these materials. Damage accumulation in the Poisson's ratio also shows that a decreased Poisson's ratio is associated with a higher failure stress, while an increased Poisson's ratio is associated with the ultimate failure of the materials. These observations improve our ability to understand what is happening to the interior microstructure of the materials via macroscopic observations, providing new validation data for models and simulation. The observation of low Poisson's ratio being associated with increased failure strength is consistent with external confining pressures increasing failure strength.

Chapter 4 - Dynamic Mechanical Response of Damaged Alumina

4.1. Introduction

There are two distinct but related phenomena tied to the concept of damage in materials, especially for brittle ceramics. The first is physical damage, which is all of the changes to a material that physically manifest such as cracks[45,136–140], phase change [88,91,141–143], twinning[144,145], and comminution [146–150]. Post-mortem analysis[4,108,146,151,152] is often used to determine the extent of physical damage after a loading event, and under quasi-static loading, *in situ* X-ray imaging is possible[153–156]. When the material is transparent[40,41,157], or allows coherent X-rays to pass through the sample such as with single crystal materials[158], physical damage propagation can be studied under dynamic loading conditions. In contrast to physical damage, the second type of damage is what we define as mechanical damage, which is how physical damage manifests as apparent changes in mechanical properties. This can be a change in material failure strength[26,135,152,159,160], fracture toughness[67,161–164], or the speed of sounds in the material[165–169] that relate to elastic constants such as Young's modulus and Poisson's ratio. A primary distinction between physical and mechanical damage is in how they are measured, in that physical damage is present regardless of loading and typically characterized via imaging, while mechanical loading is required to characterize mechanical damage. Due to the fact that physical damage causes mechanical damage, can be measured directly, and does not need a load to be applied, it is desirable to be able to derive mechanical damage behavior from observed physical damage in order to predict how materials will react to loading. Past models have predicted the macroscopic response of brittle materials by taking into account the effects of a single crack [45,56,136,170] or the interaction of multiple cracks[55,101,137,138,171], but only using the initial flaw population, which is a measure of physical damage, and has had as model inputs has had limited success in simulating the mechanical damage observed in experiments[103,172]. More research into the relationship between physical and mechanical damage is needed.

In brittle materials, physical damage is considered an irreversible process, as once a crack is present, the crack faces will not fuse together again[45,56,136,137,170]. However, physical damage does not translate to mechanical damage linearly or even monotonically[1,173,174]. For example, in the study of quasi-brittle rocks associated with seismic faults by Aben *et al.*[173], there was a region where pulverized rock demonstrated higher wave speeds, and thus higher elastic moduli, than less damaged rocks that were merely fractured. In another study, Shea and Hanson[1] showed that wave speeds in coal samples under compression did not demonstrate linear or monotonic change during the failure process. Building upon previous work with brittle materials under quasi-static and dynamic loading, Koch *et al.*[175] used ultra-high-speed (UHS) photography and digital image correlation (DIC) in conjunction with a Kolsky bar apparatus as outlined by Lo *et al.*[60] to study mechanical damage accumulation in advanced ceramics (e.g., silicon carbide, aluminum oxide, boron carbide) under dynamic loading conditions. Key results of that study were[175] that changes to the apparent Poisson's ratio were more indicative of damage than changes to Young's modulus, and that both forms of mechanical damage were nonlinear and non-monotonic with respect to strain. The apparent Young's modulus was observed to increase above pristine quasi-static values just before failure in many of the tests, which stands in contrast to prior models that assume that physical damage can only manifest as a decrease in apparent Young's modulus[36,55,134,176]. Based on prior models[55,56,101] and experiments[1,102,159], this apparent increase in Young's modulus was hypothesized to be caused by the closure of pre-existing cracks with crack faces normal to the loading direction. Crack-closure explains the apparent increase in stiffness by requiring a reduction in apparent Poisson's ratio due to material moving axially into the void space instead of expanding laterally outward. This pore-collapse-type behavior has been seen in *in situ* scans of concrete under triaxial compression[102] and in scanning electron microscope images of rocks under uniaxial compression[140]. From scanning electron microscopy and X-ray tomography by Lo *et al.* [60], Li *et al*.[110], and Amirian *et al*.[111], the scale of these voids in pristine materials are on the order of micrometers, reducing the extent to which crack closure behavior can manifest before material failure.

Building on these past works to understand both how physical damage arises and evolves in brittle materials and how mechanical damage manifests in brittle materials under various loading conditions, this paper explores the effects of physical damage on mechanical damage evolution. This paper uses thermal shock to induce internal cracking in samples as described by Lo *et* *al.*[177] and extends the use of mechanical damage analysis[175] to these already damaged materials. By introducing large internal cracks without fully fragmenting the material before loading, the crack closure phenomenon seen in non-ceramic brittle materials[1,61,102,140,159,170,171,173,174] can be studied within the context of advanced ceramics under uniaxial compression. In addition, this study also explores the use of the shear modulus change as a method of explaining observed mechanical damage accumulation, as compressive loads need to be translated into local tensile[48,104,121,178] or shear loading[101,148–150,179–181] in order to result in physical damage. This paper thus investigates the complexities of damage accumulation under uniaxial compression, and using analytic methods in order to present how physical damage relates to the evolution of apparent mechanical damage evolution.

4.2. Experimental Setup & Methods

Material behaviors in this investigation are studied within a context of uniaxial compression, using samples machined into cuboids of dimensions of 3.5 mm x 2.7 mm x 2.3 mm. These sample sizes were used in both quasi-static and dynamic testing and were chosen to conform with prior samples[108], but reduced in dimensions in order to produce higher pressures with less force used, particularly in Kolsky bar experiments. The material of interest in this study was AD995 alumina from CoorsTek, Inc., with the "995" portion of the name referring to the fact that the material is 99.5% aluminum oxide by mass, with the remaining 0.5% being silicon dioxide. AD995 was selected for use because of its ease of acquisition and for being a representative material used in armor and industry[39,162,165,181–183]. Additionally, it has been used in previous papers by the authors of this study[109,175], providing a commonality of data. The previously gathered data[109] showed that AD995 had average grain sizes of 8.0 ± 3.0 µm, minimal internal void spaces, and the silica is located at the grain boundaries as part of the interstitial material rather than present as large defects or incorporated into the grains. AD995 is, thus, almost entirely homogenous, and the only source of difference in material properties from another alumina of equal chemical purity would be from grain sizes. Temperatures of 1300°C are considered 'low' for sintering high purity alumina[184] and, thus, keeping the thermal shock temperature well below this level means that the only microstructural changes will come from the thermal shock, and not grain growth or recrystallization. Where materials such as boron carbide have graphitic inclusions[108] and additives can produce complex phase structures[66,67,143,185,186], AD995 is not known to have any of these complexities.

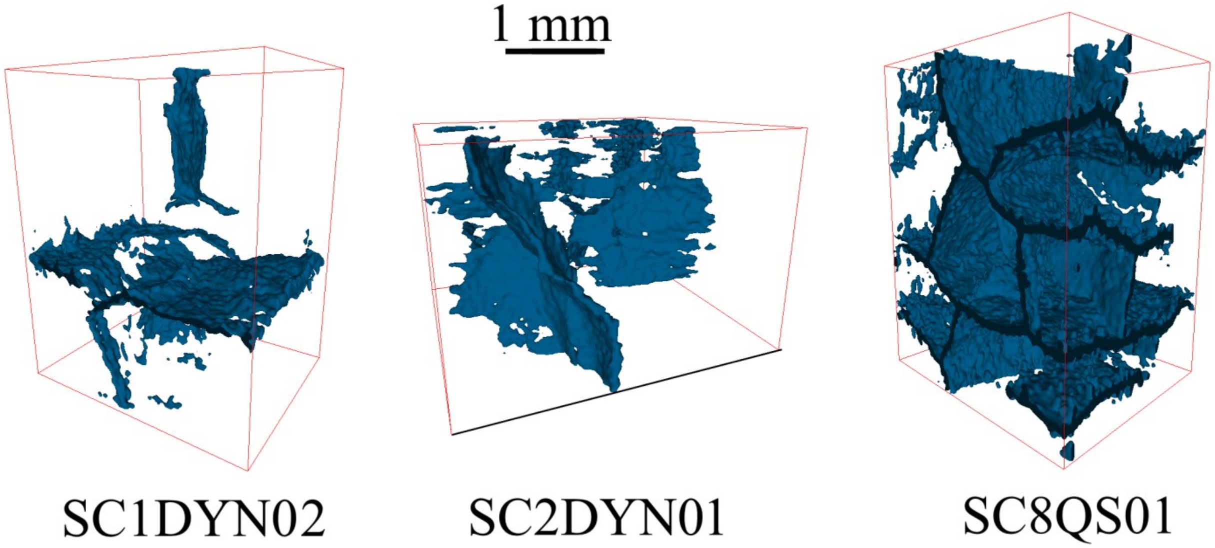

Figure 4-1– Internal crack reconstructions from X-ray computed tomography for SC1DYN02, SC2DYN01, and SC8QS01 from Lo *et al.*[60] showing the relative evolution of internal cracks. White space is not the absence of cracks but regions where any cracks present are too diffuse to be present in the reconstruction.

To produce internal cracks and damage in the alumina, the ceramic samples were thermally shocked in preparation for testing by heating them with a butane torch for 120 seconds and then visually checking for uniform thermal glow, and heating for an additional 30 seconds if glow was not uniform and repeating the inspection. By this method the samples were heated until above 750 °C. Thermal shock is then achieved by quenching the sample in room temperature water, causing the exterior of the sample to rapidly drop. This rapid temperature change is capable of causing the formation of internal cracks that have been shown to lead to mechanical damage in ceramics[187]. Previous studies focusing on the behavior of pre-damaged materials have primarily been interested in geomaterials[1,103,173,174] or concrete[102,159] damaged by mechanical forces. Testing of pre-damaged advanced ceramics has usually been limited to repeated loadings under dynamic conditions[127,188] or studying already comminuted powders[189], but Krimsky *et al.*[190] have used thermal shocking on boron carbide. In Krimsky *et al.*[190], the pre-damaged samples were subjected to one or two cycles of heating and quenching, and then characterized with X-ray computed tomography to determine crack surface area. The thermal shock method is preferred for this study because the degree of damage can be controlled by subjecting the samples to repeated heating and shocking cycles, with each sample in this study being subjected to between 1 and 8 cycles to produce a variety of damaged states. If a sample exhibited external physical damage such as surface delamination or loss of integrity, it was excluded from further testing. X-ray computed tomography was used by *Lo et al.* [60] to confirm the presence of internal cracks, with Figure 4-1 showing reconstructions of these internal cracks for three samples subjected to one, two, and eight thermal shock cycles. From Figure 4-1 it can be seen that one shock cycle produces physical damage, and eight shock cycles produces significantly more physical damage than one cycle. The difference between one and two shock cycles is, however, not as great as between zero and one or one and eight cycles, and thus the number of shock cycles should be taken as a qualitative measure of physical damage. As a result of the complexity of crack size, orientation, and their interactions with respect to loading direction, the number of shock cycles and the amount of physical damage present remains a qualitative measure for this study. Information on the number of cycles applied to each sample and the resulting peak compressive failure stress and failure strains found during testing are shown in Table 4-1. Samples are labelled according to the number of shock cycles (SC) they went through, whether they were subjected to quasi-static (QS) or dynamic (DYN) loading, and what sequence in a series of similar conditions they were subjected to. For example, SC0QS01 is the first quasi-static sample subjected to no shock cycles (i.e. pristine), while SC4DYN02 is the second dynamic sample subjected to four shock cycles. The mechanical response of pristine dynamic samples have been previously described in Koch *et al.*[175], and four quasi-static pristine tests are included in this study for completeness. In addition, a quasi-static baseline derived from manufacturer specifications is included in many of the figures demonstrating mechanical property measurements, and this serves to show the behavior that would be expected in a purely brittle elastic response.

In these studies, the quasi-static compressive strength and Young's modulus were independently examined using an MTS 810 materials testing machine that compressed samples to failure. The servo-hydraulic controls allowed for precise measurement of forces, and Digital Image Correlation (DIC) was used to determine axial and lateral strains. The DIC setup is discussed in a subsequent paragraph. A Promon U750 camera recording at 100 Hz were used to capture the entirety of a 30 to 50-second-long quasi-static experiment. While the framerate was sufficient to capture axial and lateral strain data that could be used to calculate Young's modulus and

Poisson's ratio values, 100 Hz is insufficient to capture the behavior of samples during actual failure (i.e. post-peak stress), as the events occur too quickly. For pristine samples, this yields no additional data beyond verification of manufacturer values. These mechanical values are a Young's modulus of 370 GPa, a Poisson's ratio of 0.22, and a failure strength of 2.70 GPa[112]. The quasi-static values of Young's modulus and Poisson's ratio are used as the pristine values when determining damage later. For the damaged samples subjected to quasi-static testing, their stress-strain and lateral vs. axial responses are non-linear and of interest to this study in seeking to understand relationships between physical (pre-cracking) and mechanical damage (Young's modulus and Poisson's ratio evolution).

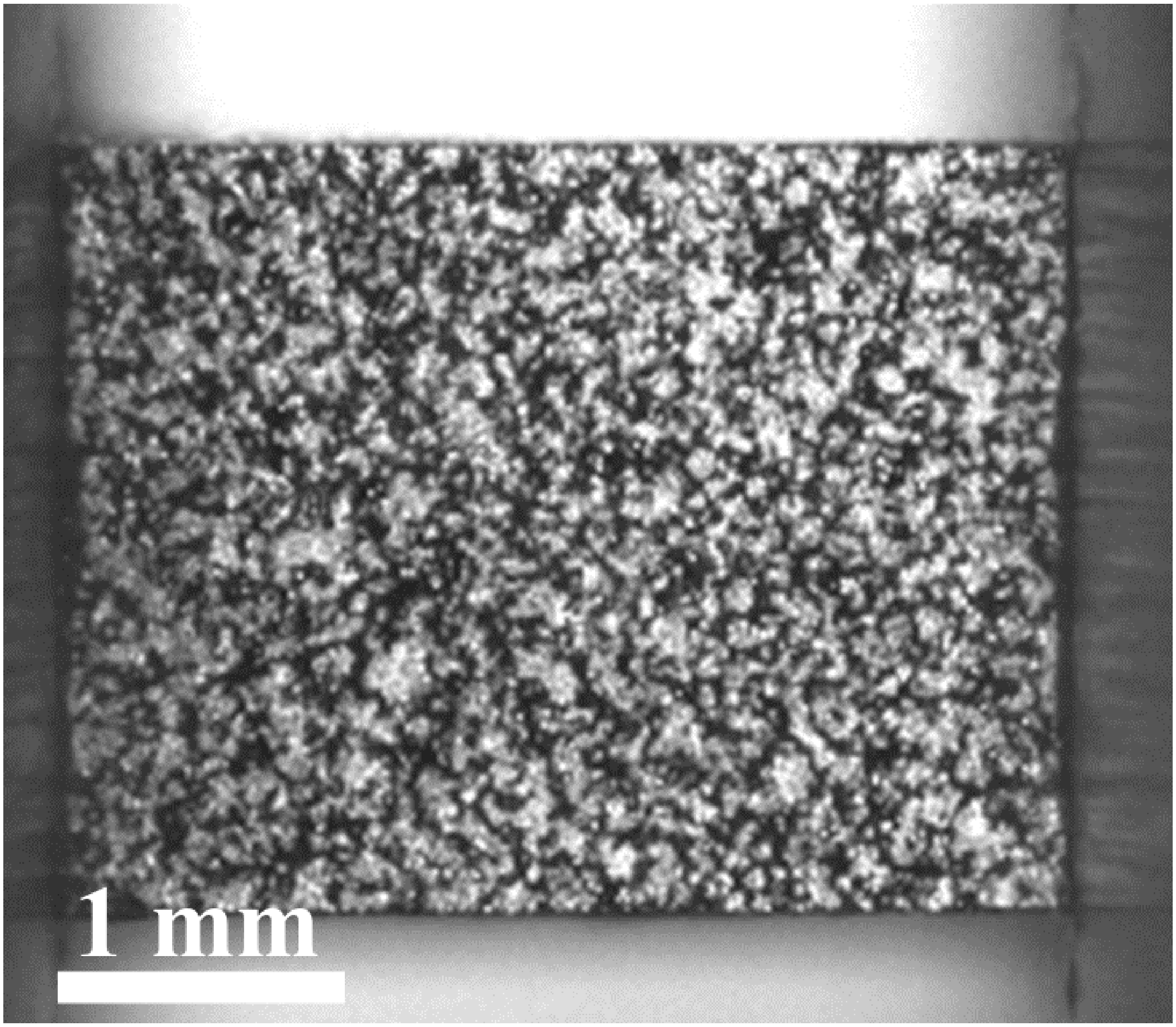

Figure 4-2 –An example of an AD995 sample sprayed with a speckle pattern for DIC purposes held between the incident and transmitted bars of the Kolsky bar. The field of view in the vertical direction has been cropped in order to better show the features of the sample.

Dynamic testing was done using a Kolsky bar testing apparatus and an ultra-high-speed Shimadzu HPV-X2 camera capable of capturing at ten million frames per second and 400 x 250 pixel resolution. For the experiments performed here, a framerate of 500,000 to 2,000,000 frames per second (FPS) was used at full resolution, and the camera system was coupled with a K2 Infinity Lens to fill the sample in the 4 mm by 6.5 mm field of view of the camera, with an example of such an image seen in Figure 4-2. The Kolsky bar apparatus used incident and transmitted bars that were 12.7 mm in diameter and made of maraging steel (Service Steel America C-350) with a Young's modulus of 200 GPa, Poisson's ratio of 0.29, yield strength of 2.68 GPa, and a density of 8100 kg/m^3. The incident bar was 101.6 cm in length, while the transmitted bar was 91.4 cm in length. Using compressed gas to provide the impulse, a projectile made from maraging steel was launched into an incident bar, which produces a strain pulse from the impact. The strain pulse is the transmitted into a ceramic sample held between the incident and transmission bars. The strain signal received by the transmission bar corresponds to the strain received by the sample while it was intact and remained in contact with both bars. In order to protect the incident and transmission bars from damage by the harder ceramic samples, 5 mm thick and 7.94 mm diameter tungsten carbide platens jacketed in 12.7 mm outer diameter titanium rings were used. High pressure grease was applied at the platen-sample interfaces in order to reduce the transmission of lateral or shear strains from the bars into the samples and to ensure that the input pulse was as uniaxial as possible. This setup is consistent with others in the literature, as noted by round robin testing performed under the supervision of Swab and Quinn[114]. A near-triangular pulse is considered ideal in Kolsky bar experiments for brittle materials[61,71], and this was achieved by using a 3.175 mm diameter and 1 mm thick tin pulse shaper, with a final strain rate on the order of 10^1 to 10^2 s^{-1} occurring over a pulse length of 200 μs. These pulse durations are much longer than typically used in the literature of 50 to 100 μs rise times[61,71], but have allowed us to achieve good stress equilibrium[175] and measurements[60] for the purpose of our current study. As a demonstration of equilibrium in the experiments in this paper, Figure 4-3 shows axial strain vs. time and stress vs. time simultaneously for SC0DYN02. Axial strains are shown for both the entire area of interest and for sub-sections of the sample surface (right in Figure 4-3), which shows that the strain field is uniform and the stress follows the strain, showing uniform deformation and good equilibrium. This methodology has previously been described and validated by Lo *et al.*[177] and Koch *et* *al.*[175]. In the experiments, strain was measured by six strain gauges arranged in three pairs, with two pairs on the incident bar, and one pair on the transmitted bar. Each pair had an additional two gauges not connected to the bars but connected together to form a full wheatstone bridge, with each bridge connected to its own Vishay 2310b amplifier, which sent their signals to an HBM Gen3i high speed portable data acquisition system sampling at 2 million samples per second. The strain gauge types were Micro-Measurements CEA-06-250UN-350 350 ohm resistance gauges secured in place via cyanoacrylate adhesive. Tests were only considered successful when strain responses and camera images confirmed that samples failed in loading on the first loading pulse through the material. This setup has been used previously in Koch *et al.* [191]and Lo *et al*.[192] and has been established as part of the state-of-the-art in ceramics Kolsky bar round robin supervised testing by Swab and Quinn[114].

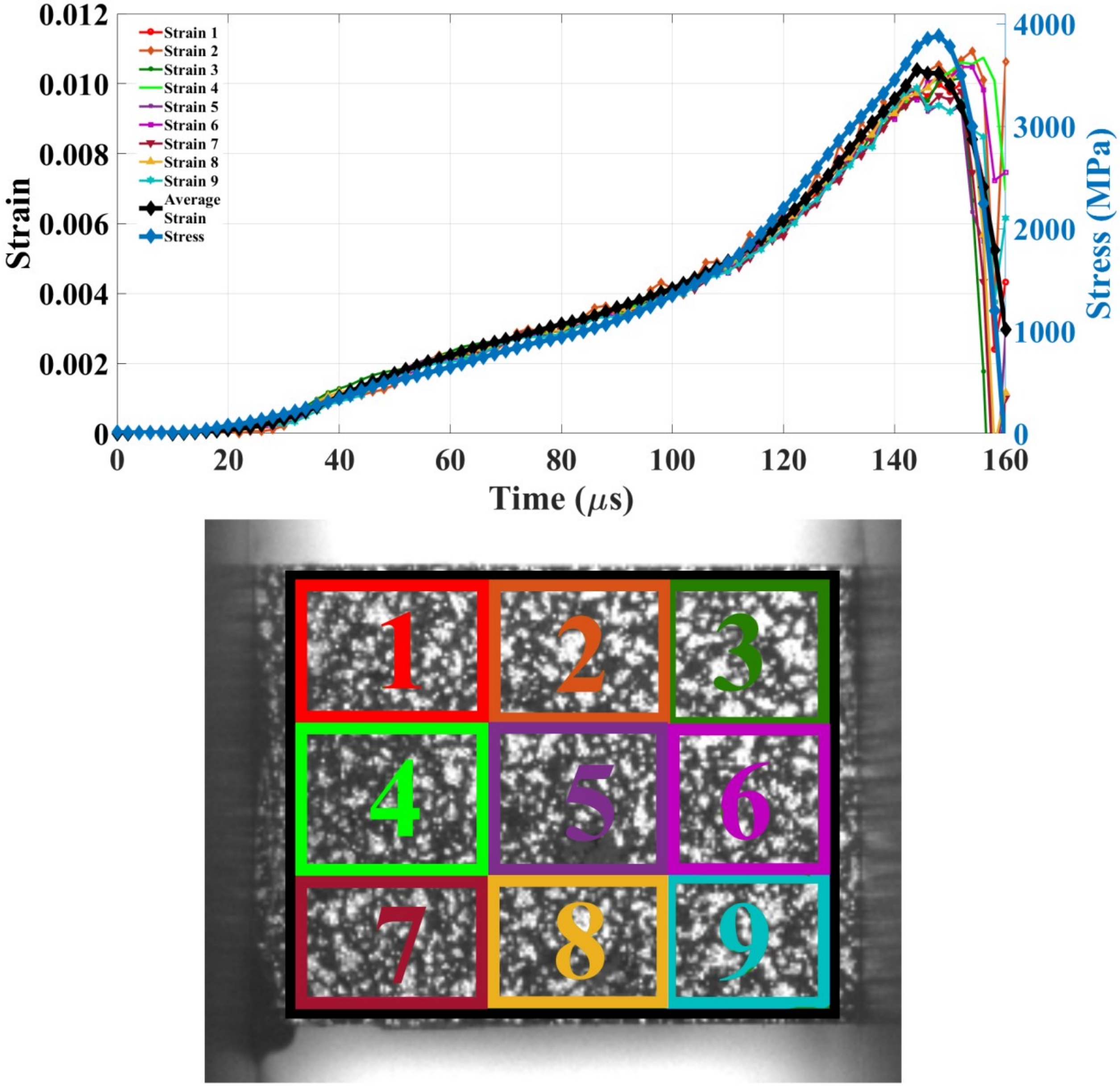

Figure 4-3 – Combined strain vs. time and stress vs. time plot for SC0DYN02 on the left, and the sample showing the various DIC regions of interest on the right. The average strain vs. time response and the stress vs. time response follow each other and the individual strain responses are not strongly affected by the region, showing that the sample is experiencing good equilibrium.

Digital image correlation techniques were applied to camera images from the quasi-static and dynamic tests in order to obtain lateral and axial strain measurements of the samples. DIC is a computer vision method used to track changes in the position of speckle patterns on the surface of an object in order to compute deformation fields, and has been well established in the study of many different materials[118–122]. DIC has been used previously in Kolsky bar experiments by the authors [110,111,175,177,192]. Due to the small size of the samples in our study, special measures were required to produce a speckle pattern that would produce more accurate measurements and lower error in correlation, requiring use of an airbrush with a 0.15 mm nozzle in order to produce speckles (speckles are seen in Figure 4-2) which corresponds to speckle areas of approximately 1300 to 2600 μm^2. Due to the high speed of image capture and thus low exposure times (~200 ns), a high gloss metallic paint for the speckles and high intensity LED ring light (REL Inc.) were required in this study to produce sufficient contrast in the images. DIC analysis was done using the commercial VIC-2D (v6 2018) software from Correlated Solutions (Irmo, South Carolina, USA), with the regions of interest discretized into 27 by 27 pixel subsets with a step size of 7 pixels. Correlation analysis was carried out using the optimized 8-tap interpolation scheme, with the shape function being internal to the software but based on derivatives of displacements and using a zero-normalized sum of squared differences criterion. Pre-filtering of images was done with a low-pass filter, while subset weighting was done via a Gaussian weighting, with no additional post-processing smoothing. Overall confidence intervals for correlations were consistently within the range of 10^{-3} to 10^{-4} pixels, leading to measurement uncertainty arising primarily from equipment and taken to be no greater than a conservatively large 5% in total. The largest possible source of uncertainty was the initial size of the samples in the visual field, taken as being 0.1 mm out of the 2.7 mm side length of the 2.7 mm by 3.5 mm face used for measurement, which amounts to ~4% uncertainty. Strains were computed from the displacement fields using the engineering strain tensor in the DIC software. The computed strain histories were matched to the stress histories produced by strain gauges on the Kolsky bar to determine stress-strain curves for each of the experiments, as is commonly done in Kolsky bar experiments in the literature[61,117,193]. This produces stress-strain plots that do not need to assume material properties of the sample. As a result of stiffness not being assumed as constant and axial and lateral strains being independently measured, variations in the Young's modulus and Poisson's ratio response can be tracked with time and strain, allowing us to track mechanical damage evolution in these properties.

4.3. Damage Quantification

With the experimental capacity to determine axial and lateral strain and stress all independently from each other, it becomes possible to measure apparent elastic properties such as Young's modulus and Poisson's ratio, and to examine how these properties deviate from linearity during loading. This study is focused on the deviation from linear elastic behavior, so normalizing the values against pristine values better illustrates change than simply plotting the apparent elastic response values. This normalization process also allows simpler comparisons between materials with different intrinsic properties, and the normalization produces values that can be compared to those predicted from previous models on damage accumulation in brittle materials[55,171,194]. With access to both Young's modulus and Poisson's ratio from the measurements of stress, and axial and lateral strain, Young's modulus and Poisson's ratio can each have their own damage term that accounts for how these properties evolve during loading, and these values can vary independently of one another mathematically. The values of Young's modulus and Poisson's ratio are not independent from each other in a physical sense, as the mechanical damage arises from physical phenomena that affect both properties simultaneously. It is through the interaction of mechanical damage for Young's modulus and Poisson's ratio that a more complete understanding of the underlying physical damage evolution can be determined. A more detailed derivation of the calculation of damage values is found in Koch *et al.*[175], where the important mechanical damage terms to the Young's modulus and Poisson's ratio being denoted as D_E and D_ν, respectively. From experiments performed in this paper, these values are calculated using Equations (4-1) and (4-2):

$$D_E = \frac{E_{app}}{E_0} - 1 \tag{4-1}$$

$$D_\nu = \frac{\nu_{app}}{\nu_0} - 1 \tag{4-2}$$

where E_0 and ν_0 are the pristine Young's modulus and Poisson's ratios determined from the quasi-static experiments, respectively, and E_{app} and ν_{app} are the apparent Young's modulus and

Poisson's ratio at each data point in a given experiment, respectively. The apparent elastic properties are calculated using Equations (4-3) and (4-4):

$$E_{app} = \frac{\sigma_{inst}}{\varepsilon_{x_{inst}}} \tag{4-3}$$

$$\nu_{app} = \frac{\varepsilon_{y_{inst}}}{\varepsilon_{x_{inst}}} \tag{4-4}$$

where σ_{inst} is the instantaneous stress, $\varepsilon_{x_{inst}}$ is the instantaneous axial strain, and $\varepsilon_{y_{inst}}$ is the instantaneous lateral strain, with "instantaneous" here referring to each individual stress-strain or lateral-axial strain data point collected for a given experiment. For these experiments, each DIC image paired with time-matched load data from the strain gauges represents a three-component data point that allows for E_{app} and ν_{app} to be calculated for a given strain, which can then be used to calculate D_E and D_ν for a given strain or time. In the discussion of the results probing the response of the undamaged and pre-damaged samples, the primary interest will be in damage accumulation with axial strain.

Investigating damage in the form of Equations (4-1) and (4-2) is also motivated by experimental data[60,110,175] where both D_E and D_ν varying simultaneously suggest phenomena such as crack closure that are not apparent when only analyzing one damage value at a time. Fortunately, there are elastic moduli that combine together Young's modulus and Poisson's ratio in their description, such as the shear and bulk modulus; tracking these are also of interest here to explain observed phenomena. For an isotropic linear elastic material, the shear modulus (*G*) is calculated from Young's modulus and Poisson's ratio by:

$$G = \frac{E}{2(1+\nu)} \tag{4-5}$$

The same process used by Koch *et al.*[175] to generate Equations (4-1) and (4-2) are used here to generate Equation (4-6), which gives the apparent shear modulus G_{app}:

$$G_{app} = \frac{E_{app}}{2(1+\nu_{app})} \tag{4-6}$$

with the apparent shear modulus calculated by the apparent E_{app} and ν_{app} produced by Equations (4-3) and (4-4), and the pristine shear modulus G_0 calculated through the insertion of the values of E_0 and ν_0 into Equation (4-5). With G_0 and G_{app} so calculated, the shear damage D_G can be calculated using Equation (4-7):

$$D_G = \frac{G_{app}}{G_0} - 1 \tag{4-7}$$

In these equations, D_E and D_ν are calculated from a single apparent elastic modulus each and are thus considered primary damage responses, while D_G is determined from two apparent elastic moduli and is, thus, viewed as a secondary damage measure. The calculation of D_G from Equation (7) serves as a complement to understanding D_E and D_ν together. Next, experimental results are discussed in three stages: direct experimental results, primary damage response, and secondary damage response. Each stage serves to expand upon the insights of prior stages to better understand how intact and physically damaged advanced ceramics behave during mechanical loading.

4.4. Results

4.4.1. Mechanical Properties

The stress-strain data curves for the twenty tests examined are seen in Figure 4-4, with the sample names described in Table 4-1. The legend in the figure denotes that the color of the curves are associated with the level of shock cycles (e.g., SC1 being 1 shock cycle), with repeated experiments denoted at the end of the label as 01, 02, etc. In Figure 4-4(a), the curves are plotted for all experiments and all levels of damage. In Figure 4-4(b) to 3(d), the stress-strain curves are sub-divided according to levels of damage and this helps with visualization when specific tests are discussed here. In all sub-figures, a straight red line is included to denote the mean quasi-static behavior of the alumina AD995 material, which serves as a reference for understanding the effect of damage on the stress-strain responses for both quasi-static and dynamic conditions. For the experiments on the intact (undamaged) samples, the average strength for the quasi-static tests are 2.5±0.2 GPa and for the dynamic experiments are 3.9±0.1 GPa. The stiffness is 360±10 GPa for both, and the failure strain is 0.0068±0.004 for quasi-static and 0.0102±0.0002 for dynamic experiments. From Figure 4-4, the trend for the pre-damaged samples typically begin with an apparent Young's modulus 10-20% below pristine (290-325 GPa). The stress-strain curves then inflect after a certain level of axial strain, with the axial strain required for inflection generally being between 0.001 and 0.004 strain. The samples subjected to the most shock cycles have the highest inflection strains, but more shock cycles do not translate into a larger strain at the inflection point. The quasi-static tests all fail catastrophically at peak stress and no strain information is collected for post-peak collapse due to framerate and triggering challenges for the camera for quasi-static testing. In the dynamic samples, some post-peak strain behavior is captured, which forms discussions later. Generally, from Figure 4-4, the failure strains increase as they become more pre-damaged. For the pre-damaged dynamic experiments, the peak strength of the damaged samples is reduced to 3.0±0.4 GPa, and also generally decreases as a function of pre-damage. For the quasi-static experiments, the pre-damaged tests mostly have lower strengths than the intact tests, with exception to SC8QS01. Unfortunately, beyond 8 shock cycles, the specimen macroscale integrity becomes unstable, and the samples cannot be reliably handled before suffering external damage that renders them unsuitable for testing, and so we were unable to investigate higher shock cycle trends with the thermal shock approach. In the quasi-static tests, trends in strength as a function of pre-damage are complicated as the failure strength appears to increase as a function of shock cycles for quasi-static loading, which is, perhaps, counter-intuitive. This will be discussed later in the Discussion section. Lastly, noticeable are some interesting behaviors in Figure 4-4: 1. sample SC3DYN02 has a steeper stress-strain slope, which indicates a higher Young's modulus, and additionally SC3DYN02 has a lower failure strain than all other samples; and, 2. samples SC8DYN01 and SC8QS01 show a convergence of behavior near failure. Both show an increase in failure strain over pristine samples and both have high inflection points, with SC8DYN01 inflecting at 0.0033 strain and SC8QS01 inflecting at 0.0051 strain. These samples were motivators for investigating damage accumulation in the shear modulus as it will be shown later in the Discussion Section to provide an explanation for the behavior observed in these and other tests.

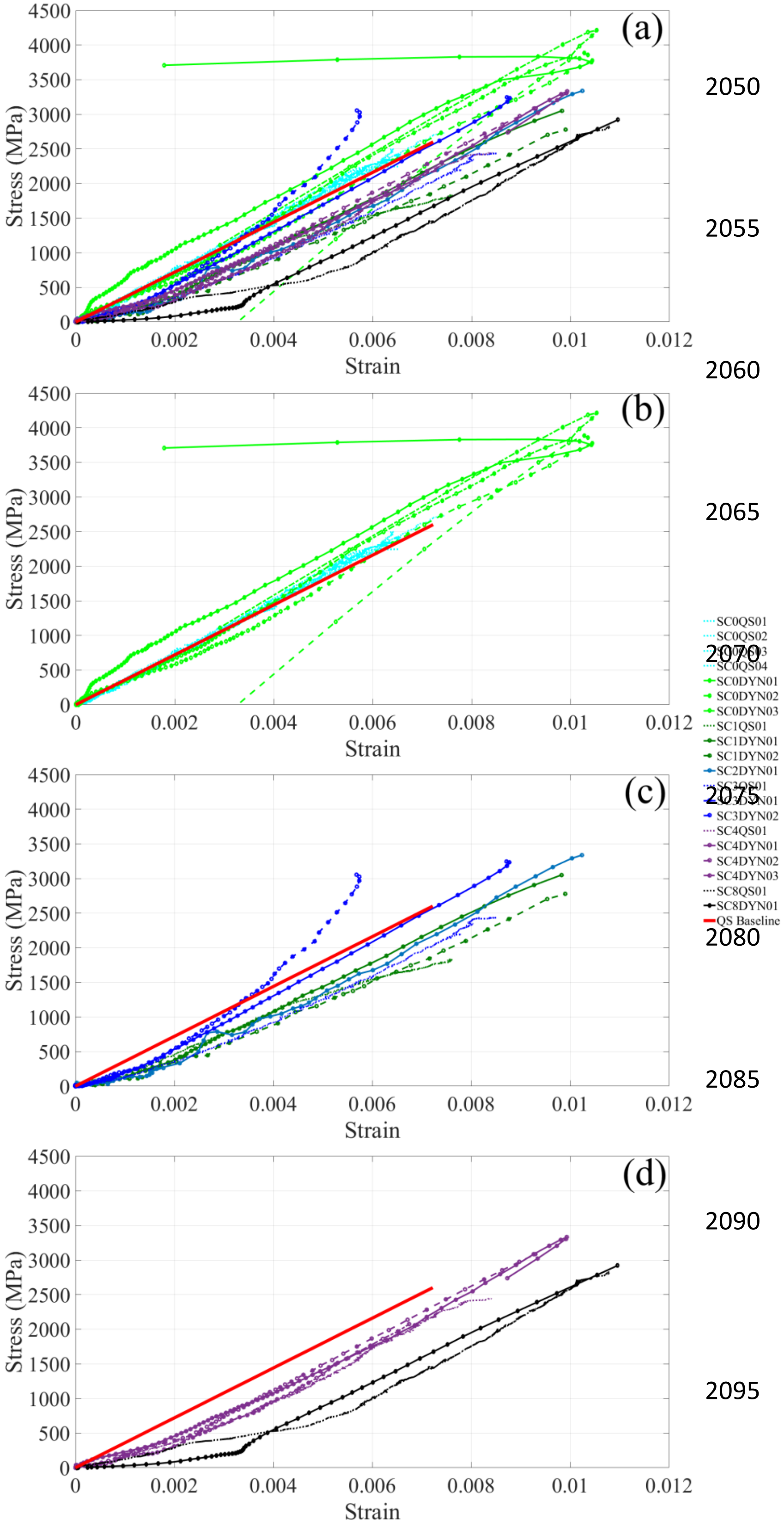

Figure 4-4 – Stress-strain curves for the various samples tested, showing the variation in early behavior and the eventual convergence towards parallel similar slopes after an initial lower value for damaged samples. Panel (a) shows all tests, panel (b) shows only the tests where no thermal shock cycles were applied, panel (c) has the samples subjected to between 1 and 3 shock cycles, and panel (d) has the samples subjected to 4 and 8 shock cycles. In addition to pristine quasi-static samples, a red line has been added to all sub-figures showing the expected linear elastic behavior based on numerous tests and manufacturer specifications. The three intact dynamic samples show the highest failure stress, as would be expected, but the most damaged samples of SC8QS01 and SC8DYN01 have the highest failure strain, which likely relates to the fact that they had the greatest strain before their slopes became parallel to the rest of the samples. The quasi-static samples all have lower failure strengths and failure strains than the intact samples, but as the number of thermal shock cycles increases the quasi-static samples show an increasing trend in failure strengths and strains. Finally, while the damaged samples fail completely at peak stress and strain, the pristine samples have unloading sections where stress and strain decrease.

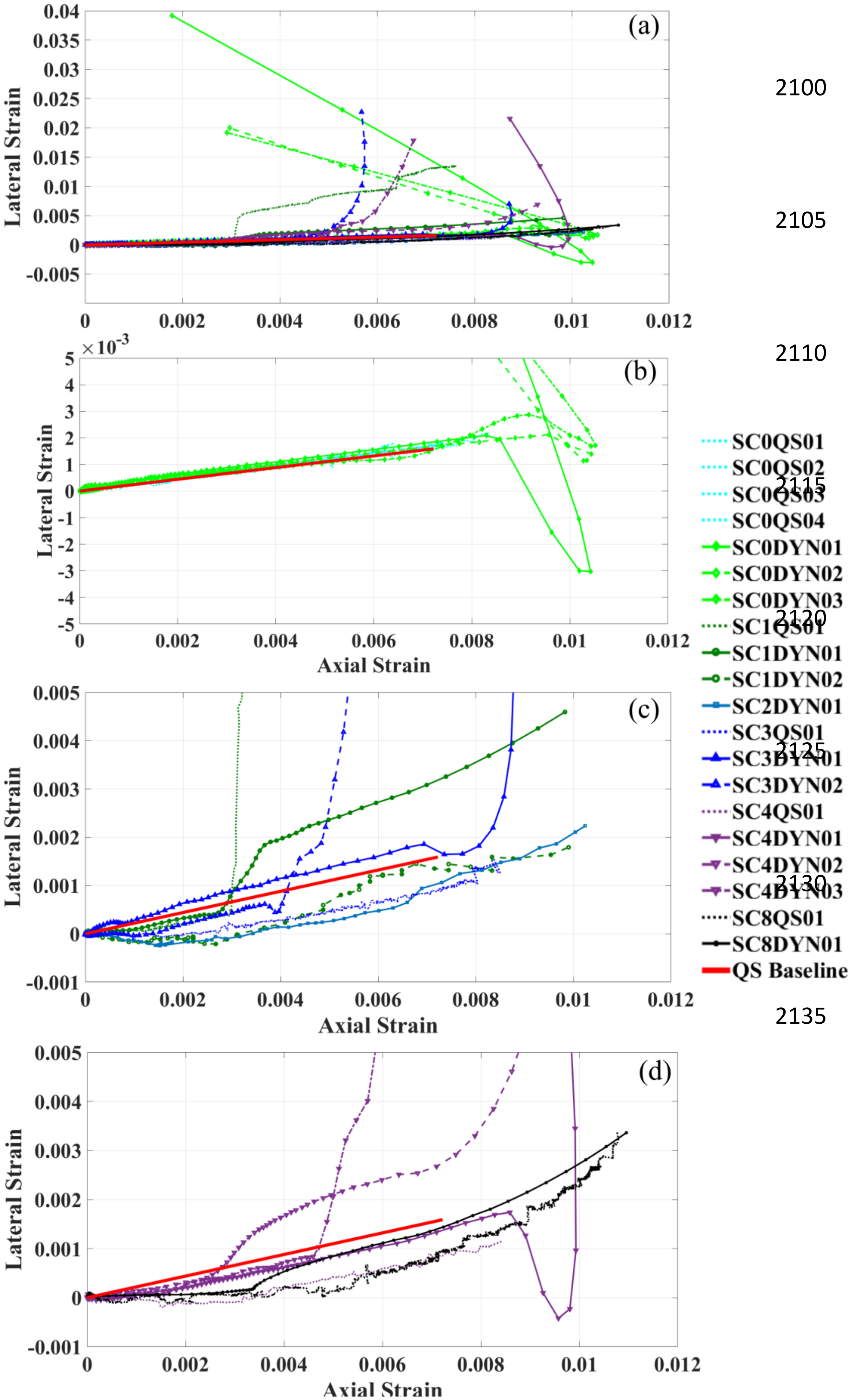

Figure 4-5 – Lateral vs. axial strain curves for the various samples tested, showing the variation in the ratio between the two strains. Panel (a) shows all tests, panel (b) shows only the tests where no thermal shock cycles were applied, panel (c) has the samples subjected to between 1 and 3 shock cycles, and panel (d) has the samples subjected to 4 and 8 shock cycles. In addition to pristine quasi-static samples, a red line has been added to all sub-figures showing the expected linear elastic behavior based on numerous tests and manufacturer specifications. Highly damaged samples abruptly fail, while the less damaged samples show large increases in lateral strain before failure. The pristine samples, SC4DYN01 and SC3DYN02 on the other hand show unloading behavior alongside these large increases in lateral strain.

Next, we show the corresponding lateral vs. axial strain relationships for all intact and pre-damaged tests in Figure 4-5. Again, the figure is sub-divided based on pre-damage levels for improved visualization and a legend is included where color notes the level of shock. The baseline quasi-static behavior (red line) is also shown in each sub-figure for reference on the effect of damage on the lateral vs. axial strain relationships. Note the y limits for sub-figures (b) to (d) are magnified from (a) in order to show more distinct trends, with asymptotic behavior for each experiment still clear in (a). For the intact experiments, the slope (or Poisson's ratio) of the lateral vs. axial strain is 0.22±0.01 for the quasi-static experiments and 0.29±0.08 for the dynamic experiments, and this is consistent with the manufacture's value of 0.22. For all pre-damaged samples across both rates in Figure 4-5, there is a region of non-increasing lateral strain for increasing axial strain at lower axial strains, followed by a mostly linearly increasing region for lateral strain as a function of axial strain. The inflection point does not strongly associate with the number of shock cycles. The non-increasing region is likely related to void collapse and crack closure, which will be discussed later in the Discussion Section. The rate of increase for lateral vs. axial strain behaviors of curves do not follow any clear trends in this plotting convention as a function of pre-damage or strain rate, nor do the inflection points. Trends become more apparent later when investigating these behaviors with respect to changes in shear modulus in Figure 4-9 and Figure 4-10. Dynamic tests generally show a larger lateral response than quasi-static tests of the same pre-damage level, with the exception of SC1QS01 having a greater lateral response than SC1DYN01 or SC1DYN02. The number of shock cycles does not seem to follow a significant trend in terms of average lateral strain at failure, with SC0 > SC4 > SC3 > SC1 > SC8 > SC2. The greatest lateral response tends to come during unloading for dynamic tests, but SC1QS01 demonstrates a series of abrupt jumps in lateral response during loading. These large lateral responses during unloading imply that internal cracks are growing internally and require additional volume to accommodate their growth and thus must expand laterally to do so. This unloading behavior is most extreme in SC0DYN01, where during unloading the strains measured by DIC become out of sync with the stresses measured by the strain gauges. This is seen in Figure 4-4 as the stress remaining near constant while the strain rapidly decreases. While non-physical in nature, what this result tells us is that the lateral expansion of the cracks is causing out-of-plane movement that the DIC is interpreting in part as a decrease in axial strain. This is supported by SC0DYN01 showing extreme lateral strain increase in Figure 4-5. The equilibrium seen in Figure 4-3 and the pristine quasi-static values conforming to manufacturer specifications indicate that our methodology is accurate up to failure (near peak stress). After failure the measurements are considered qualitative, as such post-peak behaviors are not well known in the literature for advanced ceramics due to the short time span (>10μs) they occur over.

The data taken from experiments to this point show a number of trends with physical damage (e.g., failure strain increasing with number of shock cycles), but also a number of anomalous behaviors (e.g., failure strength increasing with the number of shock cycles for quasi-static loading). The primary inferences that can be drawn from Figure 4-4 and Figure 4-5 on their own is that the relationship between physical damage and mechanical response is non-linear and non-monotonic. This is known to occur in geomaterials[1,173,174], but in those studies the degree of physical pre-damage was not as controlled. Further analysis of the material requires shifting from examining the stress-strain and lateral vs. axial curves to examining the primary mechanical damage values of D_E and D_ν. The most interesting features of these tests are associated with low stress-strain or lateral-axial responses that are not clearly observed in Figure 4-4 and Figure 4-5.

4.4.2. Damage Accumulation

The primary damage variables D_E and D_ν are calculated from the stress σ_{inst}, axial strain $\varepsilon_{x_{inst}}$, and lateral strain $\varepsilon_{y_{inst}}$, using Equations (3) and (4), respectively. The plotting of D_E vs. axial strain is shown in Figure 4-6, and the plot of D_ν vs. axial strain is shown in Figure 4-7. The same legend and sub-plotting scheme from Figure 4-4 and Figure 4-5 are used in Figure 4-6 and Figure 4-7. The red line corresponding to the expected quasi-static behavior is also shown in both Figure 4-6 and Figure 4-7, and this manifests as a horizontal line due to the fact that a purely linear elastic brittle response would demonstrate no damage of any sort up to failure. The samples in Figure 4-6 all show large negative D_E values at lower strains before an inflection occurs, and the values begin to converge towards D_E = 0, with two exceptions. The first exception is SC0DYN01, which exhibits the opposite initial behavior by exceeding the pristine Young's modulus at low axial strains, before converging to D_E = 0, and then having an increasing D_E value during unloading. The second exception to the general trend is SC3DYN02, which passes its pristine stiffness and continues to increase its apparent Young's modulus up to failure, exceeding $D_E = 0$ and having $D_E = 0.30$ at failure. In isolation, this D_E behavior is hard to reconcile with past theory which suggests that brittle materials in compression should only lose stiffness with axial strain once crack growth begins[36,55,56]. Additional insights are found via examination of D_ν and D_G in Figure 4-7 and Figure 4-10, respectively.

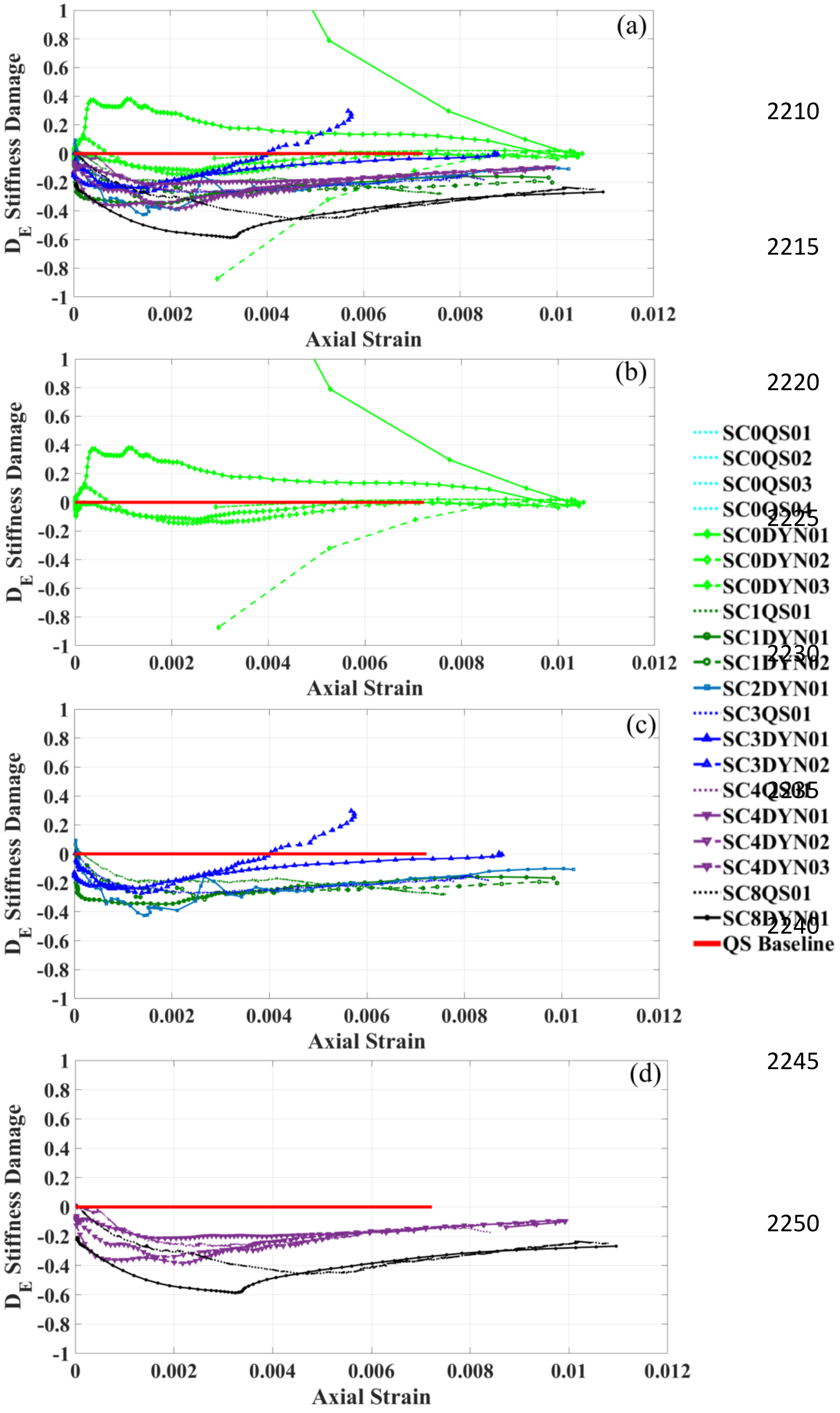

Figure 4-6 – D_E stiffness damage versus axial strain. Panel (a) shows all tests, panel (b) shows only the tests where no thermal shock cycles were applied, panel (c) has the samples subjected to between 1 and 3 shock cycles, and panel (d) has the samples subjected to 4 and 8 shock cycles. A red line has been added to all images showing the expected linear elastic behavior based expected failure strain with no damage before failure. Pristine quasi-static lines are obscured by the baseline quasi-static line, which captures their behavior. Seen is that all of the samples start with low effective stiffness before recovering towards their quasi-static pristine value ($D_E = 0$) before plateauing at some value, with the exception of SC3DYN02 and SC0DYN01, which show stiffness greater than its quasi-static value at failure. Of particular interest is the fact that this convergence towards quasi-static pristine also holds for the pristine samples, even if they begin higher than pristine such as SC0DYN01 and SC0DYN02.

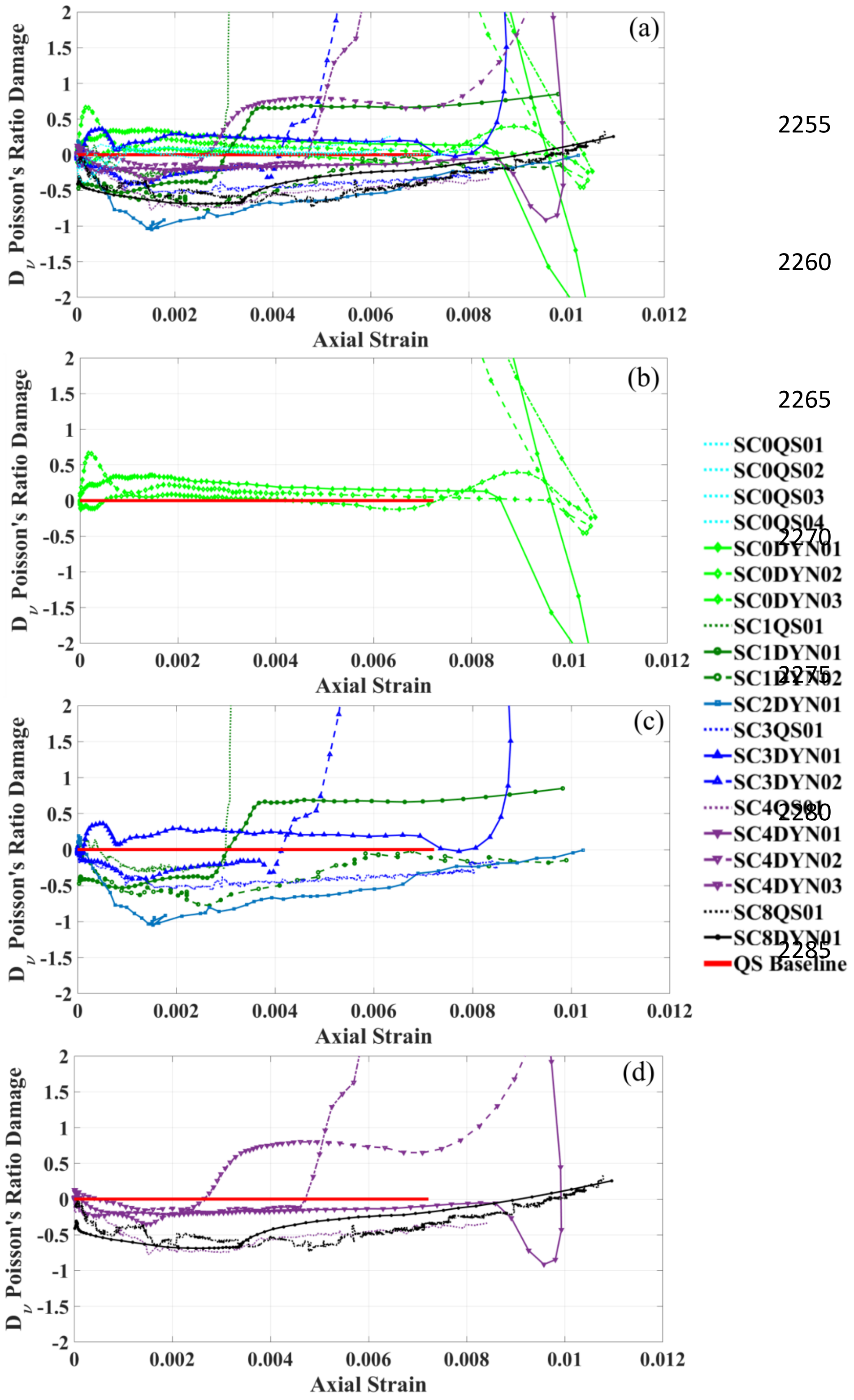

Figure 4-7 - D_{ν} Poisson's ratio damage versus axial strain. Panel (a) shows all tests, panel (b) shows only the tests where no thermal shock cycles were applied, panel (c) has the samples subjected to between 1 and 3 shock cycles, and panel (d) has the samples subjected to 4 and 8 shock cycles. A red line has been added to all images showing the expected linear elastic behavior to failure strain with no damage before failure. Pristine quasi-static lines are obscured by the baseline quasi-static line, which captures their behavior. The image shows a wide variability in the behaviors, in comparison to Figure 4-6, which shows a more consistent set of behaviors. However, as before the less damaged samples, including the pristine samples, demonstrate large increases in mechanical damage during failure.

Next, Figure 4-7 shows D_ν vs. axial strain, and reinforces the observations from Figure 4-5 in that damage does not accumulate in a consistent manner across all of the pre-damaged samples. Most of the pre-damaged samples show initial D_ν values of -0.5 or lower, and then these increase in D_ν as axial strain increases. The result of D_ν being positive at failure for the majority of the samples is the most important observation that can be drawn from these experimental observations. A positive D_ν involves the introduction of new volume to the system in order to increase Poisson's ratio above pristine, which is consistent with materials experiencing crack growth. The general description of the D_ν vs. axial strain is that the samples start with a negative D_ν, reach an inflection point, and then trend upwards. This trend of D_ν increasing before failure holds for all but SC1DYN01, as might be expected from crack closure[102,140]. However, they do not follow a consistent pattern for the number of shock cycles influencing the axial strain at which inflection occurs. The SC3DYN01, SC3DYN02, and SC4DYN01 samples that demonstrate unloading behavior with axial strain decrease also show a D_ν>1.5 at failure. Samples such as SC3DYN02 and SC4DYN01 have extreme values of D_ν at failure, being 7.6 and 12.7, respectively, which are not plotted with the other D_ν damage curves as they are so large as to obscure the primary behaviors between $-1 < D_\nu < 1$. These extreme values of D_ν are likely non-physical, but they do demonstrate how the large the lateral strains become in comparison to the axial strains, which provides information on what must be happening internally to produce such results. Additionally, all samples except SC1DYN01 demonstrate a positive D_ν at failure, indicating that their apparent Poisson's ratio has increased above the pristine quasi-static value of 0.22±0.01, which is a process that requires the introduction of new volume to the samples. Next, only SC8DYN01 has a strong inflection point in D_ν at the same strain as the strong inflection point in D_E, which is suggestive of extensive physical damage as this strong inflection suggests a change in physical processes involved in mechanical response. This observation coincides with knowledge that it has been subjected to the most thermal shock cycles of all samples and thus it is expected that it has the most physical damage. Finally, while only SC8DYN01 has a strong inflection point, its quasi-static counterpart of SC8QS01 also shows a transition from one form of behavior to another, with the mechanical damage at high axial strain following the same curve as the dynamic test with the same number of shock cycles. This convergence of behavior suggests a possible convergence of mechanical behavior between quasi-static and dynamic tests when the initial physical damage is large. However, with no general trends emerging for D_ν as a function of the number of shock cycles, further analysis of secondary damage measures such as D_G will be explored in Figure 4-8.

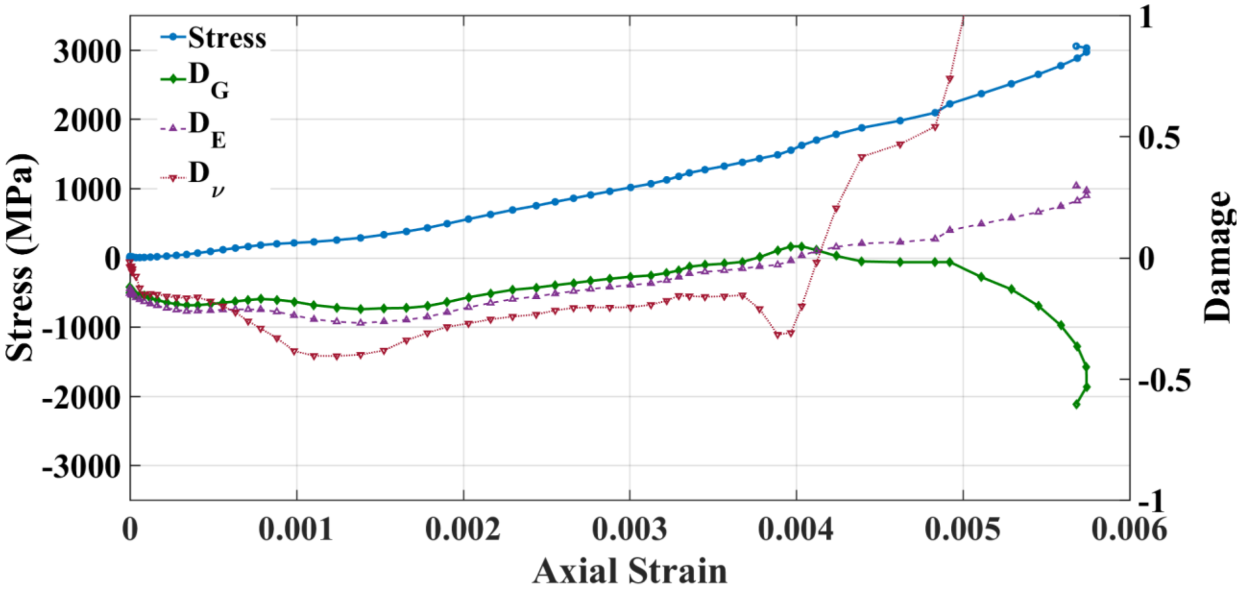

Figure 4-8 – Stress (left axis) and damage measures (right axis) vs. axial strain for SC3DYN02. Damage measures track apparent changes in Young's modulus (E), Poisson's ratio (ν), and shear modulus (G). While the sample shows an increasing Young's modulus while loaded, including a final apparent Young's modulus 25% greater than pristine quasi-static, it is the shear modulus where the actual damage appears most prominently.

To now, the raw data and the primary damage values D_E and D_ν have demonstrated some clear trends such as initial physical pre-damage producing initial D_E values below zero or failure being associated with $D_\nu > 0$, but outliers remain. It is at this point we move into the secondary damage values, and examine how D_G values calculated from Equation (7) influence understanding of the experiments. This understanding is first presented in Figure 4-8 for SC3DYN02 in specific and then explored for all cases in Figure 4-10. Previously, the greatest outlier of all of the pre-cracked materials examined in this study is SC3DYN02, as this sample shows a large increase in Young's modulus over pristine values and the lowest failure strain of all dynamic and quasi-static tests. By plotting D_E, D_ν, D_G, and stress vs. axial strain in Figure 4-8 the anomalous behavior shows a clearer trend. Namely, D_G is negative or approximately zero through the entire loading process. When D_E becomes positive at 0.0041 axial strain then D_ν has a sudden increase that causes D_G to become negative once again, undergoing a rapid decrease up to failure. As seen in Figure 4-6, for most samples, D_E trends towards $D_E = 0$ as axial strain increases up to failure, while Figure 4-7 has D_ν demonstrating much more varied and asymptotic behavior before failure for all samples. Figure 4-8 also illustrates that when SC3DYN02 is plotted as D_G vs. axial strain, three loading phases are seen. The first phase, from 0 to 0.0041 axial strain has the sample starting with a low D_G value, with D_ν being negative and D_E being less than D_G. In the second phase from 0.0041 to 0.0049 axial strain, $D_G = 0 \pm 0.05$, indicating that the sample has an essentially pristine shear modulus even while D_E and D_ν are continuing to evolve. In the third phase, from 0.0049 strain to catastrophic fracture at 0.0057 axial strain in Figure 4-8, D_G rapidly decreases. This and evidence from other tests not shown for brevity suggests there are three distinct loading processes associated with D_G, which we propose to name *recovery*, *plateau*, and *failure stages*. Figure 4-9 shows D_G vs. axial strain curves for SC0DYN02, SC1DYN01, and SC4DYN01, with these stages highlighted to better show these changes in behavior. Notably, while SC0DYN02 and SC4DYN01 show distinct *failure stages*, SC1DYN01 does not show a *failure stage*, as the sample undergoes fragmentation that prevents DIC measurement of strains during unloading. However, while SC1DYN01 has a lower D_G during the *plateau stage* than either SC0DYN02 or SC4DYN01 and has no *failure stage*, its *plateau stage* ends at the same strain as SC0DYN02 and at a higher strain than SC4DYN01. For these three tests the number of shock cycles does have an apparent correlation with a parameter, in that the length of the *plateau* increases with increasing pre-damage, and the length of the *recovery stage* decreases with increasing pre-damage. With these observations we can now examine all of the D_G vs. axial strain curves to demonstrate the patterns seen in Figure 4-8 and Figure 4-9 continue to hold.

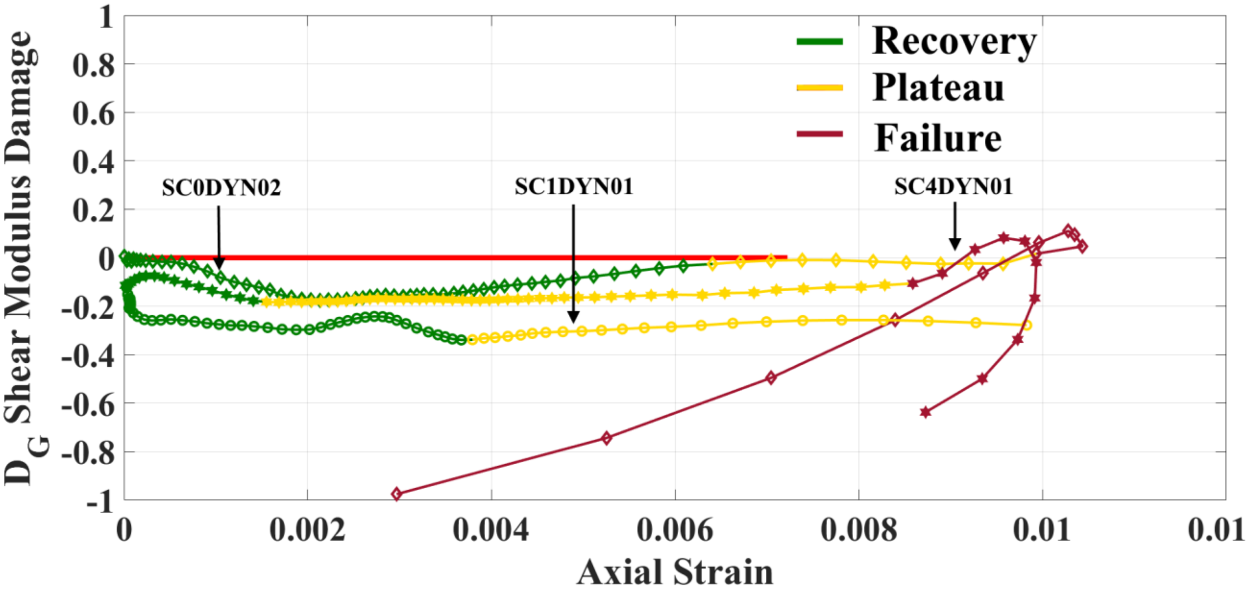

Figure 4-9 - D_G shear modulus damage vs. axial strain for SC0DYN02, SC1DYN01, and SC4DYN01 showing the different behavioral stages separated by color. The first stage, *recovery*, is in green and features an initial decline in apparent shear modulus, before either returning to D_G for SC0DYN02 or assuming a consistent state for SC1DYN01 and SC4DYN01. The second stage in yellow is the *plateau stage*, wherein the D_G value remains near constant as axial strain increases. The third stage is in red and is the *failure stage*, wherein the value of D_G begins to rapidly change with axial strain, including axial strain decreasing. In this figure only SC0DYN02 and SC4DYN01 demonstrate a *failure stage*, with SC1DYN01 suffering catastrophic fragmentation at the end of its *plateau stage* and thus losing correlation.

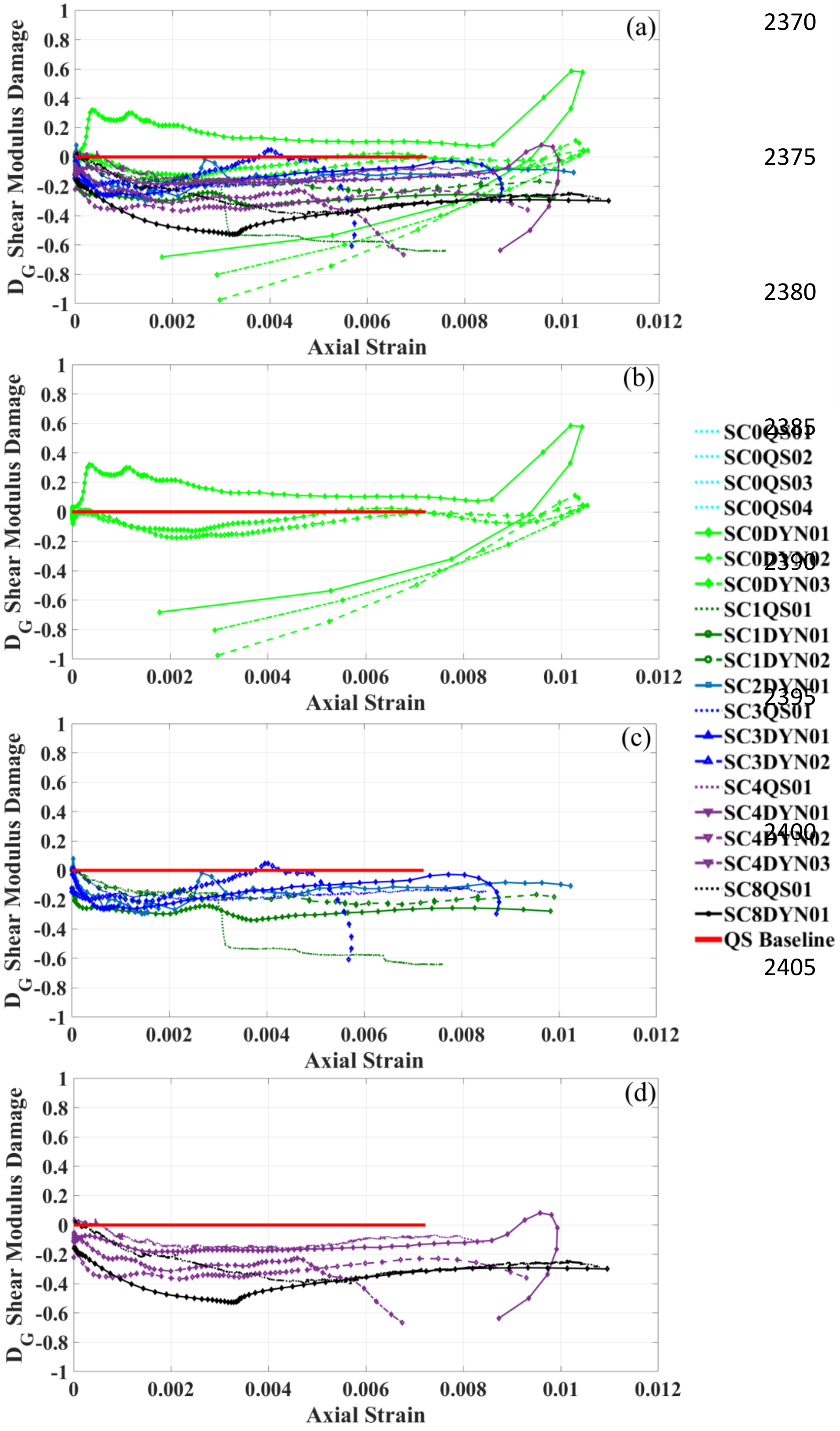

Figure 4-10 - D_G shear modulus damage for all samples. Panel (a) shows all tests, panel (b) shows only the tests where no thermal shock cycles were applied, panel (c) has the samples subjected to between 1 and 3 shock cycles, and panel (d) has the samples subjected to 4 and 8 shock cycles. A red line has been added to all images showing the expected linear elastic behavior to failure strain with no damage before failure. Pristine quasi-static lines are obscured by the baseline quasi-static line, which captures their behavior. The image shows that shear modulus damage is consistently negative at failure, even when materials such as SC0DYN01 exhibits an apparent increase in Young's modulus before failure. In this way of showing the data physical damage primarily manifests as a reduction in the capacity for the sample to tolerate shear damage before fracture.

Figure 4-10 shows D_G vs. axial strain for all pristine and pre-damaged samples, following the same conventions for panels (a) through (d) as in prior figures. Here it can be seen that all samples fail with a negative D_G value. For the pristine dynamic tests D_G values at ultimate failure are between -0.7 and -1.0, with -1.0 being a total loss of shear modulus, while the pre-damaged samples show D_G values at failure between -0.2 and -0.6. While it seems counter-intuitive for pristine samples to have greater D_G damage at ultimate failure than pre-damaged material, the overall curves help explain why pristine samples would have a more negative D_G value at ultimate failure. Namely, the more pre-damaged samples frequently have no *failure stage*, in comparison to the extended *failure stages* of the pristine samples. This lack of a *failure stage* is due to the fact that the samples fail catastrophically in a way that DIC cannot capture the change in mechanical behavior while the material physically disintegrates. For example, in Figure 4-10 the pristine SC0DYNX samples, SC3DYN01, SC3DYN02, SC4DYN01, and SC3DYN03 demonstrate definite *failure* sections. Specifically, SC1QS01 demonstrates large drops in D_G during loading, caused by the large jumps in lateral vs. axial strain seen in Figure 4-5(a) at 0.0030 and 0.0064 strain. All other pre-damaged samples have their curves end with no distinct *failure stage*. This suggests that intact materials are able to tolerate a *failure stage* before fracturing, while the samples with more pre-damage will fracture as soon as the *failure stage* begins. Further examination of the tests in Figure 4-10(c) shows how physical damage increases could change how mechanical damage behavior manifests. Figure 4-10(c) contains the samples that underwent 1, 2, or 3 shock cycles and, thus, there is an increasing amount of pre-damage. Here the SC1 series demonstrate the lowest D_G *plateau* values of the three shock cycle series shown, no distinct *failure stage*, and low failure strain. The SC2DYN01 test shows the highest failure strain, and during the *plateau stage,* demonstrates a D_G value between that of the SC1 and SC3 samples. Finally, the SC3DYN01 and SC3DYN02 show the greatest recovery of shear modulus, but also considerably lower failure strains and pronounced *failure stages*. Comparing between quasi-static tests alone, SC1QS01 has a much lower D_G and failure strain at fracture (D_G = -0.64 at 0.0076 strain) than SC3QS01 (D_G = -0.15 at 0.0084 strain). This suggests that physical damage manifests as mechanical damage in a complex manner that affects the ability of the sample to tolerate shear modulus degradation. Combining the general observations of Figure 4-10 with the insights from Figure 4-9, a trend emerges: samples with a low number of shock cycles exhibit large initial degradations in the shear modulus and are prone to fragmentation without a distinct *failure stage*, but their *plateau stages* reach approximately the same axial strain as the pristine materials. As the amount of pre-damage increases, the materials have higher initial D_G values and greater recovery towards $D_G = 0$, but at the cost of the *failure stage* beginning at lower axial strains. The presence of *failure stages* in highly pre-cracked material thus becomes indicative of early failure. SC8DYN01 reverses this trend by having a low value of D_G initially and at failure, and by having the highest failure strain of all tests, but the behavior of SC8DYN01 is convergent with SC8QS01. These and other previously noted behaviors are further examined in the Discussion in the context of the relationship between physical damage and mechanical damage.

4.5. Discussion

This research has discovered a number of key points about the relationship between physical damage and mechanical damage, and how the accumulation of both serves to degrade properties, which are summarized as:

1.) Physical damage reduces mechanical properties such as failure strength, failure strain, and apparent Young's modulus, but it is not a linear relationship where more physical damage results in more mechanical damage as previously assumed [26,36,55,194,195], and there is an additional interaction when comparing dynamic to quasi-static loading;

2.) Quantitative end points such as failure stress and strain are insufficient to explain the behavior of pre-damaged material, as the accumulation of damage involves a series of stages from the *recovery stage* to the *plateau stage* to the *failure stage,* each with different behaviors that depend on initial and current physical damaged states; and

3.) Damage to the shear modulus (D_G) of a material appears to be the most indicative factor for damage accumulation as a criterion for failure rather than damage to Young's modulus (D_E) or Poisson's ratio (D_ν). All of these points have not been predicted by prior models of brittle fracture processes[26,36,55,194,195], but elements of the physical phenomenon have been seen in other fields[1,101,103,140,170,173,174,196] that will guide the interpretation of the observations made in this paper.

First, the complex relationship between physical damage, mechanical damage, their evolution, and strain rate is well illustrated in Table 4-1, Figure 4-6, Figure 4-7, and Figure 4-10. The data there shows that the physical damage caused by thermal shock reduces failure strength, failure strain, and initial apparent Young's modulus, while dynamic loading increases failure strength and failure strain in comparison to quasi-static loading. However, increasing physical pre-damage causes quasi-static failure strength and failure strain to increase, even above the pristine value, which has profound implications for models that use the quasi-static failure strength as an input, such as the JH-2 model[26], the Paliwal-Ramesh[55], or Hu-Ramesh[36] models. This phenomenon of improved quasi-static performance and degraded dynamic performance has been observed in advanced ceramics in the past, with Arab *et al.*[33] showing that the addition of SrO_3 to zirconia toughened alumina was able to increase fracture toughness under quasi-static conditions with a specific percentage addition of SrO_3, but decreased fracture toughness under dynamic loading for all percentages. This was attributed to the SrO_3 forming a secondary phase at grain boundaries that increased the porosity of the material, which increased the fracture toughness in quasi-static loading when there was an optimal concentration of SrO_3, but weakened the material for dynamic loading in all cases. This exact behavior can be seen with SC8QS01 and SC8DYN01, with SC8QS01 showing greater failure strength and strain than pristine, which, on their own, suggest that the material has superior failure strength despite being the most highly damaged sample. SC8DYN01 on the other hand has the lowest D_G during its *plateau stage* of all the dynamic tests, and since the purpose of the thermal shocks is to produce internal cracking and thus increase the porosity of the material, the situation is analogous to what occurred with Arab *et al.*[33]. The complexity of how physical damage manifests in mechanical damage across multiple potential performance metrics, such as failure strength or apparent Young's modulus response, suggests that there are multiple possible mechanisms for the material to accommodate strain, and which mechanisms are dominant during a test depends upon the interaction of pre-damage, total strain experienced, and strain rate. The complex relationship between the responses feed into the second point about the importance of how damage accumulates with increasing strain, and this is explored next.

Following on the idea that the thermal shock induced physical damage has a complex effect on the mechanical response of the materials, it can be seen that the SC0DYN series have a noticeably different shape from the SC8 samples, even though by Table 4-1 a sample experiencing eight thermal shock cycles results in an average failure strength 77±5% of pristine and a 6±2% increase in failure strain. Qualitatively, the behavior seen in Figure 4-4, Figure 4-5, Figure 4-6, Figure 4-7, and Figure 4-10 are distinct between the pristine, moderately damaged, and most damaged samples. Examining Figure 4-10 by seeking the *recovery*, *plateau*, and *failure stages*, the trend suggested is that the pre-cracking physical damage is something the material accommodates through the rearrangement of cracks at the cost of reducing the strain at which the *plateau stage* ends and thus the *failure stage* begins. At a low number of shock cycles, the amount of apparent rearrangement is low, as seen in Figure 4-9 by the way SC1DYN01 has a relatively short *recovery stage* and a change in D_G of 0.0060 between the start and end of the *plateau stage*. This rearrangement to accommodate stress reduces apparent shear modulus and reduces the capacity to sustain a *failure stage*. For SC4DYN01 in Figure 4-9, the initial loss of shear modulus is lower than the less damaged SC1DYN01, but its *plateau stage* ends at a lower strain than SC0DYN02 or SC1DYN01, and the other SC4DYN curves in Figure 4-10 shows that the early failure is even more pronounced in SC4DYN02 and SC4DYN03. Just within Figure 4-10(c), going from 1 shock cycle to 3 shock cycles shows an increased *recovery* of D_G, but the *failure stage* begins at lower strains and the more pre-damaged samples show larger changes in D_G than the less pre-damaged samples, which fracture at the end of their *plateaus*.

Second, extending and interpreting the second discussion point, the presence and absence of the *recovery* and *failure stages* allows for the complex interaction of pre-damage and strain rate effects to be better understood. Comparing SC0DYN to SC0QS shows that the dynamic tests have a recovery period where $D_G \neq 0$ while the quasi-static tests remain at $D_G = 0$, and for all samples with pre-damage up to the SC8 series, the dynamic tests have a higher failure strain than the quasi-static tests. One inference is that starting from pristine quasi-static as a baseline, pre-damage past the first shock cycle and dynamic loading have a similar effect: a recovery period and an increased failure strain. The first shock cycle is the exception, likely due to the difference in pre-existing flaws between SC0 and SC1 being much larger than between SC1 and SC8, with any intermediate behaviors not captured. The fact that pre-damage and dynamic loading have similar mechanical responses suggests that a similar physical mechanism is responsible for both behaviors. This physical response is hypothesized here to be the activation of additional flaws, identified in the literature to be a cause of the difference in behavior between quasi-static and dynamic response[197]. In a sample with large amounts of initial pre-damage, the cracks have to be rearranged to support applied loads, forcing the activation of flaws smaller than the most significant flaw in order to facilitate load transfer to the bulk material. Under dynamic loading this is caused by the material not having sufficient time to communicate the presence of a loading event to the most significant flaw without activating other flaws in the way[197]. This similarity in response between pre-damage and dynamic loading suggests that the early *recovery* and *plateau stages* may contain important information on how a ceramic will perform once it reaches the *failure stage*.

The third discussion point to address is that the shear modulus shows a more useful description of the behaviors expected to arise from physical damage than the apparent Young's modulus or Poisson's ratio demonstrate. Prior findings[175] already suggested that the Poisson's ratio damage was more indicative of accumulating physical damage than Young's modulus damage for brittle materials subjected to dynamic loading, but this paper now shows that their combined behavior in the apparent shear modulus is more indicative. As seen in the behavior of SC3DYN02, the apparent Young's modulus can increase, so long as Poisson's ratio increases faster, and, thus, shear modulus decreases. This is a key insight for models that use a damage term, as those models assume that their equivalent terms for damage D_E vary from 0 to -1[26,36,55,194,195]. Taking Equations (4-5) through (4-7) and assuming that Poisson's ratio remains constant ($\nu_{app} = \nu_0$) produces Equation (4-8):

$$D_G = \frac{\frac{E_{app}}{2(1+\nu_0)}}{\frac{E_0}{2(1+\nu_0)}} - 1 = \frac{E_{app}}{E_0} - 1 = D_E \tag{4-8}$$

Equation (4-8) states that under the assumption that ν does not change with an applied load that $D_G = D_E$, which means that any prior model making this assumption of Poisson's ratio invariance would not distinguish which of these two elastic moduli was changing. With a growing recognition in the literature that shear plays an important role in the failure of brittle materials[101,131,149,150,168,179,181,191,198,199], the finding of shear modulus loss as an important metric in the failure of ceramics provides evidence for future focus on the study of shear failure in ceramics and how shear modulus damage evolution affects performance.

4.6. Conclusion

In this paper, we have combined together thermal shocking of ceramics to induce pre-damage via internal fracturing with previously developed techniques for combining DIC with Kolsky bar and load frame tests to observe mechanical damage accumulation with strain. Through this experimental set up we have been able to discover the complex manner in which strain rate and pre-damage interact with each other, and how physical damage manifests in non-linear and non-monotonic ways. In particular, dynamic loading can be divided into *recovery, plateau,* and *failure stages* that provide more information and context than end point measures such as failure strength or failure strains. It has also been discovered that changes to the shear modulus is more indicative of physical damage accumulation during mechanical loading than changes to Young's modulus or Poisson's ratio.

Tables

Table 4-1 – Key data on damaged samples tested, with the number of thermal shock cycles and the failure strength and failure strain when subjected to compression.

Name	Thermal Cycles	Failure Strength (GPa)	Failure Strain (%)
QS Baseline	0	2.60	0.72
SC0QS01	0	2.73	0.75
SC0QS02	0	2.60	0.64
SC0QS03	0	2.42	0.66
SC0QS04	0	2.25	0.65
SC0DYN01	0	3.91	1.00
SC0DYN02	0	3.74	1.00
SC0DYN03	0	4.06	1.05
SC1QS01	1	1.83	0.76
SC1DYN01	1	3.01	0.98
SC1DYN02	1	2.78	1.00
SC2DYN01	2	3.33	1.02
SC3QS01	3	2.43	0.83
SC3DYN01	3	3.30	0.91
SC3DYN02	3	3.10	0.63
SC4QS01	4	2.43	0.84
SC4DYN01	4	3.39	1.03
SC4DYN02	4	3.09	0.92
SC4DYN03	4	2.07	0.67
SC8QS01	8	2.82	1.08
SC8DYN01	8	3.17	1.08

Chapter 5 – Damage Accumulation Mechanisms During Dynamic Compressive Failure of Boron Carbide

5.1. Introduction

Ceramics form a core component of modern armor systems against higher level threats[18,200,201] due to their high hardness[202] and brittle fracture failure mode[17,203], producing favorable processes for blunting projectiles such as dwell and interface defeat[23,24,204,205], conoid cracking[16,206], and granular flow of comminuted material[198,207,208]. The ideal ceramic for armor purposes possesses both high hardness and low density so as to maximize protection to mass[117,209–211], with boron carbide being a leading material[210–214] for possessing among the highest hardness and lowest density of advanced ceramics, a group that also includes silicon carbide[215,216] and aluminum oxide[217–219] as the most common ceramics used in armor applications. While boron carbide has advantages over other ceramics, it also has disadvantages and complexities that motivate further study. Examples of interest are the complex crystal structure[220,221], graphitic inclusions [221–223], and mechanical anisotropy [53,108,176]. One topic of interest in boron carbide research is amorphization[221,224–229], the process by which shear stresses cause the atomic and crystalline structure of boron carbide to rearrange into a weaker form[53,222,229,230]. These shear-induced processes are typically studied using indentation at quasi-static and dynamic rates[227,228] or under plate impact[212,225,231]. In this paper, we seek to contribute to the understanding of failure in boron carbide under strain rate-dependent uniaxial compression loading.

Recent advances in combining digital-image-correlation with ultra-high-speed imaging and Kolsky bar compression experiments[60,107,110,111,175,177,232] have shown that changes in elastic properties from fracture and failure events are both non-linear and non-monotonic[175]. These results run counter to prior expectations[26,57–59] but come about from the interaction of the evolution of apparent Poisson's ratio and Young's modulus during loading and failure. One method of tracking changes to Poisson's ratio and Young's modulus simultaneously is to combine them into another elastic modulus, such as the shear modulus, used by Koch *et al.*[232]

in the study of alumina samples that were damaged by thermal shock before compressive loading. Shear modulus degradation was shown to have a greater correlation for the way the materials behaved than Young's modulus or Poisson's ratio changes taken in isolation[232]. Specifically, while the apparent Young's modulus was capable of increasing above the quasi-static value even during failure, the shear modulus was consistently below the pristine value at failure [232]. These findings taken with boron carbide's shear failure behaviors[226–228] motivate this current paper. This current paper investigates how two different forms of boron carbide undergo damage evolution with strain across a range of strain rates and how study of shear modulus damage accumulation reveals changes to the understanding of how damage accumulates in advanced ceramics. Within the range of strain rates studied, one of the forms of boron carbide undergoes a transition in the form of damage accumulation, demonstrating a change in failure mechanisms. The implications of this change in mechanisms constitutes both a novel finding experimentally and provides key insights for modelling and design work.

5.2. Experimental Setup & Methods

5.2.1. Materials

Material behaviors in this investigation are studied within a context of uniaxial compression, using samples machined into cuboids of dimensions of 3.5 mm x 2.7 mm x 2.3 mm. Shown in Figure 5-1 is an example of a sample with a speckle pattern used for Digital Image Correlation (discussed later). These sample sizes were used in both quasi-static and dynamic testing and were chosen to conform with prior studies[108], but reduced in dimensions in order to produce higher pressures with less force used. The material of interest in this study was boron carbide, categorized into two types, named as S-Series and Z-Series. The S-Series is a polycrystalline boron carbide, while the Z-Series contains titanium diboride in addition to the boron carbide, and so is a ceramic-ceramic composite. More information on the material composition of the S and Z-series can be found in Lo *et al.*[233]. In this paper, the mechanical properties and failure behaviors of these materials were determined via quasi-static and dynamic testing. Quasi-static testing is primarily used in order to determine the average mechanical properties of the materials, and they were found to conform to data in the literature[234–236]. Dynamic testing produced more complex results, where important variance between individual samples is found to be strain-rate dependent. Dynamic tests are labelled based on the strain rate they were tested at, which is determined by the combination of projectile and pulse shaper used, with the details explained below as part of the description of the Kolsky bar apparatus that is used in this study.

5.2.2. *Quasi-Static Testing*

For this study, the quasi-static compressive strength and Young's modulus were evaluated through mechanical testing using an MTS 810 materials testing machine that compressed samples to failure. In these quasi-static experiments, a strain rate of 10^{-4} s^{-1} was used. The servo-hydraulic controls provided precise measurement of forces, accurate to 0.1 N. A Digital Image Correlation (DIC) setup discussed in depth in subsequent paragraphs was used to determine axial and lateral strains during compressive loading. Stresses and strains were matched in time to produce stress-strain curves in the quasi-static experiments. For quasi-static DIC, a Promon U750 camera recording at 100 Hz was used to capture the entirety of a 30 to 50-second-long experiment. The framerate was sufficient to capture axial and lateral strain data that could be used to calculate Young's modulus and Poisson's ratio values for the linear elastic section of the test. The final failure occurs on a single digit millisecond time scale, making the 100 Hz acquisition rate of the camera records insufficient to capture the behavior of samples after peak stress.

5.2.3. *Dynamic Testing*

Dynamic compression testing was done using a Kolsky bar testing apparatus and an ultra-high-speed Shimadzu HPV-X2 camera capable of capturing 128 frames up to ten million frames per second and 400 x 250 pixel resolution. For the experiments performed here, a framerate of 500,000 to 2,000,000 frames per second (FPS) was used at full resolution. The specific framerate used depended on the loading rate of the experiment, which is described below. The ultra-high-speed camera system used a K2 Infinity Lens to fill the sample in the 4 mm by 6.5 mm field of view of the camera. An example image of a sample with a speckle pattern used in dynamic testing is shown in Figure 5-1. In this study, the Kolsky bar apparatus used incident and transmitted bars that were 12.7 mm in diameter and made of maraging steel (Service Steel America C-350) with a Young's modulus of 200 GPa, Poisson's ratio of 0.29, yield strength of 2.68 GPa, and a density of 8100 kg/m^3. The incident bar was 101.6 cm in length, while the transmitted bar was 91.4 cm in length. Using compressed gas to provide the impulse, one of two types of projectiles made from maraging steel was launched into the incident bar, so that the impact produced a strain pulse in the incident bar (details forthcoming). In order to protect the incident and transmission bars from damage by ceramic samples harder than the steel, 5 mm thick and 7.94 mm diameter tungsten carbide platens jacketed in 12.7 mm outer diameter titanium rings were used. High pressure grease was applied at the platen-sample interfaces in order to reduce the transmission of lateral or shear strains from the bars into the samples and to ensure that the input pulse was as uniaxial as possible.

Of the projectiles used, one was a shorter bar that was 152 mm long, and the other was 304 mm in length. As mentioned previously, these two lengths are used to modify the duration of the input pulse and, thus, modify the strain rate, especially in conjunction with the use of pulse shaping. A near-triangular pulse is considered ideal in Kolsky bar experiments for brittle materials[61,71], and this was achieved in this present study by using a 3.175 mm diameter and 1 mm thick high density polyethylene or tin pulse shaper. The materials for both pulse shapers were obtained from McMaster-Carr. For tests where the long projectile was used with tin (termed LTP), this produced strain rates of 200 ± 30 s^{-1} and used a camera acquisition framerate of 500,000 FPS. For the combination of the long projectile with polyethylene (LP), this produced strain rates of 400 ± 100 s^{-1} and these tests used a camera framerate of 1M FPS. Finally, for the combination of the short projectile with polyethylene (SP), test strain rates of 900 ± 200 s^{-1} were achieved and these used a camera framerate of 2M FPS. The pulse durations were 250 ± 30 μs for LTP tests, 150 ± 20 μs for LP tests, and 100 ± 20 μs for SP. These pulse durations are much longer than typically used in the literature of 50 to 100 μs rise times[61,71], but have allowed us to achieve good stress equilibrium[117] and measurements[60] for the purpose of our current study.

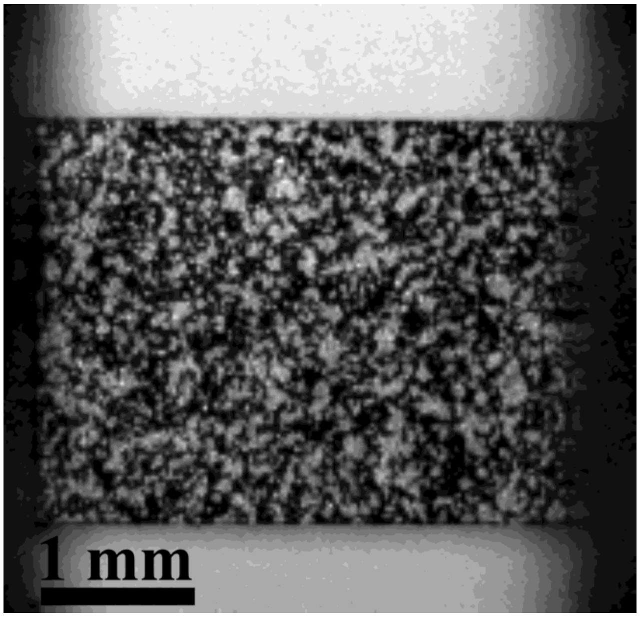

Figure 5-1 –An example of an S-Series boron carbide sample sprayed with a speckle pattern for DIC purposes that is held between the incident (left side) and transmitted bars (right side) of the Kolsky bar. The field of view in the vertical direction has been cropped in order to better show the features of the sample.

As a demonstration of loading equilibrium across the sample in the experiments in this paper, Figure 5-2 shows axial strain vs. time and stress vs. time simultaneously for S-LP1 (S material, long projectile, first experiment). Axial strains are shown for both the entire area of interest and for sub-sections of the sample surface (right in Figure 5-2), which shows that the strain field is uniform in space and time and the stress follows the strain, both an indicator of good loading equilibrium. Here, the transmitted stress was measured by six strain gauges arranged in three pairs, with two pairs on the incident bar, and one pair on the transmitted bar. Each pair had an additional two gauges not connected to the bars but connected together to form a full wheatstone bridge, with each bridge connected to its own Vishay 2310b amplifier. The signals were sent to an HBM Gen3i high speed portable data acquisition system sampling at 2 million samples per second. The strain gauge types were HBM LD20 350 ohm resistance gauges secured in place via cyanoacrylate adhesive. Tests were only considered successful when strain responses and camera images confirmed that samples failed in loading and on the first loading pulse through the material, and we saw no evidence of edge chipping. This setup has been used previously in Koch *et al.* [175,232], Li *et al.*[107,110], and Lo *et al.*[60,177], and is consistent with other Kolsky bar testing systems considered state of the art in a study by Swab and Quinn[114].

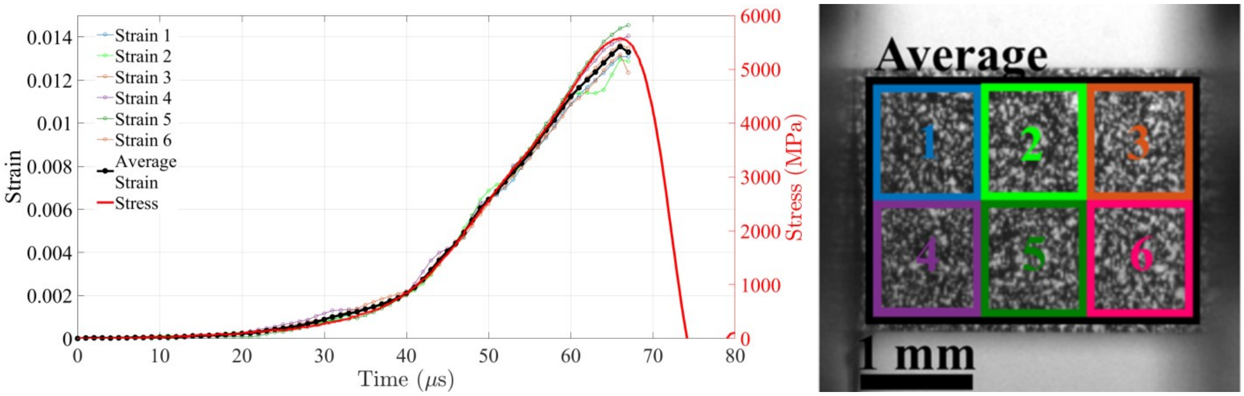

Figure 5-2 – Strain and stress vs. time plot for S-L1 on the left, and the sample showing the various DIC regions of interest on the right. The average strain vs. time response and the stress vs. time response follow each other and the individual strain responses are not strongly affected by the region, showing that the sample is experiencing good equilibrium.

5.2.4. Digital Image Correlation

The camera images from the quasi-static and dynamic tests were used for digital image correlation (DIC) analysis in order to determine axial and lateral strains, and these are used for precise measurements of Young’s Modulus and Poisson’s ratio. DIC is a computer vision technique that uses the changes in position of speckle patterns on the surface of an object in order to compute deformation fields, and is well established in the study of many different materials[118–122]. DIC has been used previously in Kolsky bar experiments by the authors [60,107,110,175,177,232,237] to track axial and lateral strains in ceramics. Because of the small size of the samples in our study, use of an airbrush with a 0.15 mm nozzle was required in order to produce speckle patterns sufficiently fine for use in low noise measurements (speckles are seen in Figure 5-1). The high speed of image capture and thus low exposure times (~200 ns) required the use of a high gloss metallic paint for the speckles and high intensity LED ring light (REL Inc.) to produce sufficient contrast in the images needed for low error analysis. The commercial DIC software VIC-2D (v6 2018) from Correlated Solutions (Irmo, South Carolina, USA) was used to obtain the strain fields. The regions of interest were discretized into 27 by 27 pixel subsets with a step size of 7 pixels for the dynamic tests. The correlation analysis was carried out using the optimized 8-tap interpolation scheme, with the shape function being internal to the software but based on derivatives of displacements and using a zero-normalized sum of squared differences criterion. Pre-filtering of images was done with a low-pass filter, while subset weighting was done via a Gaussian weighting, with no additional post-processing smoothing. Confidence intervals for correlations were consistently within the range of 10^{-3} to 10^{-}

^{4} pixels, leading to measurement uncertainty arising primarily from equipment and taken to be no greater than a conservatively large 5% in total. The greatest source of uncertainty was the initial size of the samples in the visual field, taken as being 0.1 mm out of the 2.7 mm side length of the 2.7 mm by 3.5 mm face used for measurement, which amounts to ~4% uncertainty in strain as determined by DIC. Strains were computed from the displacement fields using the engineering strain tensor in the DIC software. Computed strain histories were matched to the stress histories from the strain gauges on the Kolsky bar to determine stress-strain curves for each experiment, as is commonly done in Kolsky bar experiments in the literature[61,117,193]. With axial and lateral strains measured independently of the stress, variations in apparent Young's modulus and Poisson's ratio can be tracked with time and strain.

5.2.5. Methodology for Quantifying Damage to Elastic Constants

Mechanical damage is defined for the purposes of this paper as an apparent change in a mechanical property from quasi-static linear elastic properties. The damage can both increase or decrease the elastic properties. If a sample demonstrates more axial strain for a given stress load then it would be said to have a negative stiffness damage, while if it experienced more lateral strain for a given stress load then it would be said to have a positive Poisson's ratio damage. There are three mechanical damage terms used in this paper: the Young's modulus E, the Poisson's ratio v, and the shear modulus G. Information on the derivation of the first two damage measures can be found in Koch *et al.*[175] and the derivation of the shear modulus damage can be found in the follow-up paper by Koch *et al.*[232]. The damage values are, respectively, D_E, D_ν, and D_G, and are calculated with Equations (5-1)-(5-3).

$$D_E = \frac{E_{app}}{E_0} - 1 \tag{5-1}$$

$$D_\nu = \frac{\nu_{app}}{\nu_0} - 1 \tag{5-2}$$

$$D_G = \frac{G_{app}}{G_0} - 1 \tag{5-3}$$

where E_0, ν_0, and G_0 are the pristine, quasi-static values of the elastic properties, while E_{app}, ν_{app}, and G_{app} are the apparent elastic properties derived from experimental observations and calculated using Equations (5-4)-(5-6):

$$E_{app} = \frac{\sigma_{inst}}{\varepsilon_{x_{inst}}} \tag{5-4}$$

$$\nu_{app} = \frac{\varepsilon_{y_{inst}}}{\varepsilon_{x_{inst}}} \tag{5-5}$$

$$G_{app} = \frac{E_{app}}{2(1+\nu_{app})} \tag{5-6}$$

where σ_{inst} is the stress at a given data point, $\varepsilon_{x_{inst}}$ is the axial strain at the same point, and $\varepsilon_{y_{inst}}$ is the lateral strain at the same data point. This form of determining the apparent elastic constants is used because of the limited number of data points available, especially in the failure region that is of greatest interest. A tangent approximation based upon the secant of closely spaced data points either truncates away the failure region or produces unrealistically large fluctuations in the apparent elastic properties from noise in the system.

Altogether, this framework allows for the exploration of how multiple apparent elastic properties evolve, which is important as it allows for non-monotonic and non-linear behaviors to be understood in the context of the competition between damage mechanisms that cannot be captured in a single term. With this framework, a number of behaviors seen in experiment such as strain decreasing while stress remains near constant, become understandable. These phenomena will be seen in the Results section (next) and the implications further elaborated in the Discussion (Section 5.4).

5.3. Results

5.3.1. Strain Rate Dependent Stress-Strain Responses

Elastic properties determined from the quasi-static and dynamic experiments for the S-Series are seen in Table 5-1 and the elastic properties for the Z-Series are summarized in Table 5-2. The S-Series has a slightly higher Young's modulus at 400 ± 20 GPa in comparison to the Z-Series at 370 ± 10 GPa. The Young's modulus and Poisson's ratio for both materials are taken from the quasi-static conditions due to deviance from those values under dynamic conditions being highly nonlinear as a result of failure, as will be discussed in the Discussion. The S-Series has a quasi-static failure strain of 0.0117 ± 0.0004 and failure strength of 4.7 ± 0.1 GPa. In comparison, the Z-Series has a quasi-static failure strain of 0.0083 ± 0.0003 and failure strength of 3.1 ± 0.1 GPa. Comparing the two series, the S-Series overall has an approximately 50% greater failure strength than the Z-Series under both quasi-static and dynamic conditions, and an approximately 20% greater failure strain under both conditions. The differences between the two series are related to the differences in chemical composition and microstructure, which is presented in Lo *et al*[233].

Table 5-1 – Material properties at various noted strain rates for the S-Series boron carbide, as measured using the methods described in Section 5.2.2 through Section 5.2.4.

	QS	**LTP**	**LP**	**SP**
Strain Rate (s^{-1})	10^{-3}	220±20	400±100	1000±200
Failure Strength (GPa)	4.7±0.1	5.6±0.2	5.5±0.2	5.6±0.5
Failure Strain	0.013±0.3	0.015±0.001	0.013±0.001	0.015±0.009
Young's Modulus (GPa)	400±20	420±10	430±40	440±60
Poisson's Ratio	0.15±0.01	0.17±0.02	0.15±0.01	0.20±0.04

Table 5-2 – Material properties at various noted strain rates for the Z-series boron carbide-titanium diboride composite, as measured using the methods described in Section 5.2.2 through Section 5.2.4.

	QS	**LTP**	**LP**	**SP**
Strain Rate (s^{-1})	10^{-3}	180±10	400±100	800±200
Failure Strength (GPa)	3.1±0.1	3.7±0.1	3.8±0.2	3.9±0.2
Failure Strain	0.0083±0.0003	0.0092±0.0003	0.0099±0.0008	0.0098±0.0006
Young's Modulus (GPa)	370±10	410±20	400±30	360±30
Poisson's Ratio	0.15±0.01	0.131±0.003	0.16±0.02	0.16±0.04

Figure 5-3 shows the stress vs. axial strain plots for the S and Z boron carbide series under dynamic compression conditions, divided into three subfigures by whether the test used the short projectile (1000 ± 200 s^{-1}), long projectile (400 ± 100 s^{-1}), or long projectile (200 ± 20 s^{-1}) with tin pulse shaper. This division categorizes the tests based on their strain rate, as discussed previously. A key element seen in these plots is a particular behavior seen after post-peak stress where the strain decreases faster than the stress decreases, resulting in an increase in apparent instantaneous stiffness. One of these tests is pointed out with an arrow in Figure 5-3, Panel A. This is a non-physical stress-strain result but provides qualitative information on the failure mechanisms that the material is undergoing. This unloading behavior is found in all tests for the Z-Series, half of the long projectile S-Series, and three quarters of the short projectile S-Series. For the S-Series that do not demonstrate this behavior, they will instead show increasing strains while stress decreases. The test that shows the highest failure stress, S-LTP1 with 5.91 GPa at a 0.0132 failure strain, is one of the tests that has an increasing strain and decreasing stress failure mode. S-LTP1 also has the highest post-peak axial strain. Altogether, the Z-Series have lower failure stresses and strains than the S-Series, and demonstrate more non-linear behavior in loading and unloading. The reasons for this will be explored in Section 5.3.3, and discussed in detail in the Discussion.

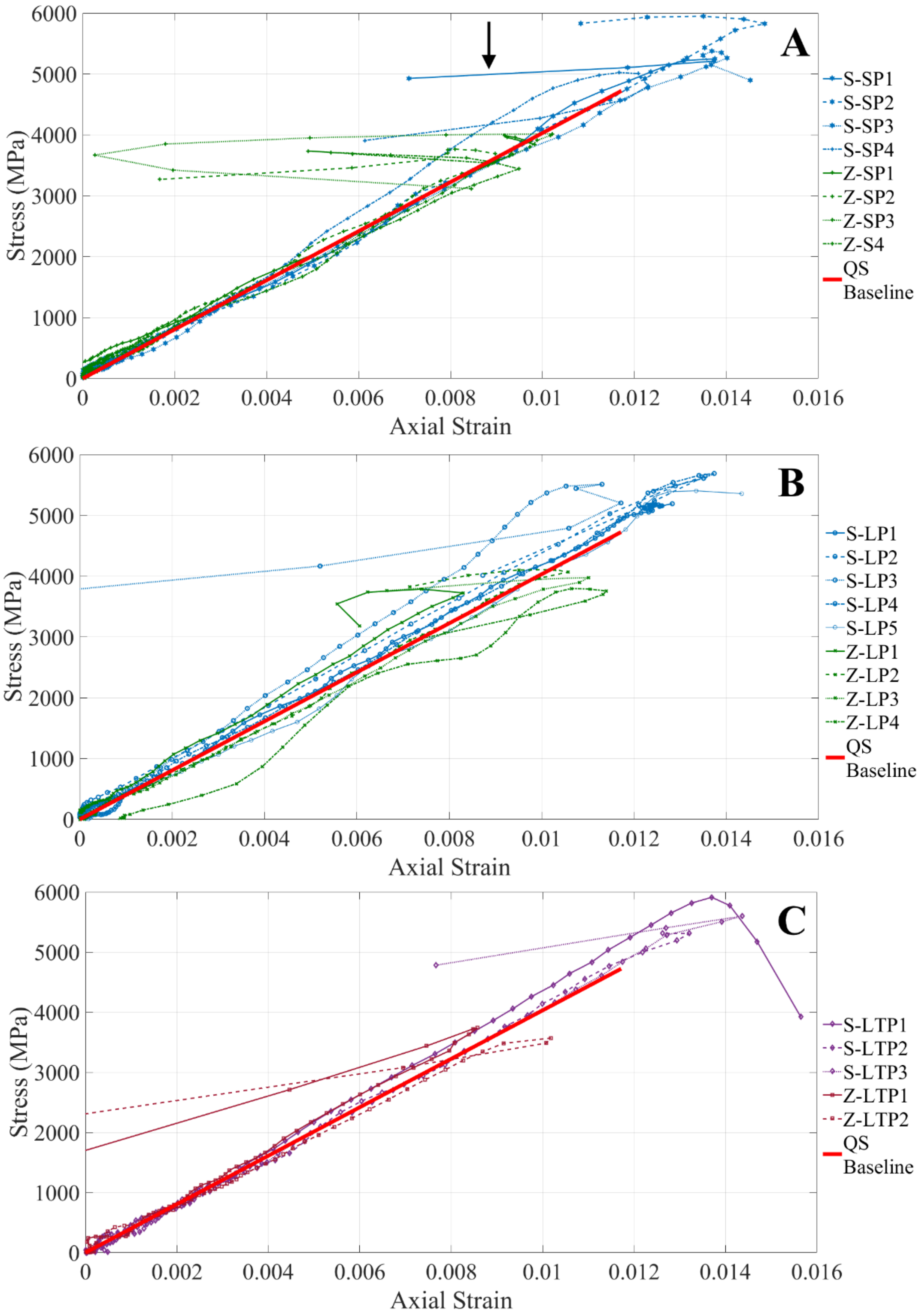

Figure 5-3 - Stress vs. strain for short projectile with polyethylene pulse shaper tests 1000 ± 200 s^{-1} (top, panel A), long projectile with polyethylene pulse shaper tests 400 ± 100 s^{-1} (middle, panel B) and long projectile with tin pulse shaper tests 200 ± 20 s^{-1} (bottom, panel C). The quasi-static tests for the S-series are summarized as a single linear line that shows how dynamic conditions cause deviation from linear elastic behavior. The arrow seen in Panel A points to an example of a test where the strain decreased faster than the stress. This behavior can be interpreted as an increase in apparent stiffness.

5.3.2. Strain-Rate Dependent Lateral-Axial Strain Responses

Figure 5-4 shows the lateral vs. axial strain plots for the S and Z boron carbide series undergoing dynamic uniaxial compressive loading, again divided into three subfigures based upon the projectile used, and, thus, the strain rate. Unlike in Figure 5-3, these plots are primarily linear with a Poisson's ratio of between 0.15 and 0.20 before failure, with exact numbers for each material at each strain rate given in Table 5-1 and Table 5-2. Neither material shows a strong rate dependency for Poisson's ratio before failure. After failure, if the axial strain decreases then the lateral strain undergoes a large increase. If the axial strain does not decrease, the lateral strain does not show a large increase either. These plots show that the lateral vs. axial behavior remains primarily linear before peak strain, and the anomalous behavior of strain decreasing faster than stress seen in Figure 5-3 corresponds to the tests with large increases in lateral strain. If the material were buckling outward, as suggested to explain asynchronous behavior seen in Figure 5-3, Panel A and designated by an arrow, then a large increase in lateral strain is expected; this is what is observed in Figure 5-4. This behavior also supports the possibility of significant internal crack growth producing additional lateral expansion to accommodate the crack growth[238].

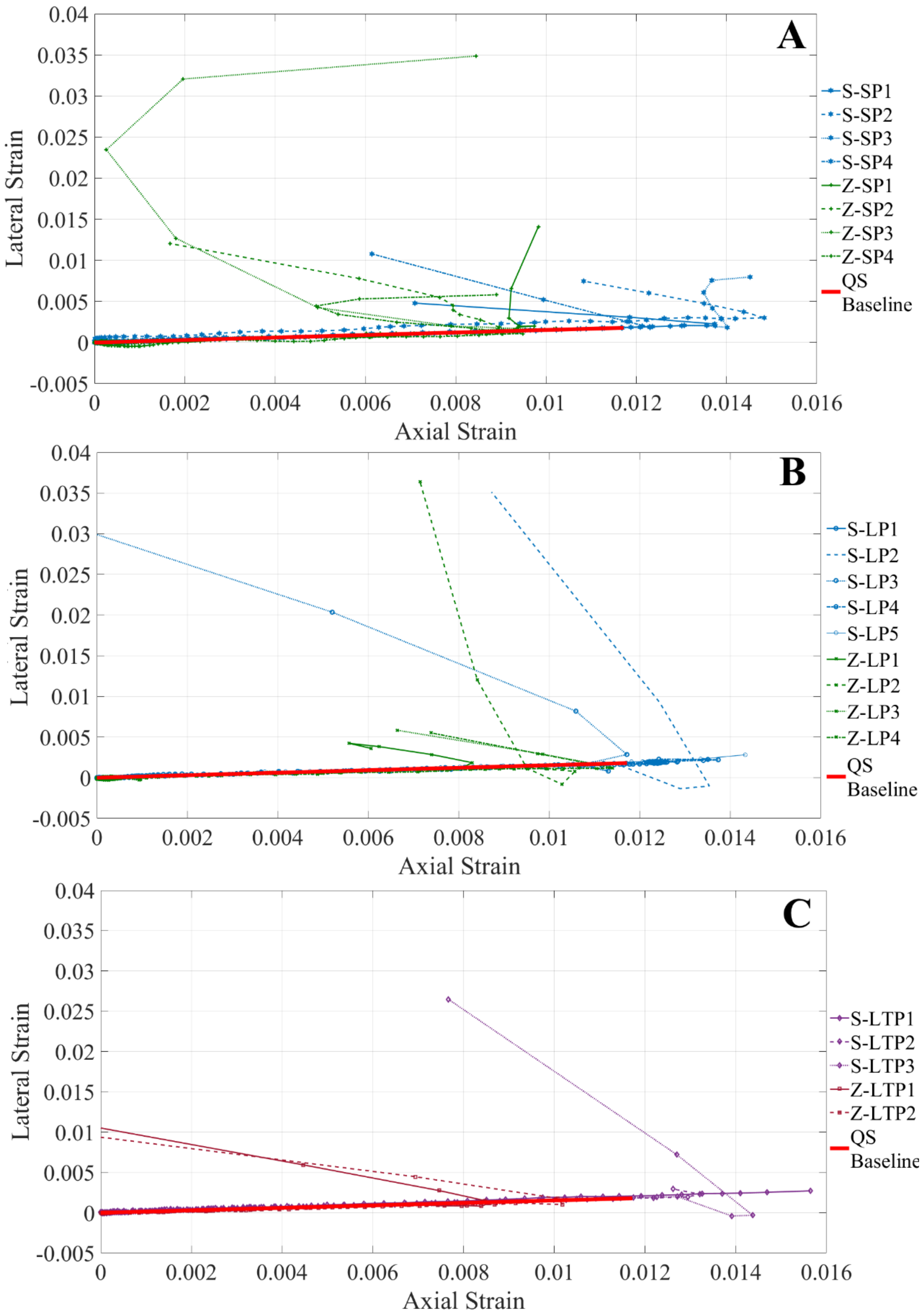

Figure 5-4 - Lateral vs. axial strain for short projectile with polyethylene pulse shaper tests 1000 ± 200 s^{-1} (top, panel A), long projectile with polyethylene pulse shaper tests 400 ± 100 s^{-1} (middle, panel B) and long projectile with tin pulse shaper tests 200 ± 20 s^{-1} (bottom, panel C). The quasi-static tests for the S-series are summarized as a single linear line that shows how dynamic conditions cause deviation from linear elastic behavior.

5.3.3. Damage Evolution with Axial Strain

Figure 5-5, Figure 5-6, and Figure 5-7 show the D_E, D_ν, and D_G vs. axial strain plots, respectively. These plots show how the S and Z series manifest damage in different elastic mechanical properties as their strain increases, and how strain rate influences these changes.

5.3.3.1. Stiffness Damage Evolution with Axial Strain

Figure 5-5 shows the D_E Young's modulus damage vs. axial strain for the S and Z boron carbide series undergoing dynamic compressive loading, divided into subfigures according to strain rate whether the test used the long projectile or the short projectile. At strain rates of 1000 ± 200 s^{-1} (Figure 5-5, Panel A), the S and Z series show consistent D_E behavior with minimal change (within 5% of mean values for a given test) before reaching maximum strain, at which point the boron carbide begins to unload. During the unloading process, the apparent strain decreases while D_E increases. In the intermediate strain rate regime of 400 ± 100 s^{-1} (Figure 5-5, Panel B), the behavior of both the S and Z series is more unstable, with both series having samples that demonstrated significant initial change in stiffness of ±20% before recovering to the baseline value before failure. Both series also have samples that demonstrate large changes in stiffness during the unloading phase, with apparent axial strain increasing and decreasing. A primary example of this behavior is seen in test S-LP5, which is indicated with an arrow in Figure 5-5, Panel B. This suggests that the samples that demonstrate rapid changes in apparent axial strain are undergoing complex surface strain evolution. Finally, for the long tin tests with strain rate of 200 ± 20 s^{-1} (Figure 5-5, Panel C), the S-LTP1 tests exhibits a behavior where D_E remains near constant throughout the test and then begins to smoothly decrease in value at a peak stress of 5.91 GPa at 0.0132 strain. Accounting for the differences in nomenclature, this behavior is what is expected from past theory[57–59], with stiffness damage accumulating smoothly and monotonically after peak stress, with strain continuing to decrease. Other S-series tests and the Z-series tests in the 200 ± 20 s^{-1} strain rate regime still show an increasing D_E while apparent axial strain decreases, but the large fluctuations that were observed in the 400 ± 100 s^{-1} regime are not present over these strain rates. The combination of both expected and unexpected behavior, and the instability of behavior suggests that there is a strain-rate dependent transition from one mode of failure to another that occurs for the S-Series in the strain-rates studied here.

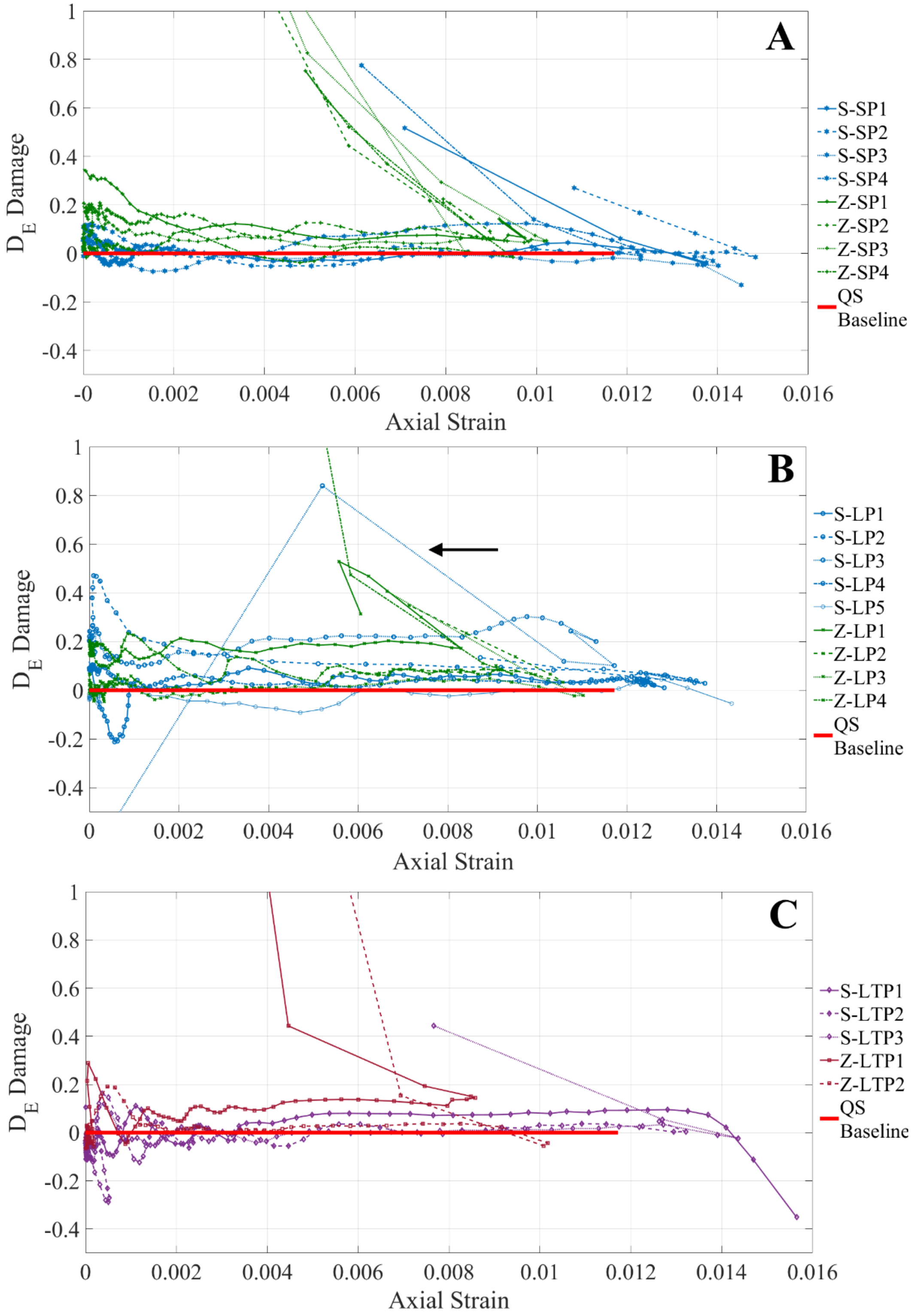

Figure 5-5 - D_E vs. strain for short projectile with polyethylene pulse shaper tests 1000 ± 200 s^{-1} (top, panel A), long projectile with polyethylene pulse shaper tests 400 ± 100 s^{-1} (middle, panel B) and long projectile with tin pulse shaper tests 200 ± 20 s^{-1} (bottom, panel C). The quasi-static tests for the S-series are summarized as a single linear line that shows how dynamic conditions cause deviation from linear elastic behavior. The arrow in Panel B points to the test S-LP5, which increases and decreases in D_E during the unloading process. This can also be seen in Z-LP1.

5.3.3.2. *Poisson's Ratio Damage Evolution with Axial Strain*

Figure 5-6 shows the D_ν Poisson's ratio damage evolution vs. axial strain for the S and Z boron carbide series undergoing dynamic uniaxial compression, divided into subfigures according to strain rate whether the test used the long projectile or the short projectile. For the 1000 ± 200 s^{-1} high strain rate experiments (Figure 5-6, Panel A), both the S and Z-series show large D_ν increases after reaching peak strain. Two tests also show divergent behavior from the general trends from the rest of the tests, namely S-SP2 and Z-SP3 (these are labeled in Figure 5-6, Panel A as 1 and 2, respectively). In the S-SP2 case, the experiment begins with $D_\nu > 1$, which indicates that it has a Poisson's ratio greater than twice the quasi-static value (in absolute terms this is a Poisson's ratio of approximately 0.3). The D_ν value then decreases as the axial strain increases throughout the test, indicating that volume is being conserved less and less as the experiment occurs. Under compression, this indicates that void spaces are being collapsed instead of material expanding outward as manifested by an increase in the lateral strain. Once the sample reaches a peak strain of 0.01483 in S-SP2, D_ν rapidly increases as the strain decreases, which suggests that there is now significant void growth in the sample. In another example, Z-S3 shows the opposite sort of behavior, beginning with $D_\nu < -1$, which means that compression is causing inward rather than outward lateral strain and thus it can be assumed that there is an initial collapse of void spaces. In the Z-SP3 test, D_ν increases with increasing axial strain, but remains negative until peak strain is reached, at which point the sample undergoes rapid increase in D_ν during the unloading process. What these two series have in common is that even though they never reach $D_\nu = 0$ before peak stress, they are both trending in that direction, suggesting that the compression process is driving the two materials towards a baseline state before failure. The recovery of quasi-static baseline behavior from an initial extreme value has been seen previously in thermally shocked alumina[232]. For the intermediate strain rate grouping of 400 ± 100 s^{-1} (Figure 5-6, panel B), some of the series exhibit initial D_ν greater than 0.5 or lower than -0.5, but none are as pronounced as the S-SP2 and Z-SP3 experiments. The significant behavior here is how multiple samples demonstrate abrupt drops in D_ν that occurs a few measurement points before peak before then having extreme positive D_ν values during the unloading phase (after peak strain), a behavior seen in other advanced ceramics such as alumina and silicon carbide[175]. Prominent examples of this behavior can be seen in Figure 5-6, Panel B are Z-LP3 and S-LP2, which are labelled 3 and 4, respectively. For the lowest dynamic strain rates of 200 ± 30 s^{-1} (Figure 5-6, Panel C), a decrease in D_v before peak strain followed by an extreme increase in D_v at failure is the dominant behavior. The most extreme of these is S-LTP3, labelled 5 in Figure 5-6, Panel C. Along with Z-LP3 and S-LP2, these tests all show $D_v < -1$ before failure and then $D_v > 2$ during failure. A notable exception to this trend is sample S-LTP1, which shows no significant change in D_v before reaching failure at peak strain. This means that S-LTP1 demonstrated no sign of significant bulking, which is notable since it also demonstrated D_E behavior similar to models which do not consider bulking a significant factor[57–59].

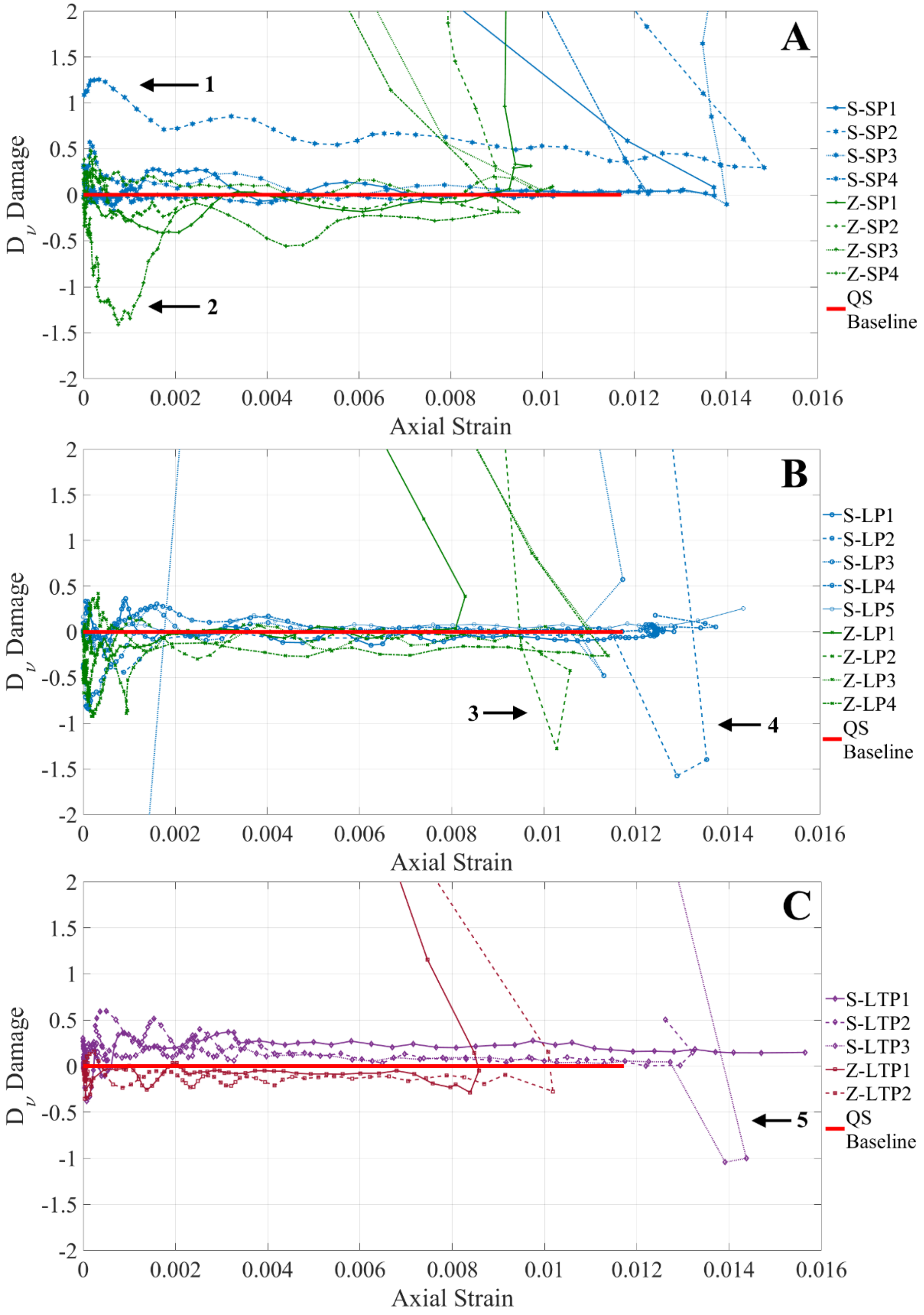

Figure 5-6 - D_ν vs. strain for short projectile with polyethylene pulse shaper tests 1000 ± 200 s^{-1} (top, panel A), long projectile with polyethylene pulse shaper tests 400 ± 100 s^{-1} (middle, panel B) and long projectile with tin pulse shaper tests 200 ± 20 s^{-1} (bottom, panel C). The quasi-static tests for the S-series are summarized as a single linear line that shows how dynamic conditions cause deviation from linear elastic behavior. Tests that show large and persistent initial deviations in D_ν in Panel A are labelled as 1 for S-SP2 and 2 for Z-SP3. Z-LP3, S-LP2, and S-LTP3 are all labelled as 3, 4, and 5, respectively, and show tests that prominently feature abrupt drops in D_ν to below -1 right before rapid increase in D_ν during the unloading process.

5.3.3.3. *Shear Modulus Damage Evolution with Axial Strain*

Figure 5-7 shows the D_G shear modulus damage vs. axial strain for the S and Z boron carbide series undergoing dynamic uniaxial compression, divided into subfigures according to strain rate. For all strain-rates, the D_G value at ultimate failure is negative, as previously seen with intact and damaged alumina[232]. The significance of D_G vs. axial strain behavior is that after the peak strength is reached and the failure process begins, there are two ways for D_G to become negative. The first method is that D_E becomes negative, which is the form assumed by past models[26,57,59,100]. The other path for D_G to become negative is if D_ν increases. D_G can become negative while D_E is increasing so long as D_ν increases more quickly than D_E. From the observations seen in Figure 5-5 through Figure 5-7, the differences in behavior suggest that there is a competition of strain-rate dependent damage mechanisms, and at least two elastic property damage measures are required to understand the evolution of these mechanisms with strain and strain-rate, specifically the Poisson's ratio and shear modulus. These implied behaviors are examined more thoroughly in Section 3.4 and discussed in Section 5.4, Discussion.

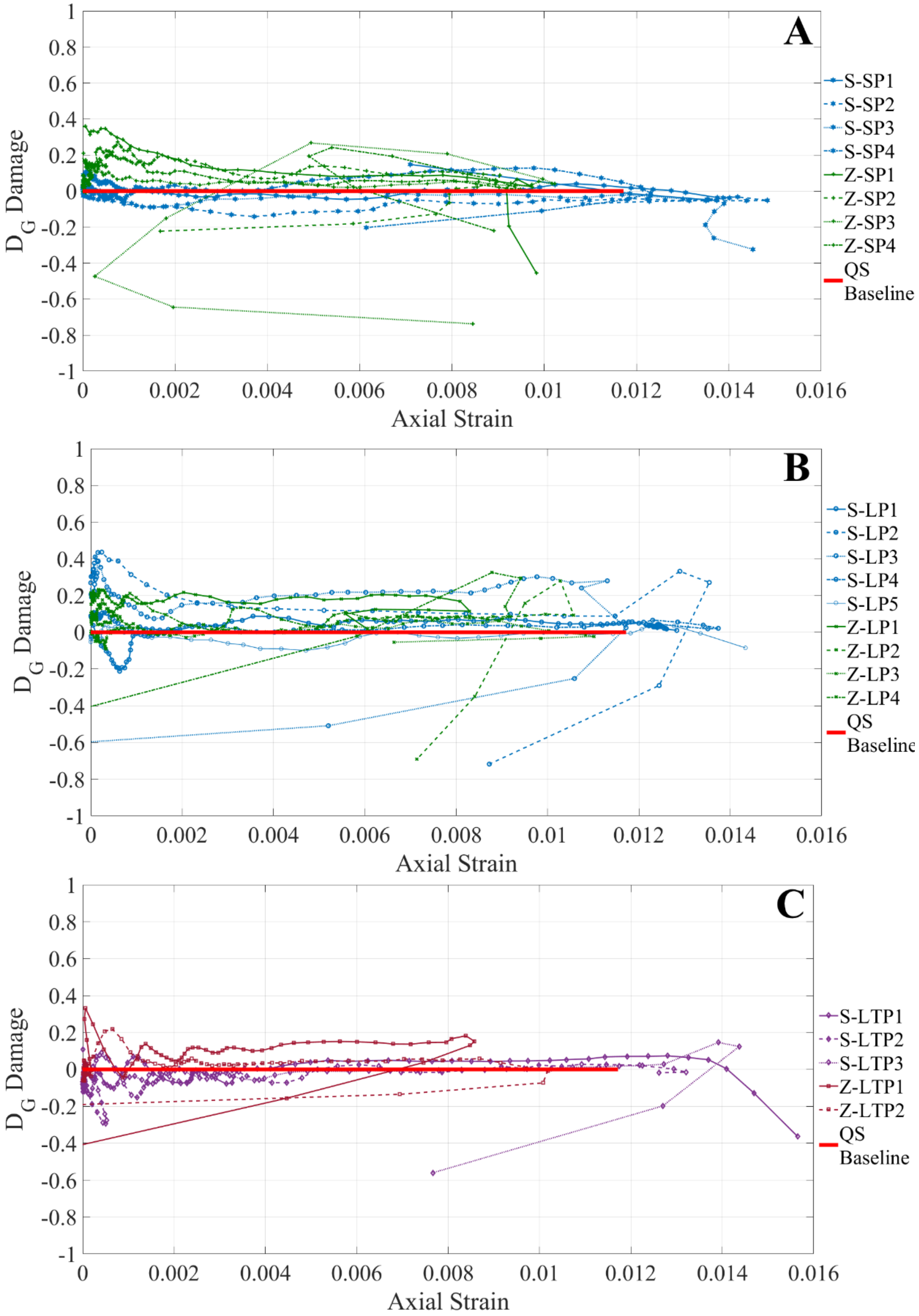

Figure 5-7 - D_G vs. strain for short projectile with polyethylene pulse shaper tests 1000 ± 200 s^{-1} (top, panel A), long projectile with polyethylene pulse shaper tests 400 ± 100 s^{-1} (middle, panel B) and long projectile with tin pulse shaper tests 200 ± 20 s^{-1} (bottom, panel C)). The quasi-static tests for the S-series are summarized as a single linear line that shows how dynamic conditions cause deviation from linear elastic behavior.

5.3.4. Influence of Strain-Rate on Damage Evolution with Axial Strain

Figure 5-8 shows the three damage measures vs. axial strain for the lowest (S-LTP1) strain rate S-series sample, and Figure 5-9 shows the three damage measures vs. axial strain for the highest (S-SP1) strain rate S-series samples. These figures show how strain rate generally influences the damage evolution in the selected elastic properties. In particular, Figure 5-8 demonstrates that S-LTP1 shows no significant change to D_{ν} with strain, which means that D_E and D_G trace the same path, offset by a constant amount related to the damage to the Poisson's ratio. In fact, if ν_0 is taken to be 0.18 rather than 0.15 (the quasi-static value) for this test, there is no significant change in Poisson's ratio with strain. If there is no change in ν, then D_E and D_G are mathematically identical, as shown in Equation 7, derived from Equations 1, 3, and 6.

$$D_G = \left(\frac{G_{app}}{G_0} - 1\right) = \left(\frac{\frac{E_{app}}{2(1+\nu)}}{\frac{E_0}{2(1+\nu)}} - 1\right) = \left(\frac{E_{app}}{E_0} - 1\right) = D_E \tag{7}$$

For S-LTP1, there is also no significant damage (degradation of Young's modulus, Poisson's ratio, or shear modulus) apparent up to the peak stress. At peak stress, D_E and D_G undergo a monotonic and linear decrease. This pattern is exactly what is predicted in past damage accumulation theories[57–59], with the theories having originally been derived from quasi-static testing observations[203,238–240].

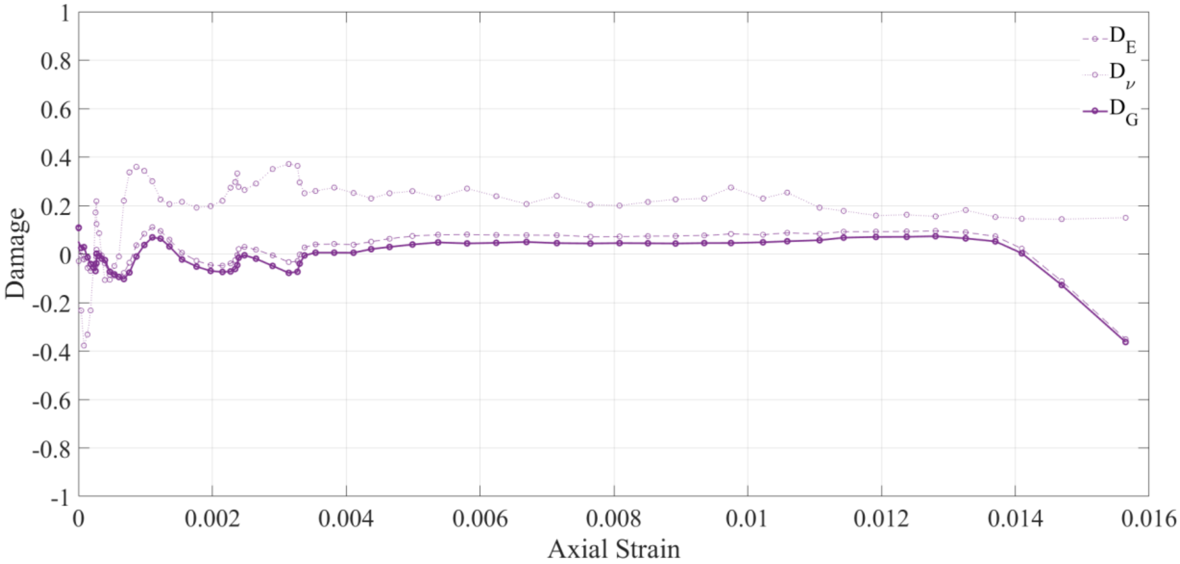

Figure 5-8 – D_E, D_ν, and D_G damage for S-LTP1 plotted vs. axial strain, showing the lowest strain rate test in the S-series at 200 s^{-1}. The figure demonstrates that D_G and D_E overlap near exactly, and if *E* and *ν* are adjusted such that they use values derived from this test rather than quasi-static values then the test shows no damage accumulation in any of the values up to 0.0137 strain (peak stress), at which point D_G and D_E both begin to decrease simultaneously.

By contrast, Figure 5-9 shows the damage vs. axial strain measures for the S-SP1 sample, which is at a higher strain rate of 1100 s^{-1} than S-LTP1 at 200 s^{-1}. Here, D_E and D_G track each other up to the point of maximum strain, at which point they diverge as D_ν undergoes a rapid increase. While D_E increases as the axial strain decreases, D_G decreases and, thus, is believed to serve as a better indicator of damage under high strain rate loading conditions. Contrasting with Figure 5-8, Figure 5-9 suggests that at the lower strain rate, damage accumulation is a stable process that involves minor dilatancy, likely because only a single flaw, or few flaws, is (are) being activated and thus requires minimal additional volume to accommodate its growth[238,241,242]. However, as the strain rate increases, current damage accumulation theory suggests that more flaws are activated[17], producing a greater internal volume increase and thus a greater apparent Poisson's ratio. More flaws being activated also requires more new free surfaces to be generated, taking away strain energy[243–245]. Taken altogether, this suggests that S-LTP1 is undergoing quasi-static type failure, while S-SP1 is undergoing dynamic type failure.

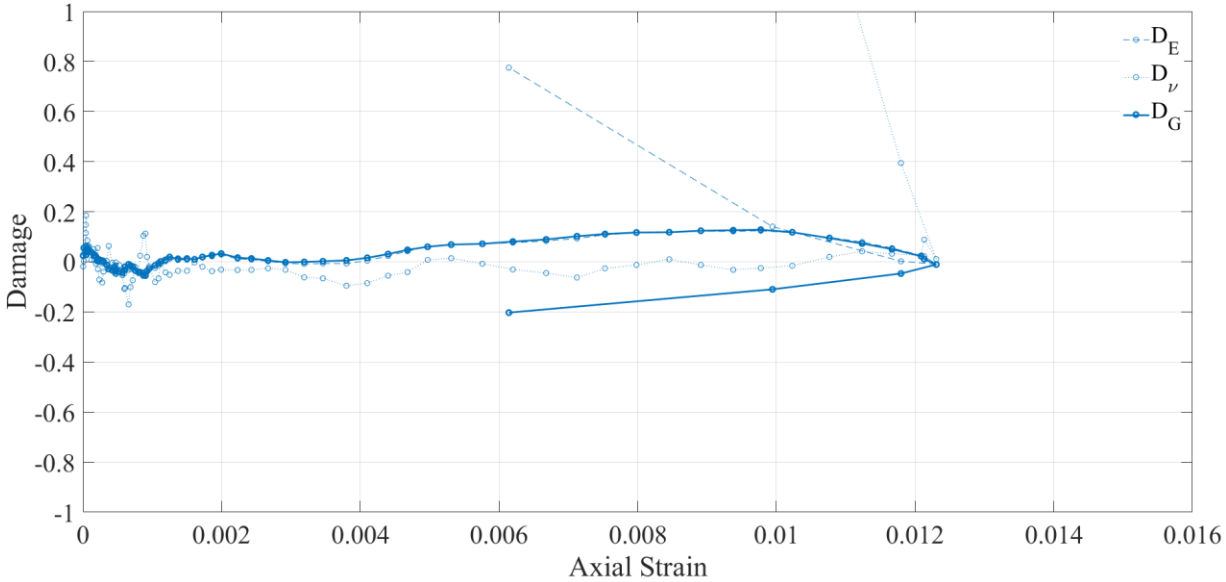

Figure 5-9 – D_E, D_ν, and D_G damage for S-SP1 plotted vs. axial strain, the highest strain rate test in the S-series at 1100 s^{-1}. D_G and D_E overlap up to the point of failure at maximum strain of 0.0123 strain, at which point they diverge due to the rapid increase of D_ν.

Evidence of the change in behavior from quasi-static-type to dynamic-type failure are found in the images of S-LTP1 and S-SP1 just before the loss of correlation, which are seen in Figure 5-10. In Figure 5-10 Panel A, the last image of S-LTP1 before the correlation is lost shows no surface damage, while in Figure 5-10 Panel B the last image of S-SP1 before the correlation is lost shows the presence of axial cracks. The presence of surface cracks in S-SP1 does not interfere with the correlation process, but it does contribute to the changes in apparent Poisson's ratio that lead to the loss of shear modulus.

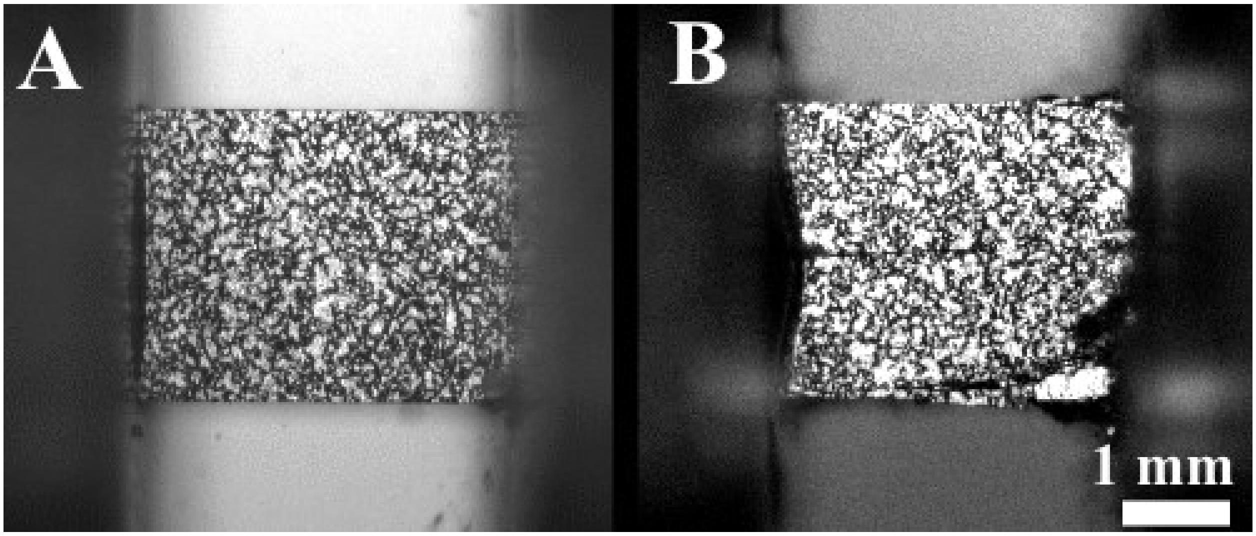

Figure 5-10 – Images of S-SLT1 (Panel A) and S-SP1 (Panel B) one frame before correlation of surface strains is lost due to surface cracking. S-SLT1 shows no signs of damage at the surface, while S-SP1 has cracks emerging at the edges of the sample and an axial crack running across the surface. This crack is insufficient to cause a loss of correlation in the DIC algorithm across the entire area of interest.

5.3.5. Quasi-Static to Dynamic-Type Failure Transition

Taking this new insight to re-examine Figure 5-5 through Figure 5-7 shows that both the S-series and Z-series have consistent damage vs. axial strain behaviors at the 1000 ± 200 s^{-1} strain rates (Panel A in all Figures), while the intermediate strain rate of 500 ± 100 s^{-1} (Panel B in all Figures) shows more anomalous behaviors, as indicated by arrows. At strain rates 200 ± 30 s^{-1} (Panel C in all Figures), the S-series shows a mixture of damage evolution behaviors. Given that the S-series is a purer material with a higher strength and stiffness than the Z-series[233], this suggests the possibility that these properties mediate at what strain rates a material transitions from quasi-static type failure to dynamic type failure. With the S-S1 and S-LT1 tests as upper and lower boundaries, the S-series likely has a transition zone between 10^2 and 10^3 s^{-1}, while the Z-series appears to have its transition zone less than 10^2 s^{-1}, as it exhibits consistent D_G driven shear modulus loss in the strain rates examined. The instability in behaviors for the S-series is likely due to different failure mechanisms being in competition at these strain rates, such that small differences in composition between samples can lead to a more quasi-static type failure or to a more dynamic type failure even at similar strain rates.

5.4. Discussion

This paper has presented new insights into the strain-rate sensitivities of damage accumulation in two types of boron carbide, a hot-pressed material (S-series) and a titanium diboride-boron carbide composite (Z-series). The key observations from the paper includes that the peak strength of the S-series is greater than the Z-series as seen in comparing to Table 5-2. From Figure 5-5 through Figure 5-7 it is also seen that the S-series has a later transition from quasi-static to dynamic failure. In the experiments, the quasi-static failure mode manifested as changes to primarily the Young's Modulus degradation (Figure 5-8), while the dynamic failure mode manifested as changes to both the Young's Modulus and the Poisson's ratio (Figure 5-9). In both quasi-static and dynamic failure modes, the shear modulus degradation was more indicative of the onset and evolution of compressive failure, and this motivates more detailed consideration for shear modulus evolution in modelling advanced ceramic materials. The implications of these outcomes are presented in this Discussion.

5.4.1. Current Understanding

Conventionally, previous models predicting the rate-dependent compressive failure of advanced ceramics[26,57–59] have assumed that the damage accumulates monotonically, only serves to degrade the Young's Modulus, and the functional form for damage accumulation is the same across all strain rates[26,57–59]. It is often assumed that completely damaged elements no longer participate in the continued mechanical response of the material [26,57,59], although some recent efforts[58,246,247] are being made to account for the transitions between intact and granular forms in models. With these assumptions, these models have been able to reasonably predict the strain-rate dependent strength of brittle materials[59,241,242]. These prior models were informed by the data that was available at the time[17,203,210,239,247,248], but until recently the data has been limited to end-state values such as the failure strength or strain, rather than the stress and strain data up to failure. Our experimental observations in this paper demonstrate that this conventional understanding is correct for quasi-static loading rates, but with new data on the intermediate failure states, we have seen that the assumptions derived from quasi-static behavior no longer hold in dynamic strain-rate loading regimes, an important outcome of this paper. On-going research in the literature have tried to understand the transitional behaviors between quasi-static and dynamic failure by investigating the evolution of the stress-strain response as a function of strain rate[249] instead of solely evaluating the peak stress vs. strain[38]. Our data can help generate new assumptions for modelling in these higher strain-rate regimes.

In the experiments in this paper, it is observed that the accumulation of damage occurs non-monotonically, primarily happens in the shear modulus for dynamic failure, and the surface strains in the samples (measured from DIC) are decreasing even as the stresses increase. This behavior is exemplified in the damage evolution plots seen in Figure 5-9. In the literature, previous models have primarily assumed elastic properties can only decrease through damage accumulation[57,59,246]. This is reasonable for brittle materials as cracking is an irreversible process [239] and so damage must accumulate in a monotonic fashion since cracks cannot be removed once they are present. In this paper, quasi-static failure was observed to exhibit monotonic damage accumulation. As an example, the D_G and D_E curves in Figure 5-8 show a continuously decreasing value past the peak stress. In brittle failure modelling [57,59,246], this behavior is captured through assumptions about a few isolated cracks being initiated, where their interactions are typically assumed to be structured (e.g., they all experience loading at each time step [57]). While these assumptions may be valid under quasi-static failure conditions, observations made in this paper in the dynamic failure regime (e.g., Figure 5) indicate that damage is non-monotonic (i.e., it can decrease and increase after, or vice-versa), and this is likely a consequence of the complex interactions during crack initiation, growth, and coalescence, which are also rate-dependent[238]. With many cracks being activated, the assumption of isolation and all cracking being treated equally at time/strain [57,58] may no longer hold. Under dynamic failure conditions, cracks may close [232], slide [195], open[99], grow [239], and interact [250], thus yielding complex temporal and spatial evolution through the material[238]. These behaviors will also depend on, for example, the orientation of the cracks to the loading direction and their size[177,232]. While this is a complex process, being able to model damage accumulation as either quasi-static-type or dynamic-type greatly simplifies modelling while still providing an overall increase in the accuracy and descriptiveness of the models.

5.4.2. Shear Failure

For the observation that damage primarily occurs in the shear modulus, this is also a strain-rate dependent phenomenon. During quasi-static failure conditions, the D_E and D_G values are observed to be equal (Figure 5-8). This is a consequence of there being no change to D_ν (Figure 5-8), indicating that bulking is not a significant contributor to quasi-static failure. The assumption that there is no change to ν is also common in models of brittle failure [57,59,246]. Under dynamic failure, it was observed that D_E and D_G diverged near peak stress, and this was driven by the increase in D_ν. Here, this evolution of D_ν (Figure 5-6) is a consequence of material bulking, which is the increase in internal volume needed to accommodate fracture behavior driven by crack closure, sliding, opening, growth, and interaction. In this paper, bulking is observed to manifest at the structural scale, and this serves to reduce the ability of the material to resist shear strains. Bulking [242] was observed in the dynamic experiments to manifest as a notable change in geometry via the formation of axial columns (Figure 5-10, Panel B), resulting in up to 3 times as much lateral strain as axial strain when correlation is lost in DIC (Figure 5-4). The change in geometry affects the global measure of stiffness, both in terms of DIC of local columns and the cross-sectional area of the load. The observed effect of the changes in geometry is an increase in the resistance of the material to uniaxial compressive deformation at the compromise of its ability to resist shear. This is supported by observations in this paper that Poisson's ratio increases rapidly above 5 during failure, and that surface cracking is observed in dynamic experiments before DIC is lost, as seen in Figure 5-10. While not confirmed, this also suggests that failure is occurring from the outside of the material to inwards, most likely to do with the geometry of the specimens. In the future, improved diagnostics (e.g., phase contrast imaging [251] and Photon Doppler Velocimetry [109,252]) will yield additional insights into the sequence of fracturing events that govern the quasi-static and dynamic behaviors of brittle materials.

Finally, the fact that the Z-series does not show a change from quasi-static-type failure to dynamic-type failure over the strain-rates studied (approximately 10^2 to 10^3 s^{-1}) suggests that the strain-rate range for the material is less than 10^2 s^{-1}. Past studies have suggested a transition point at approximately 10^0 s^{-1}[242]. Uncertainty as to exact behavior across strain-rates arises from the fact that quasi-static testing equipment is typically capable of strain-rates from 10^{-6} to 10^{-2} s^{-1}, while typical Kolsky bars achieve strain-rates of 10^2 to 10^4 s^{-1}[242]. Because the S-series has a higher quasi-static Young's modulus and failure strength than the Z-series, this suggests that the transition strain-rate from quasi-static to dynamic failure is governed by some intrinsic material property such as stiffness, strength, fracture toughness, or crack propagation speed[241,242] (which is governed by wave speed[253], which in turn relates to elastic properties and material density). The presence of a transition in damage accumulation behavior has been previously unexpected, but fits in with prior observations and provides new insights into the physical process of failure and fracture of brittle materials.

5.5. Conclusion

In this study, quasi-static and dynamic compression testing was performed on two different grades of boron carbide, one a high purity hot pressed boron carbide (S-series) and the other a boron carbide-titanium diboride ceramic composite (Z-series). The quasi-static testing revealed no new insights, but the dynamic compression testing incorporated DIC into the process and spanned between 10^2 and 10^3 s^{-1} strain rates and provided important new insights into dynamic failure mechanisms for advanced ceramics. At lower strain-rates, the S-series shows little to no changes to Poisson's ratio during the loading process, while the Z-series and high strain-rate S-series show large increases to Poisson's ratio as the strain increases. For all tests, the apparent shear modulus is below its quasi-static value at the point of failure, but the driver of this decrease varies depending upon the strain-rate. At lower strain-rates the shear modulus decrease is caused by an apparent decrease in the Young's modulus, while at higher strain-rates the shear modulus decrease is driven by an increase in the apparent Poisson's ratio. The apparent Young's modulus can even increase at higher strain-rates, but the shear modulus consistently decreases. This suggests that the elastic properties that respond to damage accumulation in brittle materials are the shear modulus and the Poisson's ratio, with the apparent Young's modulus being a function of those two properties. The data suggests that there is a transition zone from quasi-static-type failure where bulking is not a significant factor to dynamic-type failure where bulking is a significant factor. That the S-series shows this transition in behavior but the Z-series does not suggests that the transition point is related to a property such as stiffness or ultimate failure strength, as these properties are greater under quasi-static conditions for the S-series than the Z-series. The transition point for most advanced ceramics likely lies within the infrequently studied zone of 10^{-1} to 10^{1} strain-rate.

Chapter 6 – Conclusion

This thesis has focused on studying the mechanics of brittle material failure, with particular emphasis on advanced ceramics. The primary areas of study have been on the characterization of the microstructure of alumina; and the mechanical response of alumina, silicon carbide, boron carbide, and the TitanMade® cermet. The experiments involved in the study of damage accumulation and mechanical properties of ceramics were:

- Characterization using scanning electron microscopy, electron backscatter diffraction, and energy dispersive X-ray spectroscopy. These techniques were used to assess the microstructural properties of AD-85 and AD-995 alumina. Detailed information on grain sizes, chemical compositions of grains and defects, and defect sizes and spacing was obtained.
- Impact experiments were used to examine the impact behavior of alumina tiles. By coupling together high-speed photography, flash X-ray photography, and photon-Doppler velocimetry, the impact event could be observed with sub-microsecond temporal resolution.
- Quasi-static and dynamic Kolsky bar compression experiments with DIC for pristine AD-85, AD-995, silicon carbide, and boron carbide. AD-995 was also pre-damaged via thermal shocking. These experiments were used to examine how damage accumulated under uniform compressive loading.

6.1. Contributions

From the work performed in this thesis the contributions are:

- AD-85 alumina has smaller alumina grains than AD-995, a feature normally associated with greater strength and fracture toughness for ceramics. The presence of amorphous silica, large pores, and chemical impurities within AD-85 resulted in the material having a lower Young's modulus, failure strength, and less resistance to failure during impact with a projectile. This reinforces previous findings in the literature that continuity of material is more important than grain size[33,35,65,67,69], and additionally provides a material with these microstructural properties to compare and contrast with more chemically uniform ceramics.

- Kolsky bar experiments showed that materials increased their failure strength in comparison to quasi-static conditions as expected[38,50,77,93]. However, changes in microstructure such as the increased porosity of AD-85 versus AD-995 or pre-damage via thermal shocking for AD-995 produced a complex change in stress-strain and axial-lateral responses that manifested in non-linear and non-monotonic patterns. These responses were not behaviors expected by previous theory[57–59].
- The translation of compression stresses into shear stresses and how the material responds to shear is a critical component of the brittle failure process. First seen in this thesis in the wave front interactions between the projectile and target in the PDV traces of impact experiments in Chapter 2, and subsequently seen in the way the apparent shear modulus accumulates damage in compression experiments with DIC in Chapter 4. This is a novel discovery and provides new avenues for future experimental design, improving simulation fidelity, and methods of armor design.
- From Chapter 3 onward, experiments found that apparent mechanical damage is both non-linear and non-monotonic with strain in quasi-static and dynamic compression experiments. This behavior was previously not considered in the literature[26,36,55].
- Using past damage accumulation models as a starting point[26,36,55], the work incorporated changes to Poisson's ratio as a damage factor. Tracking Poisson's ratio damage and Young's modulus damage together also allowed for other elastic moduli such as shear modulus to be tracked. Shear and shear modulus plays a central role in the compressive and impact failure of brittle materials. A key recommendation is that failure models should account for changes to shear modulus rather than only considering Young's modulus. Processes such as pore collapse and crack closure allow for brittle materials to recover stiffness, but these phenomena reduce resistance to ultimate failure.

6.2. Future Work

Future work stemming from this research can be categorized as:

- Design simulations to incorporate bulking by modifying damage equations to use changes to Poisson's ratio and shear modulus rather than only Young's modulus, with the intention of replicating the stress-strain and axial-lateral behaviors observed in experiments.
- Perform further impact experiments at higher and lower velocities and with different ceramic materials in order to explore how different damage accumulation behaviors influences impact resistance at different input energies. Use modified Kolsky bar experiments to produce uniform shear loading in order to test if the shear modulus will change when subjected to shear load rather than a compressive load. Use 3D printing to produce samples with specified internal porosity and structures to generate controlled internal initial damage states for the purposes of better understanding damage accumulation for pre-damage materials.

References

[1] V.R. Shea, D.R. Hanson, Elastic Wave Velocity and Attenuation as Used to Define Phases of Loading and Failure in Coal, Int. J. Rock Mech. Min. Sci. 25 (1988) 431–437.

[2] K.T. Ramesh, A.M. Stickle, J. Kimberley, Rocks, Shocks and Asteroids, and Some Interesting Research Directions in Mechanics: 2015 Murray Lecture Paper, Exp. Mech. (2017). https://doi.org/10.1007/s11340-017-0324-9.

[3] I.G. Crouch, Body armour – New materials, new systems, Def. Technol. (2019). https://doi.org/10.1016/j.dt.2019.02.002.

[4] D.A. Shockey, A.H. Marchand, S.R. Skaggs, G.E. Cort, M.W. Burkett, R. Parker, Failure Phenomenology of Confined Ceramic Targets and Impacting Rods, Int. J. Impact Eng. 9 (1990) 263–275.

[5] M.L. Wilkins, Mechanics of penetration and perforation, Int. J. Eng. Sci. 16 (1978) 793–807.

[6] M. Wilkins, C. Honodel, D. Sawle, APPROACH TO THE STUDY OF LIGHT ARMOR., California Univ., Livermore. Lawrence Radiation Lab., 1967. https://www.osti.gov/scitech/servlets/purl/4308612 (accessed June 27, 2017).

[7] M.L. Wilkins, C.F. Cline, C.A. Honodel, Fourth Progress Report of Light Armor Program, California University, Lawrence Radiation Lab, 1969.

[8] W.W. Chen, A.M. Rajendran, B. Song, X. Nie, Dynamic Fracture of Ceramics in Armor Applications, J. Am. Ceram. Soc. 90 (2007) 1005–1018. https://doi.org/10.1111/j.1551-2916.2007.01515.x.

[9] J.D. Clayton, Penetration resistance of armor ceramics: Dimensional analysis and property correlations, Int. J. Impact Eng. 85 (2015) 124–131. https://doi.org/10.1016/j.ijimpeng.2015.06.025.

[10] T.J. Moynihan, S.-C. Chou, A.L. Mihalcin, Application of the Depth-of-Penetration Test Methodology to Characterize Ceramics for Personnel Protection:, Defense Technical Information Center, Fort Belvoir, VA, 2000. https://doi.org/10.21236/ADA376698.

[11] F. Cui, G. Wu, T. Ma, W. Li, Effect of Ceramic Properties and Depth-of-penetration Test Parameters on the Ballistic Performance of Armour Ceramics, Def. Sci. J. 67 (2017) 260. https://doi.org/10.14429/dsj.67.10664.

[12] H.M. Ghomi, A.G. Odeshi, The effects of microstructure, strain rates and geometry on dynamic impact response of a carbon–manganese steel, Mater. Sci. Eng. A. 532 (2012) 308–315. https://doi.org/10.1016/j.msea.2011.10.096.

[13] A.G. Odeshi, M.N. Bassim, High strain-rate fracture and failure of a high strength low alloy steel in compression, Mater. Sci. Eng. A. 525 (2009) 96–101. https://doi.org/10.1016/j.msea.2009.07.026.

[14] A.G. Odeshi, S. Al-ameeri, M.N. Bassim, Effect of high strain rate on plastic deformation of a low alloy steel subjected to ballistic impact, J. Mater. Process. Technol. 162–163 (2005) 385–391. https://doi.org/10.1016/j.jmatprotec.2005.02.157.

[15] G. Owolabi, D. Odoh, A. Odeshi, H. Whitworth, Occurrence of Dynamic Shear Bands in AISI 4340 Steel under Impact Loads, World J. Mech. 03 (2013) 139–145. https://doi.org/10.4236/wjm.2013.32011.

[16] D.R. Curran, L. Seaman, T. Cooper, D.A. Shockey, Micromechanical model for comminution and granular flow of brittle material under high strain rate application to penetration of ceramic targets, Int. J. Impact Eng. 13 (1993) 53–83.

[17] J.D. Hogan, L. Farbaniec, N. Daphalapurkar, K.T. Ramesh, On Compressive Brittle Fragmentation, J. Am. Ceram. Soc. 99 (2016) 2159–2169. https://doi.org/10.1111/jace.14171.

[18] A. Krell, E. Strassburger, Order of influences on the ballistic resistance of armor ceramics and single crystals, Mater. Sci. Eng. A. 597 (2014) 422–430. https://doi.org/10.1016/j.msea.2013.12.101.

[19] A. Krell, E. Strassburger, T. Hutzler, J. Klimke, Single and Polycrystalline Transparent Ceramic Armor with Different Crystal Structure, J. Am. Ceram. Soc. 96 (2013) 2718–2721. https://doi.org/10.1111/jace.12530.

[20] D.E. Grady, Shock-wave compression of brittle solids, Mech. Mater. 29 (1998) 181–203.

[21] J. Kimberley, K.T. Ramesh, N.P. Daphalapurkar, A scaling law for the dynamic strength of brittle solids, Acta Mater. 61 (2013) 3509–3521. https://doi.org/10.1016/j.actamat.2013.02.045.

[22] J.D. Hogan, J. Kimberley, K. Hazeli, J. Plescia, K.T. Ramesh, Dynamic behavior of an ordinary chondrite: The effects of microstructure on strength, failure and fragmentation, Icarus. 260 (2015) 308–319. https://doi.org/10.1016/j.icarus.2015.07.027.

[23] G.E. Hauver, E.J. Rapacki, Jr., P.H. Netherwood, R.F. Benck, Interface Defeat of Long-Rod Projectiles by Ceramic Armor, (2005).

[24] T. Behner, A. Heine, M. Wickert, Dwell and penetration of tungsten heavy alloy long-rod penetrators impacting unconfined finite-thickness silicon carbide ceramic targets, Int. J. Impact Eng. 95 (2016) 54–60. https://doi.org/10.1016/j.ijimpeng.2016.04.008.

[25] D.L. Orphal, R.R. Franzen, A.C. Charters, T.L. Menna, A.J. Piekutowski, Penetration of Confined Boron Carbide Targets by Tungsten Long Rods at Impact Velocities from 1.5 to 5.0 km/s, Int. J. Impact Eng. 19 (1997) 15–29.

[26] G.R. Johnson, T.J. Holmquist, An improved computational constitutive model for brittle materials, in: AIP Conf. Proc., AIP, Colorado Springs, Colorado (USA), 1994: pp. 981–984. https://doi.org/10.1063/1.46199.

[27] F. Longy, J. Cagnoux, Plasticity and Microcracking in Shock-Loaded Alumina, J. Am. Ceram. Soc. 72 (1989) 971–979.

[28] A.K. Mukhopadhyay, K.D. Joshi, A. Dey, R. Chakraborty, A. Rav, S.K. Biswas, S.C. Gupta, Shock deformation of coarse grain alumina above Hugoniot elastic limit, J. Mater. Sci. 45 (2010) 3635–3651. https://doi.org/10.1007/s10853-010-4409-4.

[29] D.E. Munson, R.J. Lawrence, Dynamic deformation of polycrystalline alumina, J. Appl. Phys. 50 (1979) 6272–6282. https://doi.org/10.1063/1.325766.

[30] J. Ning, H. Ren, T. Guo, P. Li, Dynamic response of alumina ceramics impacted by long tungsten projectile, Int. J. Impact Eng. 62 (2013) 60–74. https://doi.org/10.1016/j.ijimpeng.2013.06.006.

[31] J.M. Staehler, W.W. Predebon, B.J. Pletka, G. Subhash, Micromechanisms of deformation in high-purity hot-pressed alumina, Mater. Sci. Eng. A. 291 (2000) 37–45.

[32] T.L. Jones, C.S. Meredith, B. Becker, First static and dynamic analysis of 3-D-printed sintered ceramics for body armor applications, Am. Ceram. Soc. Bull. 96 (2017) 36–41.

[33] A. Arab, R. Ahmad, Z.A. Ahmad, Effect of SrCO3 addition on the dynamic compressive strength of ZTA, Int. J. Miner. Metall. Mater. 23 (2016) 481–489. https://doi.org/10.1007/s12613-016-1259-3.

[34] S. Li, C.-A. Wang, J. Zhou, Effect of starch addition on microstructure and properties of highly porous alumina ceramics, Ceram. Int. 39 (2013) 8833–8839. https://doi.org/10.1016/j.ceramint.2013.04.072.

[35] R.L. Landingham, A.W. Casey, Final Report of the Light Armor Materials Program, Lawrence Livermore Natl. Lab. UCRL-51269. (1972). http://www.iaea.org/inis/collection/NCLCollectionStore/_Public/04/068/4068133.pdf (accessed June 23, 2017).

[36] G. Hu, J. Liu, L. Graham-Brady, K.T. Ramesh, A 3D mechanistic model for brittle materials containing evolving flaw distributions under dynamic multiaxial loading, J. Mech. Phys. Solids. 78 (2015) 269–297. https://doi.org/10.1016/j.jmps.2015.02.014.

[37] J.D. Hogan, L. Farbaniec, D. Mallick, V. Domnich, K. Kuwelkar, T. Sano, J.W. McCauley, K.T. Ramesh, Fragmentation of an advanced ceramic under ballistic impact: Mechanisms and microstructure, Int. J. Impact Eng. 102 (2017) 47–54. https://doi.org/10.1016/j.ijimpeng.2016.12.008.

[38] S. Nemat-Nasser, H. Deng, STRAIN-RATE EFFECT ON BRITTLE FAILURE in Compression, Acta Metall. Mater. 42 (1994) 1013–1024.

[39] E. Strassburger, Visualization of Impact Damage in Ceramics Using the Edge-On Impact Technique, Int. J. Appl. Ceram. Technol. 1 (2004) 235–242.

[40] E. Strassburger, High-Speed Photographic Study of Wave Propagation and Impact Damage in Transparent Aluminum Oxynitride (AION), DTIC Document, 2006. http://oai.dtic.mil/oai/oai?verb=getRecord&metadataPrefix=html&identifier=ADA457205 (accessed September 26, 2016).

[41] E. Strassburger, P. Patel, J.W. McCauley, C. Kovalchick, K.T. Ramesh, D.W. Templeton, High-speed transmission shadowgraphic and dynamic photoelasticity study of stress wave and impact damage propagation in transparent materials and laminates using the edge-on impact (EOI) method, DTIC Document, 2008. http://oai.dtic.mil/oai/oai?verb=getRecord&metadataPrefix=html&identifier=ADA479090 (accessed September 26, 2016).

[42] E. Strassburger, P. Patel, J.W. McCauley, Visualization and analysis of impact damage in sapphire, DTIC Document, 2011. http://oai.dtic.mil/oai/oai?verb=getRecord&metadataPrefix=html&identifier=ADA556724 (accessed September 26, 2016).

[43] E. Strassburger, S. Bauer, G. Popko, Damage visualization and deformation measurement in glass laminates during projectile penetration, Def. Technol. 10 (2014) 226–238. https://doi.org/10.1016/j.dt.2014.05.008.

[44] B. Aydelotte, B. Schuster, Impact and Penetration of SiC: The Role of Rod Strength in the Transition from Dwell to Penetration, Procedia Eng. 103 (2015) 19–26. https://doi.org/10.1016/j.proeng.2015.04.004.

[45] W.F. Brace, E.G. Bombolakis, A note on brittle crack growth in compression, J. Geophys. Res. 68 (1963) 3709–3713.

[46] S. Nemat-Nasser, H. Horii, ROCK FAILURE IN COMPRESSION, Int. J. Eng. Sci. 22 (1984) 999–1011.

[47] H. Horii, S. Nemat-Nasser, Compression-Induced Microcrack Growth in Brittle Solids, J. Geophys. Res. 90 (1985) 3105–3125.

[48] H. Horii, S. Nemat-Nasser, Compression-induced Nonplanar Crack Extension, J. Geophys. Res. 87 (1982) 6805–6821.

[49] A.L. Tonge, A Unified Framework Which Uses Multi-Scale Microstructural Information for Modelling Dynamic Failure in Brittle Materials, The Johns Hopkins University, 2014.

[50] A.L. Tonge, J. Kimberley, K.T. Ramesh, A Consistent Scaling Framework for Simulating High Rate Brittle Failure Problems, Procedia Eng. 58 (2013) 692–701. https://doi.org/10.1016/j.proeng.2013.05.080.

[51] J.D. Clayton, A.L. Tonge, A nonlinear anisotropic elastic–inelastic constitutive model for polycrystalline ceramics and minerals with application to boron carbide, Int. J. Solids Struct. 64–65 (2015) 191–207. https://doi.org/10.1016/j.ijsolstr.2015.03.024.

[52] K.T. Ramesh, J.D. Hogan, J. Kimberley, A. Stickle, A review of mechanisms and models for dynamic failure, strength, and fragmentation, Planet. Space Sci. 107 (2015) 10–23. https://doi.org/10.1016/j.pss.2014.11.010.

[53] L. Farbaniec, J.D. Hogan, K.Y. Xie, M. Shaeffer, K.J. Hemker, K.T. Ramesh, Damage evolution of hot-pressed boron carbide under confined dynamic compression, Int. J. Impact Eng. 99 (2017) 75–84. https://doi.org/10.1016/j.ijimpeng.2016.09.008.

[54] G. Hu, The failure of brittle materials under dynamic multiaxial loading, The Johns Hopkins University, 2012.

[55] B. Paliwal, K.T. Ramesh, An interacting micro-crack damage model for failure of brittle materials under compression, J. Mech. Phys. Solids. 56 (2008) 896–923. https://doi.org/10.1016/j.jmps.2007.06.012.

[56] S. Nemat-Nasser, M. Obata, A microcrack model of dilatancy in brittle materials, J Appl Mech. 55 (1988) 24–35.

[57] B. Paliwal, K.T. Ramesh, An interacting micro-crack damage model for failure of brittle materials under compression, J. Mech. Phys. Solids. 56 (2008) 896–923. https://doi.org/10.1016/j.jmps.2007.06.012.

[58] A.L. Tonge, A Unified Framework Which Uses Multi-Scale Microstructural Information for Modelling Dynamic Failure in Brittle Materials, The Johns Hopkins University, 2014.

[59] G. Hu, J. Liu, L. Graham-Brady, K.T. Ramesh, A 3D mechanistic model for brittle materials containing evolving flaw distributions under dynamic multiaxial loading, J. Mech. Phys. Solids. 78 (2015) 269–297. https://doi.org/10.1016/j.jmps.2015.02.014.

[60] C. Lo, T. Sano, J.D. Hogan, Microstructural and mechanical characterization of variability in porous advanced ceramics using X-ray computed tomography and digital image correlation, Mater. Charact. 158 (2019) 109929. https://doi.org/10.1016/j.matchar.2019.109929.

[61] D.J. Frew, M.J. Forrestal, W. Chen, A split Hopkinson pressure bar technique to determine compressive stress-strain data for rock materials, Exp. Mech. 41 (2001) 40–46.

[62] B. Paliwal, K.T. Ramesh, Effect of crack growth dynamics on the rate-sensitive behavior of hot-pressed boron carbide, Scr. Mater. 57 (2007) 481–484. https://doi.org/10.1016/j.scriptamat.2007.05.028.

[63] G. Hu, C.Q. Chen, K.T. Ramesh, J.W. McCauley, Dynamic multiaxial response of a hot-pressed aluminum nitride, Scr. Mater. 66 (2012) 527–530. https://doi.org/10.1016/j.scriptamat.2011.12.037.

[64] H. Wang, K.T. Ramesh, Dynamic strength and fragmentation of hot-pressed silicon carbide under uniaxial compression, Acta Mater. 52 (2004) 355–367. https://doi.org/10.1016/j.actamat.2003.09.036.

[65] N.A. Rejab, A.Z.A. Azhar, M.M. Ratnam, Z.A. Ahmad, The effects of CeO2 addition on the physical, microstructural and mechanical properties of yttria stabilized zirconia

toughened alumina (ZTA), Int. J. Refract. Met. Hard Mater. 36 (2013) 162–166. https://doi.org/10.1016/j.ijrmhm.2012.08.010.

[66] H. Manshor, S. Md Aris, A.Z.A. Azhar, E.C. Abdullah, Z.A. Ahmad, Effects of TiO2 addition on the phase, mechanical properties, and microstructure of zirconia-toughened alumina ceramic composite, Ceram. Int. 41 (2015) 3961–3967. https://doi.org/10.1016/j.ceramint.2014.11.080.

[67] N.A. Rejab, A.Z.A. Azhar, K.S. Kian, M.M. Ratnam, Z.A. Ahmad, Effects of MgO addition on the phase, mechanical properties, and microstructure of zirconia-toughened alumina added with CeO2 (ZTA–CeO2) ceramic composite, Mater. Sci. Eng. A. 595 (2014) 18–24. https://doi.org/10.1016/j.msea.2013.11.091.

[68] M. Schwentenwein, J. Homa, Additive Manufacturing of Dense Alumina Ceramics, Int. J. Appl. Ceram. Technol. 12 (2015) 1–7. https://doi.org/10.1111/ijac.12319.

[69] T.L. Jones, C.S. Meredith, B. Becker, First static and dynamic analysis of 3-D-printed sintered ceramics for body armor applications, Am. Ceram. Soc. Bull. 96 (2017) 36–41.

[70] L.R. Meza, S. Das, J.R. Greer, Strong, lightweight, and recoverable three-dimensional ceramic nanolattices, Science. 345 (2014) 1322–1326.

[71] D.J. Frew, M.J. Forrestal, W. Chen, Pulse shaping techniques for testing brittle materials with a split hopkinson pressure bar, Exp. Mech. 42 (2002) 14.

[72] P. Jannotti, R. Doney, B. Schuster, Time-Resolved Measurement of Deformation of Metal Plates Due to High-Velocity Impacts, Procedia Eng. 204 (2017) 276–283. https://doi.org/10.1016/j.proeng.2017.09.737.

[73] B. Aydelotte, B. Schuster, Impact and Penetration of SiC: The Role of Rod Strength in the Transition from Dwell to Penetration, Procedia Eng. 103 (2015) 19–26. https://doi.org/10.1016/j.proeng.2015.04.004.

[74] O.T. Strand, D.R. Goosman, C. Martinez, T.L. Whitworth, W.W. Kuhlow, Compact system for high-speed velocimetry using heterodyne techniques, Rev. Sci. Instrum. 77 (2006) 083108. https://doi.org/10.1063/1.2336749.

[75] D.H. Dolan, Accuracy and precision in photonic Doppler velocimetry, Rev. Sci. Instrum. 81 (2010) 053905. https://doi.org/10.1063/1.3429257.

[76] D.G. Brandon, E.Y. Gutmanas, Z. Nissenholz, J. Ozeri, D. Shechtman, N. Travitzki, Y. Yeshurun, Strengthening of Alumina by Heat Treatment, Strength Met. Alloys ICSMA 6. (1982) 7.

[77] S. Acharya, S. Bysakh, V. Parameswaran, A. Kumar Mukhopadhyay, Deformation and failure of alumina under high strain rate compressive loading, Ceram. Int. 41 (2015) 6793–6801. https://doi.org/10.1016/j.ceramint.2015.01.126.

[78] J. Lankford, The role of dynamic material properties in the performance of ceramic armor, Int. J. Appl. Ceram. Technol. 1 (2004) 205–210.

[79] H. Gao, Surface roughening and branching instabilities in dynamic fracture, J. Mech. Phys. Solids. 41 (1993) 457–486. https://doi.org/10.1016/0022-5096(93)90044-G.

[80] K. Ravi-Chandar, W.G. Knauss, An experimental investigation into dynamic fracture: III. On steady-state crack propagation and crack branching, Int. J. Fract. 26 (1984) 141–154. https://doi.org/10.1007/BF01157550.

[81] Z.W. Yu, S. Tan, Z. Shan, X.Q. Tian, X-ray computed tomography quantification of damage in concrete under compression considering irreversible mode-II microcracks, Fatigue Fract. Eng. Mater. Struct. 40 (2017) 1960–1972.

[82] J.W. McCauley, E. Strassburger, P. Patel, B. Paliwal, K.T. Ramesh, Experimental Observations on Dynamic Response of Selected Transparent Armor Materials, Exp. Mech. 53 (2013) 3–29. https://doi.org/10.1007/s11340-012-9658-5.

[83] T. Børvik, M. Langseth, O.S. Hopperstad, K.A. Malo, Perforation of 12mm thick steel plates by 20mm diameter projectiles with flat, hemispherical and conical noses: part I: experimental study, Int. J. Impact Eng. 27 (2002) 19–35.

[84] C.C. Holland, E.A. Gamble, F.W. Zok, V.S. Deshpande, R.M. McMeeking, Effect of design on the performance of steel–alumina bilayers and trilayers subject to ballistic impact, Mech. Mater. 91 (2015) 241–251. https://doi.org/10.1016/j.mechmat.2015.05.002.

[85] E.A. Gamble, B.G. Compton, F.W. Zok, Impact response of layered steel–alumina targets, Mech. Mater. 60 (2013) 80–92. https://doi.org/10.1016/j.mechmat.2013.01.008.

[86] T. Behner, A. Heine, M. Wickert, Dwell and penetration of tungsten heavy alloy long-rod penetrators impacting unconfined finite-thickness silicon carbide ceramic targets, Int. J. Impact Eng. 95 (2016) 54–60. https://doi.org/10.1016/j.ijimpeng.2016.04.008.

[87] N.K. Bourne, Shock-induced brittle failure of boron carbide, Proc. R. Soc. Math. Phys. Eng. Sci. 458 (2002) 1999–2006. https://doi.org/10.1098/rspa.2002.0968.

[88] M. Chen, Shock-Induced Localized Amorphization in Boron Carbide, Science. 299 (2003) 1563–1566. https://doi.org/10.1126/science.1080819.

[89] D. Ghosh, G. Subhash, T.S. Sudarshan, R. Radhakrishnan, X.-L. Gao, Dynamic Indentation Response of Fine-Grained Boron Carbide, J. Am. Ceram. Soc. 90 (2007) 1850–1857. https://doi.org/10.1111/j.1551-2916.2007.01652.x.

[90] D. Ghosh, G. Subhash, C.H. Lee, Y.K. Yap, Strain-induced formation of carbon and boron clusters in boron carbide during dynamic indentation, Appl. Phys. Lett. 91 (2007) 061910. https://doi.org/10.1063/1.2768316.

[91] G. Subhash, D. Ghosh, J. Blaber, J.Q. Zheng, V. Halls, K. Masters, Characterization of the 3-D amorphized zone beneath a Vickers indentation in boron carbide using Raman spectroscopy, Acta Mater. 61 (2013) 3888–3896. https://doi.org/10.1016/j.actamat.2013.03.028.

[92] G. Subhash, S. Maiti, P.H. Geubelle, D. Ghosh, Recent Advances in Dynamic Indentation Fracture, Impact Damage and Fragmentation of Ceramics, J. Am. Ceram. Soc. 91 (2008) 2777–2791. https://doi.org/10.1111/j.1551-2916.2008.02624.x.

[93] S.M. Walley, Historical review of high strain rate and shock properties of ceramics relevant to their application in armour, Adv. Appl. Ceram. 109 (2010) 446–466. https://doi.org/10.1179/174367609X422180.

[94] T.J. Moynihan, J.C. LaSalvia, M.S. Burkins, Analysis of Shatter Gap Phenomenon in a Boron Carbide-Composite Laminate Armor System, in: Orlando, FL, 2002.

[95] S.J. Bless, Z. Rosenberg, B. Yoon, Hypervelocity Penetration of Ceramics, Int. J. Impact Eng. 5 (1987) 165–171.

[96] Z. Rozenberg, Y. Yeshurun, The relation between ballastic efficiency and compressive strength of ceramic tiles, Int. J. Impact Eng. 7 (1988) 357–362.

[97] J. Liu, L. Graham-Brady, Effective anisotropic compliance relationships for wing-cracked brittle materials under compression, Int. J. Solids Struct. 100–101 (2016) 151–168. https://doi.org/10.1016/j.ijsolstr.2016.08.012.

[98] R.S. Ayyagari, N.P. Daphalapurkar, K.T. Ramesh, The effective compliance of spatially evolving planar wing-cracks, J. Mech. Phys. Solids. 111 (2018) 503–529. https://doi.org/10.1016/j.jmps.2017.11.016.

[99] W.B. Bradley, A.S. Kobayashi, An investigation of propagating cracks by dynamic photoelasticity, Exp. Mech. 10 (1970) 106–113.

[100] A.L. Tonge, K.T. Ramesh, Application of the Tonge-Ramesh micromechanics based damage model to boron carbide under uniaxial compression and simplied ballistic loading, (2014).

[101] H. Deng, S. Nemat-Nasser, Microcrack Interaction and Shear Fault Failure, Int. J. Damage Mech. 3 (1994) 3–37. https://doi.org/10.1177/105678959400300101.

[102] C. Poinard, E. Piotrowska, Y. Malecot, L. Daudeville, E.N. Landis, Compression triaxial behavior of concrete: the role of the mesostructure by analysis of X-ray tomographic images, Eur. J. Environ. Civ. Eng. 16 (2012) s115–s136. https://doi.org/10.1080/19648189.2012.682458.

[103] C. Landron, O. Bouaziz, E. Maire, J. Adrien, Experimental investigation of void coalescence in a dual phase steel using X-ray tomography, Acta Mater. 61 (2013) 6821–6829. https://doi.org/10.1016/j.actamat.2013.07.058.

[104] I.A. Bannikova, O.B. Naimark, S.V. Uvarov, Transition from multi-center fracture to fragmentation statistics under intensive loading, in: Procedia Structural Integrity, 2016: pp. 1944–1950.

[105] T.J. Holmquist, G.R. Johnson, C.A. Gerlach, An improved computational constitutive model for glass, Philos. Trans. R. Soc. Math. Phys. Eng. Sci. 375 (2017) 20160182. https://doi.org/10.1098/rsta.2016.0182.

[106] R.L. Woodward, W.A. Gooch, R.G. O'Donnell, W.J. Perciballi, B.J. Baxter, S.D. Pattie, A study of fragmentation in the ballistic impact of ceramics, Int. J. Impact Eng. 15 (1994) 605–618.

[107] H. Li, P. Motamedi, J.D. Hogan, On the rate-dependency of mechanical properties and failure mechanisms of a (γ + α2) - TiAl/Ti3Al-Al2O3 cermet, Mater. Sci. Eng. A. 791 (2020) 139747. https://doi.org/10.1016/j.msea.2020.139747.

[108] J.D. Hogan, L. Farbaniec, M. Shaeffer, K.T. Ramesh, The Effects of Microstructure and Confinement on the Compressive Fragmentation of an Advanced Ceramic, J. Am. Ceram. Soc. 98 (2015) 902–912. https://doi.org/10.1111/jace.13353.

[109] B.M.L. Koch, P. Jannotti, D. Mallick, B. Schuster, T. Sano, J.D. Hogan, Influence of microstructure on the impact failure of alumina, Mater. Sci. Eng. A. 770 (2020) 138549. https://doi.org/10.1016/j.msea.2019.138549.

[110] Hy. Li, P. Motamedi, J.D. Hogan, Characterization and mechanical testing on novel (γ + α2) – TiAl/Ti3Al/Al2O3 cermet, Mater. Sci. Eng. A. 750 (2019) 152–163. https://doi.org/10.1016/j.msea.2019.02.039.

[111] B. Amirian, H. Li, J.D. Hogan, The Mechanical Response of a α2(Ti3Al)+γ(TiAl)-Nanograined Al2O3 Cermet Under Dynamic Compression: Modeling and Experiment, Acta Mater. (2019).

[112] CoorsTek, Advanced Alumina Materials & Manufacturing Processes Brochure, (2016). https://www.coorstek.com/media/1715/advanced-alumina-brochure.pdf.

[113] G.L. Harris, Properties of silicon carbide, 1995.

[114] J.J. Swab, G.D. Quinn, Dynamic Compression Strength of Ceramics: Results from an Interlaboratory Round-Robin Exercise, (2019) 58.

[115] W.W. Chen, B. Song, Split Hopkinson (Kolsky) Bar: Design, Testing, and Applications, Springer Science & Business Media, 2010.

[116] K. Xia, W. Yao, Dynamic rock tests using split Hopkinson (Kolsky) bar system – A review, J. Rock Mech. Geotech. Eng. 7 (2015) 27–59. https://doi.org/10.1016/j.jrmge.2014.07.008.

[117] W.W. Chen, A.M. Rajendran, B. Song, X. Nie, Dynamic Fracture of Ceramics in Armor Applications, J. Am. Ceram. Soc. 90 (2007) 1005–1018. https://doi.org/10.1111/j.1551-2916.2007.01515.x.

[118] N. Yang, J. Boselli, P.J. Gregson, I. Sinclair, Simulation and quantitative assessment of finite-size particle distributions in metal matrix composites, Mater. Sci. Technol. 16 (2000) 797–805. https://doi.org/10.1179/026708300101508469.

[119] A. Bastawros, Experimental analysis of deformation mechanisms in a closed-cell aluminum alloy foam, J. Mech. Phys. Solids. 48 (2000) 301–322. https://doi.org/10.1016/S0022-5096(99)00035-6.

[120] Analysis of a multiaxial test on a C/C composite by using digital image correlation and a damage model, (n.d.) 11.

[121] B. Wattrisse, A. Chrysochoos, J.-M. Muracciole, M. Némoz-Gaillard, Analysis of strain localization during tensile tests by digital image correlation, Exp. Mech. 41 (2001) 29–39. https://doi.org/10.1007/BF02323101.

[122] B. Pan, K. Qian, H. Xie, A. Asundi, Two-dimensional digital image correlation for in-plane displacement and strain measurement: a review, Meas. Sci. Technol. 20 (2009) 062001. https://doi.org/10.1088/0957-0233/20/6/062001.

[123] J. Kimberley, G. Hu, K.T. Ramesh, A Scaled Model Describing the Rate-Dependent Compressive Failure of Brittle Materials, in: T. Proulx (Ed.), Dyn. Behav. Mater. Vol. 1, Springer New York, New York, NY, 2011: pp. 419–421. http://link.springer.com/10.1007/978-1-4614-0216-9_57 (accessed October 3, 2016).

[124] P. Chantikul, S.J. Bennison, B.R. Lawn, Role of grain size in the strength and r-curve properties of alumina, J. Am. Ceram. Soc. 73 (1990) 2419–2427.

[125] D.P. Dandekar, P. Bartkowski, Shock response of AD995 alumina, in: AIP, 1994: pp. 733–736. https://doi.org/10.1063/1.46437.

[126] M. Guazzato, M. Albakry, S.P. Ringer, M.V. Swain, Strength, fracture toughness and microstructure of a selection of all-ceramic materials. Part I. Pressable and alumina glass-infiltrated ceramics, Dent. Mater. 20 (2004) 441–448. https://doi.org/10.1016/j.dental.2003.05.003.

[127] H. Luo, W. Chen, Dynamic Compressive Response of Intact and Damaged AD995 Alumina, Int. J. Appl. Ceram. Technol. 1 (2005) 254–260. https://doi.org/10.1111/j.1744-7402.2004.tb00177.x.

[128] G. Ravichandran, G. Subhash, A micromechanical model for high strain rate behavior of ceramics, Int. J. Solids Struct. 32 (1995) 2627–2646. https://doi.org/10.1016/0020-7683(94)00286-6.

[129] B. Paliwal, K.T. Ramesh, J.W. McCauley, M. Chen, Dynamic Compressive Failure of AlON Under Controlled Planar Confinement, J. Am. Ceram. Soc. 91 (2008) 3619–3629. https://doi.org/10.1111/j.1551-2916.2008.02712.x.

[130] T.J. Holmquist, G.R. Johnson, A Computational Constitutive Model for Glass Subjected to Large Strains, High Strain Rates and High Pressures, J. Appl. Mech. 78 (2011) 051003. https://doi.org/10.1115/1.4004326.

[131] Q. Rao, Z. Sun, O. Stephansson, C. Li, B. Stillborg, Shear fracture (Mode II) of brittle rock, Int. J. Rock Mech. Min. Sci. 40 (2003) 355–375. https://doi.org/10.1016/S1365-1609(03)00003-0.

[132] G. Ruiz, A. Pandolfi, M. Ortiz, Three-dimensional cohesive modeling of dynamic mixed-mode fracture, Int. J. Numer. Methods Eng. 52 (2001) 97–120. https://doi.org/10.1002/nme.273.

[133] G. Hu, The failure of brittle materials under dynamic multiaxial loading, The Johns Hopkins University, 2012.

[134] G. Hu, C.Q. Chen, K.T. Ramesh, J.W. McCauley, Mechanisms of dynamic deformation and dynamic failure in aluminum nitride, Acta Mater. 60 (2012) 3480–3490. https://doi.org/10.1016/j.actamat.2012.03.011.

[135] S. Bavdekar, G. Subhash, Comparison of pressure-sensitive strength models for ceramics under ultrahigh confinement, Int. J. Impact Eng. 118 (2018) 60–66. https://doi.org/10.1016/j.ijimpeng.2018.04.007.

[136] W.B. Bradley, A.S. Kobayashi, An investigation of propagating cracks by dynamic photoelasticity, Exp. Mech. 10 (1970) 106–113.

[137] A. Chudnovsky, M. Kachanov, INTERACTION OF A CRACK WITH A FIELD OF MICROCRACKS, Lett. Appl. Eng. Sci. 21 (1983) 1009–1018.

[138] M.F. Ashby, S.D. Hallam, The Failure of Brittle Solids Containing Small Cracks Under Compressive Stress States, Acta Metall. 34 (1986) 497–510.

[139] B. Aydelotte, B. Schuster, Observation and Modeling of Cone Cracks in Ceramics, in: B. Song, L. Lamberson, D. Casem, J. Kimberley (Eds.), Dyn. Behav. Mater. Vol. 1, Springer International Publishing, Cham, 2016: pp. 19–23. http://link.springer.com/10.1007/978-3-319-22452-7_4 (accessed December 14, 2016).

[140] P.-Q. Ji, X.-P. Zhang, Q. Zhang, A new method to model the non-linear crack closure behavior of rocks under uniaxial compression, Int. J. Rock Mech. Min. Sci. 112 (2018) 171–183. https://doi.org/10.1016/j.ijrmms.2018.10.015.

[141] W. Braue, B. Hildmann, H. Schneider, U. Hornemann, The crystalline-to-amorphous transition in shock-loaded mullite Al2VI(Al2+2xSi2−2x)IVO10−x in the light of shear modulus anisotropy, J. Eur. Ceram. Soc. 29 (2009) 3135–3146. https://doi.org/10.1016/j.jeurceramsoc.2009.05.051.

[142] D. Ghosh, G. Subhash, J.Q. Zheng, V. Halls, Influence of stress state and strain rate on structural amorphization in boron carbide, J. Appl. Phys. 111 (2012) 063523. https://doi.org/10.1063/1.3696971.

[143] A.P. Awasthi, G. Subhash, High-pressure deformation and amorphization in boron carbide, J. Appl. Phys. 125 (2019) 215901. https://doi.org/10.1063/1.5091795.

[144] Q. An, W.A. Goddard, K.Y. Xie, G. Sim, K.J. Hemker, T. Munhollon, M.F. Toksoy, R.A. Haber, Superstrength through Nanotwinning, Nano Lett. 16 (2016) 7573–7579. https://doi.org/10.1021/acs.nanolett.6b03414.

[145] X. Li, S. Yin, S.H. Oh, H. Gao, Hardening and toughening mechanisms in nanotwinned ceramics, Scr. Mater. 133 (2017) 105–112. https://doi.org/10.1016/j.scriptamat.2017.02.003.

[146] D.R. Curran, L. Seaman, T. Cooper, D.A. Shockey, Micromechanical model for comminution and granular flow of brittle material under high strain rate application to penetration of ceramic targets, Int. J. Impact Eng. 13 (1993) 53–83.

[147] M.W. Chen, J.W. McCauley, J.C. LaSalvia, K.J. Hemker, Microstructural Characterization of Commercial Hot-Pressed Boron Carbide Ceramics, J. Am. Ceram. Soc. 88 (2005) 1935–1942. https://doi.org/10.1111/j.1551-2916.2005.00346.x.

[148] Z.P. Bažant, F.C. Caner, Comminution of solids caused by kinetic energy of high shear strain rate, with implications for impact, shock, and shale fracturing, Proc. Natl. Acad. Sci. 110 (2013) 19291–19294.

[149] Z.P. Bažant, F.C. Caner, Impact comminution of solids due to local kinetic energy of high shear strain rate: I. Continuum theory and turbulence analogy, J. Mech. Phys. Solids. 64 (2014) 223–235. https://doi.org/10.1016/j.jmps.2013.11.008.

[150] Z.P. Bažant, Y. Su, Impact Comminution of Solids Due to Progressive Crack Growth Driven by Kinetic Energy of High-Rate Shear, J. Appl. Mech. 82 (2015) 031007. https://doi.org/10.1115/1.4029636.

[151] J.D. Hogan, L. Farbaniec, N. Daphalapurkar, K.T. Ramesh, On Compressive Brittle Fragmentation, J. Am. Ceram. Soc. 99 (2016) 2159–2169. https://doi.org/10.1111/jace.14171.

[152] J.D. Hogan, L. Farbaniec, T. Sano, M. Shaeffer, K.T. Ramesh, The effects of defects on the uniaxial compressive strength and failure of an advanced ceramic, Acta Mater. 102 (2016) 263–272. https://doi.org/10.1016/j.actamat.2015.09.028.

[153] D.M. Collins, M. Mostafavi, R.I. Todd, T. Connolley, A.J. Wilkinson, A synchrotron X-ray diffraction study of in situ biaxial deformation, Acta Mater. 90 (2015) 46–58. https://doi.org/10.1016/j.actamat.2015.02.009.

[154] D.M. Collins, T. Erinosho, F.P.E. Dunne, R.I. Todd, T. Connolley, M. Mostafavi, H. Kupfer, A.J. Wilkinson, A synchrotron X-ray diffraction study of non-proportional strain-path effects, Acta Mater. 124 (2017) 290–304. https://doi.org/10.1016/j.actamat.2016.11.011.

[155] E.N. Landis, D.T. Keane, X-ray microtomography for fracture studies in cement-based materials, in: Dev. X-Ray Tomogr. II, International Society for Optics and Photonics, 1999: pp. 105–114.

[156] E. Maire, C. Le Bourlot, J. Adrien, A. Mortensen, R. Mokso, 20 Hz X-ray tomography during an in situ tensile test, Int. J. Fract. 200 (2016) 3–12. https://doi.org/10.1007/s10704-016-0077-y.

[157] E. Strassburger, Stress wave and damage propagation in transparent laminates at elevated temperatures, DTIC Document, 2010. http://oai.dtic.mil/oai/oai?verb=getRecord&metadataPrefix=html&identifier=ADA519117 (accessed September 26, 2016).

[158] J.Y. Huang, J.C. E, J.W. Huang, T. Sun, K. Fezzaa, S.L. Xu, S.N. Luo, Dynamic deformation and fracture of single crystal silicon: Fracture modes, damage laws, and anisotropy, Acta Mater. 114 (2016) 136–145. https://doi.org/10.1016/j.actamat.2016.05.022.

[159] Y. Hao, H. Hao, G.P. Jiang, Y. Zhou, Experimental confirmation of some factors influencing dynamic concrete compressive strengths in high-speed impact tests, Cem. Concr. Res. 52 (2013) 63–70. https://doi.org/10.1016/j.cemconres.2013.05.008.

[160] M. Salviato, K. Kirane, Z.P. Bazˇant, Statistical distribution and size effect of residual strength of quasibrittle materials after a period of constant load, J. Mech. Phys. Solids. 64 (2014) 440–454. https://doi.org/10.1016/j.jmps.2013.12.005.

[161] B.J. Dalgleish, A. Fakhr, P.L. Pratt, R.D. Rawlings, The Fracture Toughness-Microstructure Relationship of Alumina-Based Ceramics, (n.d.) 2031–2038.

[162] M. Guazzato, M. Albakry, S.P. Ringer, M.V. Swain, Strength, fracture toughness and microstructure of a selection of all-ceramic materials. Part I. Pressable and alumina glass-infiltrated ceramics, Dent. Mater. 20 (2004) 441–448. https://doi.org/10.1016/j.dental.2003.05.003.

[163] A.D. Norton, S. Falco, N. Young, J. Severs, R.I. Todd, Microcantilever investigation of fracture toughness and subcritical crack growth on the scale of the microstructure in Al 2 O 3, J. Eur. Ceram. Soc. 35 (2015) 4521–4533. https://doi.org/10.1016/j.jeurceramsoc.2015.08.023.

[164] N.P. Padture, B.R. Lawn, Toughness Properties of a Silicon Carbide with an in Situ Induced Heterogeneous Grain Structure, J. Am. Ceram. Soc. 77 (1994) 2518–2522. https://doi.org/10.1111/j.1151-2916.1994.tb04637.x.

[165] L.-S. Chang, T.-H. Chuang, W.J. Wei, Characterization of alumina ceramics by ultrasonic testing, Mater. Charact. 45 (2000) 221–226. https://doi.org/10.1016/S1044-5803(00)00081-4.

[166] R.S. Lima, S.E. Kruger, G. Lamouche, B.R. Marple, Elastic Modulus Measurements via Laser-Ultrasonic and Knoop Indentation Techniques in Thermally Sprayed Coatings, J. Therm. Spray Technol. 14 (2005) 52–60. https://doi.org/10.1361/10599630522701.

[167] B.R. Goodlet, C.J. Torbet, E.J. Biedermann, L.M. Jauriqui, J.C. Aldrin, T.M. Pollock, Forward models for extending the mechanical damage evaluation capability of resonant ultrasound spectroscopy, Ultrasonics. 77 (2017) 183–196. https://doi.org/10.1016/j.ultras.2017.02.002.

[168] K.K. Phani, Correlation between ultrasonic shear wave velocity and Poisson's ratio for isotropic porous materials, J. Mater. Sci. 43 (2008) 316–323. https://doi.org/10.1007/s10853-007-2055-2.

[169] A. Migliori, J.L. Sarrao, W.M. Visscher, T.M. Bell, M. Lei, Z. Fisk, R.G. Leisure, Resonant ultrasound spectroscopic techniques for measurement of the elastic moduli of solids, Phys. B Condens. Matter. 183 (1993) 1–24.

[170] S. Nemat-Nasser, H. Horii, ROCK FAILURE IN COMPRESSION, Int. J. Eng. Sci. 22 (1984) 999–1011.

[171] Z. Hui, L. Hongyan, A Damage Constitutive Model for a Rock Considering the Microcrack Deformation and Propagation, Electron. J. Geotech. Eng. 21 (2016) 4507–4518.

[172] C. Landron, E. Maire, O. Bouaziz, J. Adrien, L. Lecarme, A. Bareggi, Validation of void growth models using X-ray microtomography characterization of damage in dual phase steels, Acta Mater. 59 (2011) 7564–7573. https://doi.org/10.1016/j.actamat.2011.08.046.

[173] F.M. Aben, M.-L. Doan, J.-P. Gratier, F. Renard, Coseismic damage generation and pulverization in fault zones: insights from dynamic Split-Hopkinson Pressure Bar experiments, in: Evol. Fault Zone Prop. Dyn. Process. Seism. Rupture, 2017. https://www.researchgate.net/profile/Francois_Renard/publication/318172696_Coseismic_Damage_Generation_and_Pulverization_in_Fault_Zones_Evolution_of_Fault_Properties_During_Seismic_Rupture/links/59637e7da6fdccc9b15a3a84/Coseismic-Damage-Generation-and-Pulverization-in-Fault-Zones-Evolution-of-Fault-Properties-During-Seismic-Rupture.pdf (accessed August 8, 2017).

[174] V.L. Shkuratnik, P.V. Nikolenko, A.E. Koshelev, Stress dependence of elastic P-wave velocity and amplitude in coal specimens under varied loading conditions, J. Min. Sci. 52 (2016) 873–877. https://doi.org/10.1134/S1062739116041322.

[175] B.M.L. Koch, C. Lo, H. Li, T. Sano, Jonathan Ligda, Hogan, James D., Two-Dimensional Dynamic Damage Accumulation in Engineered Brittle Materials, Eng. Fract. Mech. 244 (2021).

[176] L. Farbaniec, J.D. Hogan, K.Y. Xie, M. Shaeffer, K.J. Hemker, K.T. Ramesh, Damage evolution of hot-pressed boron carbide under confined dynamic compression, Int. J. Impact Eng. 99 (2017) 75–84. https://doi.org/10.1016/j.ijimpeng.2016.09.008.

[177] C. Lo, T. Sano, J.D. Hogan, Deformation mechanisms and evolution of mechanical properties in damaged advanced ceramics, J. Eur. Ceram. Soc. 40 (2020) 3129–3139. https://doi.org/10.1016/j.jeurceramsoc.2020.02.058.

[178] L.F. Pereira, J. Weerheijm, L.J. Sluys, A new rate-dependent stress-based nonlocal damage model to simulate dynamic tensile failure of quasi-brittle materials, Int. J. Impact Eng. 94 (2016) 83–95. https://doi.org/10.1016/j.ijimpeng.2016.04.002.

[179] D.E. Grady, Adiabatic shear failure in brittle solids, Int. J. Impact Eng. 38 (2011) 661–667. https://doi.org/10.1016/j.ijimpeng.2011.01.001.

[180] K. Hajlaoui, A.R. Yavari, B. Doisneau, A. LeMoulec, W.J. Botta F., G. Vaughan, A.L. Greer, A. Inoue, W. Zhang, å. Kvick, Shear delocalization and crack blunting of a metallic glass containing nanoparticles: In situ deformation in TEM analysis, Scr. Mater. 54 (2006) 1829–1834. https://doi.org/10.1016/j.scriptamat.2006.02.030.

[181] Z. Rosenberg, D. Yaziv, Y. Yeshurun, S.J. Bless, Shear strength of shock?loaded alumina as determined with longitudinal and transverse manganin gauges, J. Appl. Phys. 62 (1987) 1120–1122. https://doi.org/10.1063/1.339721.

[182] H. Abe, M. Naito, T. Hotta, N. Shinohara, K. Uematsu, Flaw Size Distribution in High-Quality Alumina, J. Am. Ceram. Soc. 86 (2003) 1019–1021.

[183] J. Kim, Y. Kwon, N. Shin, K. Sohn, Visualization of fractures in alumina ceramics by mechanoluminescence, Acta Mater. 53 (2005) 4337–4343. https://doi.org/10.1016/j.actamat.2005.05.032.

[184] L.A. Xue, I.-W. Chen, Deformation and Grain Growth of Low-Temperature-Sintered High-Purity Alumina, J. Am. Ceram. Soc. 73 (1990) 3518–3521. https://doi.org/10.1111/j.1151-2916.1990.tb06489.x.

[185] Y. Zhou, K. Hirao, M. Toriyama, Y. Yamauchi, S. Kanzaki, Effects of intergranular phase chemistry on the microstructure and mechanical properties of silicon carbide ceramics densified with rare-earth oxide and alumina additions, J. Am. Ceram. Soc. 84 (2001) 1642–1644.

[186] D. SCITI, A. BELLOSI, Effects of additives on densification, microstructure and properties of liquid-phase sintered silicon carbide, (n.d.) 7.

[187] E.H. Lutz, M.V. Swain, N. Claussen, Thermal Shock Behavior of Duplex Ceramics, J. Am. Ceram. Soc. 74 (1991) 19–24. https://doi.org/10.1111/j.1151-2916.1991.tb07290.x.

[188] H. Luo, W.W. Chen, A.M. Rajendran, Dynamic Compressive Response of Damaged and Interlocked SiC-N Ceramics, J. Am. Ceram. Soc. 89 (2006) 266–273. https://doi.org/10.1111/j.1551-2916.2005.00688.x.

[189] P. Nicewicz, P. Peciar, O. Macho, T. Sano, J.D. Hogan, Quasi-static confined uniaxial compaction of granular alumina and boron carbide observing the particle size effects, J. Am. Ceram. Soc. 103 (2020) 2193–2209. https://doi.org/10.1111/jace.16871.

[190] E. Krimsky, K.T. Ramesh, M. Bratcher, M. Foster, J.D. Hogan, Quantification of damage and its effects on the compressive strength of an advanced ceramic, Eng. Fract. Mech. 208 (2019) 107–118. https://doi.org/10.1016/j.engfracmech.2019.01.007.

[191] B.M.L. Koch, P. Jannotti, D. Mallick, B. Schuster, T. Sano, J.D. Hogan, Influence of microstructure on the impact failure of alumina, Mater. Sci. Eng. A. 770 (2020) 138549. https://doi.org/10.1016/j.msea.2019.138549.

[192] C. Lo, T. Sano, J.D. Hogan, Micostructural and Mechanical Characterization of Variability in Porour Advanced Ceramics Using X-Ray Computed Tomography and Digital Image Correlation, Acta Mater. (2019).

[193] J. Kimberley, J. Paul, A Miniature Tensile Kolsky Bar for Thin Film Testing, in: B. Song, D. Casem, J. Kimberley (Eds.), Dyn. Behav. Mater. Vol. 1, Springer International Publishing, Cham, 2015: pp. 221–226. http://link.springer.com/10.1007/978-3-319-06995-1_33 (accessed October 3, 2016).

[194] M.H. Ahmadi, H. Molladavoodi, A micromechanical Sliding-Damage Model Under Dynamic Compressive Loading, Period. Polytech. Civ. Eng. (2019). https://doi.org/10.3311/PPci.13249.

[195] M. Basista, D. Gross, The sliding crack model of brittle deformation: an internal variable approach, Int. J. Solids Struct. 35 (1998) 487–509.

[196] A. Arab, R. Ahmad, Z.A. Ahmad, Effect of SrCO3 addition on the dynamic compressive strength of ZTA, Int. J. Miner. Metall. Mater. 23 (2016) 481–489. https://doi.org/10.1007/s12613-016-1259-3.

[197] K.T. Ramesh, J.D. Hogan, J. Kimberley, A. Stickle, A review of mechanisms and models for dynamic failure, strength, and fragmentation, Planet. Space Sci. 107 (2015) 10–23. https://doi.org/10.1016/j.pss.2014.11.010.

[198] Z.P. Bažant, F.C. Caner, Impact comminution of solids due to local kinetic energy of high shear strain rate: I. Continuum theory and turbulence analogy, J. Mech. Phys. Solids. 64 (2014) 223–235. https://doi.org/10.1016/j.jmps.2013.11.008.

[199] H. Deng, S. Nemat-Nasser, Microcrack Interaction and Shear Fault Failure, Int. J. Damage Mech. 3 (1994) 3–37. https://doi.org/10.1177/105678959400300101.

[200] J.D. Clayton, Penetration resistance of armor ceramics: Dimensional analysis and property correlations, Int. J. Impact Eng. 85 (2015) 124–131. https://doi.org/10.1016/j.ijimpeng.2015.06.025.

[201] W. Liu, Z. Chen, X. Cheng, Y. Wang, A.R. Amankwa, J. Xu, Design and ballistic penetration of the ceramic composite armor, Compos. Part B Eng. 84 (2016) 33–40. https://doi.org/10.1016/j.compositesb.2015.08.071.

[202] C.D. Hilton, J.W. McCauley, J.J. Swab, E.R. Shanholtz, M.W. Chen, Using Hardness Tests to Quantify Bulk Plasticity and Predict Transition Velocities in SiC Materials, Int. J. Appl. Ceram. Technol. 10 (2013) 114–122. https://doi.org/10.1111/j.1744-7402.2012.02817.x.

[203] H. Deng, S. Nemat-Nasser, Dynamic damage evolution in brittle solids, Mech. Mater. 14 (1992) 83–103.

[204] C.E. Anderson, J.D. Walker, An analytical model for dwell and interface defeat, Int. J. Impact Eng. 31 (2005) 1119–1132. https://doi.org/10.1016/j.ijimpeng.2004.07.013.

[205] E. Strassburger, S. Bauer, S. Weber, H. Gedon, Flash X-ray cinematography analysis of dwell and penetration of small caliber projectiles with three types of SiC ceramics, Def. Technol. 12 (2016) 277–283. https://doi.org/10.1016/j.dt.2016.01.011.

[206] D.A. Shockey, A.H. Marchand, S.R. Skaggs, G.E. Cort, M.W. Burkett, R. Parker, Failure Phenomenology of Confined Ceramic Targets and Impacting Rods, Int. J. Impact Eng. 9 (1990) 263–275.

[207] Z.P. Bažant, F.C. Caner, Comminution of solids caused by kinetic energy of high shear strain rate, with implications for impact, shock, and shale fracturing, Proc. Natl. Acad. Sci. 110 (2013) 19291–19294.

[208] Z.P. Bažant, Y. Su, Impact Comminution of Solids Due to Progressive Crack Growth Driven by Kinetic Energy of High-Rate Shear, J. Appl. Mech. 82 (2015) 031007. https://doi.org/10.1115/1.4029636.

[209] R.L. Landingham, A.W. Casey, Final Report of the Light Armor Materials Program, Lawrence Livermore Natl. Lab. UCRL-51269. (1972). http://www.iaea.org/inis/collection/NCLCollectionStore/_Public/04/068/4068133.pdf (accessed June 23, 2017).

[210] A.G. Evans, M.E. Gulden, M. Rosenblatt, Impact damage in brittle materials in the elastic-plastic response regime, Proc. R. Soc. Lond. A. 361 (1978) 343–365.

[211] S.J. Bless, Z. Rosenberg, B. Yoon, Hypervelocity Penetration of Ceramics, Int. J. Impact Eng. 5 (1987) 165–171.

[212] T.J. Holmquist, G.R. Johnson, Characterization and evaluation of boron carbide for plate-impact conditions, J. Appl. Phys. 100 (2006) 093525. https://doi.org/10.1063/1.2362979.

[213] G.R. Johnson, T.J. Holmquist, Response of boron carbide subjected to large strains, high strain rates, and high pressures, J. Appl. Phys. 85 (1999) 8060. https://doi.org/10.1063/1.370643.

[214] T.J. Holmquist, G.R. Johnson, Response of boron carbide subjected to high-velocity impact, Int. J. Impact Eng. 35 (2008) 742–752. https://doi.org/10.1016/j.ijimpeng.2007.08.003.

[215] M. Bakas, J.W. McCauley, V. Greenhut, D. Niesz, R. Haber, B. West, Quantitative analysis of inclusion distributions in hot pressed silicon carbide, Int. J. Impact Eng. 50 (2012) 40–48. https://doi.org/10.1016/j.ijimpeng.2012.06.010.

[216] C. Denoual, C.E. Cottenot, others, Visualization of the damage evolution in impacted silicon carbide ceramics, Int. J. Impact Eng. 21 (1998) 225–235.

[217] H. Abe, M. Naito, T. Hotta, N. Shinohara, K. Uematsu, Flaw Size Distribution in High-Quality Alumina, J. Am. Ceram. Soc. 86 (2003) 1019–1021.

[218] M. Bai, W. Li, Y. Li, W. Zhao, jianqing Wu, P. Rao, Low-velocity impact property of alumina/epoxy/metal laminated composites, J. Wuhan Univ. Technol.-Mater Sci Ed. 31 (2016) 779–785. https://doi.org/10.1007/s11595-016-1445-1.

[219] B.J. Dalgleish, A. Fakhr, P.L. Pratt, R.D. Rawlings, The Fracture Toughness-Microstructure Relationship of Alumina-Based Ceramics, (n.d.) 2031–2038.

[220] W.P. Huhn, M. Widom, A free energy model of boron carbide, J. Stat. Phys. 150 (2013) 432–441.

[221] V. Domnich, S. Reynaud, R.A. Haber, M. Chhowalla, Boron Carbide: Structure, Properties, and Stability under Stress, J. Am. Ceram. Soc. 94 (2011) 3605–3628. https://doi.org/10.1111/j.1551-2916.2011.04865.x.

[222] M.W. Chen, J.W. McCauley, J.C. LaSalvia, K.J. Hemker, Microstructural Characterization of Commercial Hot-Pressed Boron Carbide Ceramics, J. Am. Ceram. Soc. 88 (2005) 1935–1942. https://doi.org/10.1111/j.1551-2916.2005.00346.x.

[223] L. Farbaniec, J.D. Hogan, K.T. Ramesh, Micromechanisms associated with the dynamic compressive failure of hot-pressed boron carbide, Scr. Mater. 106 (2015) 52–56. https://doi.org/10.1016/j.scriptamat.2015.05.004.

[224] W. Braue, B. Hildmann, H. Schneider, U. Hornemann, The crystalline-to-amorphous transition in shock-loaded mullite Al2VI(Al2+2xSi2−2x)IVO10−x in the light of shear modulus anisotropy, J. Eur. Ceram. Soc. 29 (2009) 3135–3146. https://doi.org/10.1016/j.jeurceramsoc.2009.05.051.

[225] M. Chen, Shock-Induced Localized Amorphization in Boron Carbide, Science. 299 (2003) 1563–1566. https://doi.org/10.1126/science.1080819.

[226] D. Ghosh, G. Subhash, J.Q. Zheng, V. Halls, Influence of stress state and strain rate on structural amorphization in boron carbide, J. Appl. Phys. 111 (2012) 063523. https://doi.org/10.1063/1.3696971.

[227] G. Subhash, D. Ghosh, J. Blaber, J.Q. Zheng, V. Halls, K. Masters, Characterization of the 3-D amorphized zone beneath a Vickers indentation in boron carbide using Raman spectroscopy, Acta Mater. 61 (2013) 3888–3896. https://doi.org/10.1016/j.actamat.2013.03.028.

[228] G. Subhash, A.P. Awasthi, C. Kunka, P. Jannotti, M. DeVries, In search of amorphization-resistant boron carbide, Scr. Mater. 123 (2016) 158–162. https://doi.org/10.1016/j.scriptamat.2016.06.012.

[229] T.J. Moynihan, J.C. LaSalvia, M.S. Burkins, Analysis of Shatter Gap Phenomenon in a Boron Carbide-Composite Laminate Armor System, in: Orlando, FL, 2002.

[230] D.P. Dandekar, Shock response of boron carbide, ARMY RESEARCH LAB ABERDEEN PROVING GROUND MD, 2001. http://www.dtic.mil/docs/citations/ADA389400 (accessed July 14, 2017).

[231] D.D. Mallick, K.T. Ramesh, Dynamic fragmentation of boron carbide using laser-driven flyers, Int. J. Impact Eng. 136 (2020) 103416. https://doi.org/10.1016/j.ijimpeng.2019.103416.

[232] B.M.L. Koch, C. Lo, H. Li, T. Sano, J. Ligda, J.D. Hogan, Dynamic mechanical response of damaged alumina AD995, J. Eur. Ceram. Soc. 41 (2021) 2034–2048. https://doi.org/10.1016/j.jeurceramsoc.2020.10.020.

[233] C. Lo, H. Li, J. Ligda, G. Toussaint, J.D. Hogan, On the Evaluation of Mechanical Properties and Ballistic Performance of Two Variants of Boron Carbide, Int. J. Impact Eng. 152 (2021) 44.

[234] C. Anderson, S. Chocron, K.A. Dannemann, A.E. Nicholls, Testing boron carbide under triaxial compression, in: 2012: pp. 88–91. https://doi.org/10.1063/1.3686228.

[235] K. Kuwelkar, V. Domnich, W. Rafaniello, R. Haber, J.D. Hogan, Characterization of Boron Carbide Powders and Boron Carbide Ceramics, (2015).

[236] W. Ji, S.S. Rehman, W. Wang, H. Wang, Y. Wang, J. Zhang, F. Zhang, Z. Fu, Sintering boron carbide ceramics without grain growth by plastic deformation as the dominant densification mechanism, Sci. Rep. 5 (2015) 15827. https://doi.org/10.1038/srep15827.

[237] B. Amirian, H. Li, J.D. Hogan, The Mechanical Response of a α2(Ti3Al)+γ(TiAl)-Nanograined Al2O3 Cermet Under Dynamic Compression: Modeling and Experiment, Acta Mater. (2019).

[238] S. Nemat-Nasser, M. Obata, A microcrack model of dilatancy in brittle materials, J Appl Mech. 55 (1988) 24–35.

[239] W.F. Brace, E.G. Bombolakis, A note on brittle crack growth in compression, J. Geophys. Res. 68 (1963) 3709–3713.
[240] E.G. Bombolakis, Study of the brittle fracture process under uniaxial compression, Tectonophysics. 18 (1973) 231–248.
[241] J. Kimberley, K.T. Ramesh, N.P. Daphalapurkar, A scaling law for the dynamic strength of brittle solids, Acta Mater. 61 (2013) 3509–3521. https://doi.org/10.1016/j.actamat.2013.02.045.
[242] C.C. Holland, R.M. McMeeking, The influence of mechanical and microstructural properties on the rate-dependent fracture strength of ceramics in uniaxial compression, Int. J. Impact Eng. 81 (2015) 34–49. https://doi.org/10.1016/j.ijimpeng.2015.02.007.
[243] Z.P. Bažant, S.-D. Pang, Activation energy based extreme value statistics and size effect in brittle and quasibrittle fracture, J. Mech. Phys. Solids. 55 (2007) 91–131. https://doi.org/10.1016/j.jmps.2006.05.007.
[244] K. Bhattacharya, G. Ravichandran, Energy-Based Model of Compressive Splitting in Heterogenous Brittle Solids, J. Mech. Phys. Solids. 46 (1998) 2171–2181.
[245] F.C. Caner, Z.P. Bažant, Impact comminution of solids due to local kinetic energy of high shear strain rate: II–Microplane model and verification, J. Mech. Phys. Solids. 64 (2014) 236–248. https://doi.org/10.1016/j.jmps.2013.11.009.
[246] A.L. Tonge, K.T. Ramesh, Application of the Tonge-Ramesh micromechanics based damage model to boron carbide under uniaxial compression and simplied ballistic loading, (2014).
[247] J. Huang, S. Xu, S. Hu, Influence of particle breakage on the dynamic compression responses of brittle granular materials, Mech. Mater. 68 (2014) 15–28. https://doi.org/10.1016/j.mechmat.2013.08.002.
[248] M.F. Ashby, C.G. Sammis, The Damage Mechanics of Brittle Solids in Compression, Pure Appl. Geophys. 133 (1990) 489–520.
[249] K. Gbetchi, C. Dascalu, Two-scale thermomechanical damage model for dynamic shear failure in brittle solids, Contin. Mech. Thermodyn. (2020). https://doi.org/10.1007/s00161-020-00916-x.
[250] A. Chudnovsky, M. Kachanov, INTERACTION OF A CRACK WITH A FIELD OF MICROCRACKS, Lett. Appl. Eng. Sci. 21 (1983) 1009–1018.
[251] B. Schuster, Radiography and Phase Contrast Imaging of Ballistic Impact in Boron Carbide, (2016).
[252] D.H. Dolan, Accuracy and precision in photonic Doppler velocimetry, Rev. Sci. Instrum. 81 (2010) 053905. https://doi.org/10.1063/1.3429257.
[253] V.R. Shea, D.R. Hanson, Elastic Wave Velocity and Attenuation as Used to Define Phases of Loading and Failure in Coal, Int. J. Rock Mech. Min. Sci. 25 (1988) 431–437.